


PHYSICS RESEARCH AND TECHNOLOGY

SOLAR FLARES



Investigations and
Selected Research

Sarah L. Jones
Editor

Novinka

Complimentary Contributor Copy

PHYSICS RESEARCH AND TECHNOLOGY

SOLAR FLARES

INVESTIGATIONS AND SELECTED RESEARCH

No part of this digital document may be reproduced, stored in a retrieval system or transmitted in any form or by any means. The publisher has taken reasonable care in the preparation of this digital document, but makes no expressed or implied warranty of any kind and assumes no responsibility for any errors or omissions. No liability is assumed for incidental or consequential damages in connection with or arising out of information contained herein. This digital document is sold with the clear understanding that the publisher is not engaged in rendering legal, medical or other professional services.

Complimentary Contributor Copy

PHYSICS RESEARCH AND TECHNOLOGY

Additional books in this series can be found on Nova's website under the Series tab.

Additional e-books in this series can be found on Nova's website under the eBooks tab.

PHYSICS RESEARCH AND TECHNOLOGY

SOLAR FLARES
INVESTIGATIONS AND
SELECTED RESEARCH

SARAH L. JONES
EDITOR



New York

Complimentary Contributor Copy

Copyright © 2016 by Nova Science Publishers, Inc.

All rights reserved. No part of this book may be reproduced, stored in a retrieval system or transmitted in any form or by any means: electronic, electrostatic, magnetic, tape, mechanical photocopying, recording or otherwise without the written permission of the Publisher.

We have partnered with Copyright Clearance Center to make it easy for you to obtain permissions to reuse content from this publication. Simply navigate to this publication's page on Nova's website and locate the "Get Permission" button below the title description. This button is linked directly to the title's permission page on copyright.com. Alternatively, you can visit copyright.com and search by title, ISBN, or ISSN.

For further questions about using the service on copyright.com, please contact:

Copyright Clearance Center

Phone: +1-(978) 750-8400

Fax: +1-(978) 750-4470

E-mail: info@copyright.com.

NOTICE TO THE READER

The Publisher has taken reasonable care in the preparation of this book, but makes no expressed or implied warranty of any kind and assumes no responsibility for any errors or omissions. No liability is assumed for incidental or consequential damages in connection with or arising out of information contained in this book. The Publisher shall not be liable for any special, consequential, or exemplary damages resulting, in whole or in part, from the readers' use of, or reliance upon, this material. Any parts of this book based on government reports are so indicated and copyright is claimed for those parts to the extent applicable to compilations of such works.

Independent verification should be sought for any data, advice or recommendations contained in this book. In addition, no responsibility is assumed by the publisher for any injury and/or damage to persons or property arising from any methods, products, instructions, ideas or otherwise contained in this publication.

This publication is designed to provide accurate and authoritative information with regard to the subject matter covered herein. It is sold with the clear understanding that the Publisher is not engaged in rendering legal or any other professional services. If legal or any other expert assistance is required, the services of a competent person should be sought. FROM A DECLARATION OF PARTICIPANTS JOINTLY ADOPTED BY A COMMITTEE OF THE AMERICAN BAR ASSOCIATION AND A COMMITTEE OF PUBLISHERS.

Additional color graphics may be available in the e-book version of this book.

Library of Congress Cataloging-in-Publication Data

Names: Jones, Sarah L. (Editor), editor.

Title: Solar flares : investigations and selected research / Sarah L. Jones, editor.

Other titles: Physics research and technology.

Description: Hauppauge, New York : Nova Science Publishers, Inc., [2016] |

Series: Physics research and technology | Includes bibliographical references and index.

Identifiers: LCCN 2016041838 (print) | LCCN 2016044862 (ebook) | ISBN

9781536102048 (softcover) | ISBN 1536102040 (softcover) | ISBN

9781536102215 (ebook) | ISBN 1536102210 (ebook) | ISBN 9781536102215

Subjects: LCSH: Solar flares. | Ionospheric electron density. | D region.

Classification: LCC QB526.F6 S592 2016 (print) | LCC QB526.F6 (ebook) | DDC

523.7/5--dc23

LC record available at <https://lcn.loc.gov/2016041838>

Published by Nova Science Publishers, Inc. † New York

Complimentary Contributor Copy

CONTENTS

Preface		vii
Chapter 1	Solar Flares: Origin and Threat to Our Civilization <i>Nils-Axel Mörner</i>	1
Chapter 2	Electron Density Characteristics in Ionospheric D-Region during Solar X-Ray Flare <i>Aleksandra Nina</i>	13
Chapter 3	Analysis of the Ionospheric D-Region Disturbances in Response to the Effects of Solar X-Ray Flares <i>Desanka M. Šulić, Vladimir A. Srećković and Anatolij A. Mihajlov</i>	45
Chapter 4	Solar Flares on Transition from the Grand Maximum to the Minimum? <i>V. G. Kossobokov, J. L. Le Mouél and V. Courtillot</i>	81
Chapter 5	Latest News on Zebra Patterns in the Solar Radio Emission <i>G. P. Chernov</i>	101
Index		151

PREFACE

Solar Flares refer to solar coronal mass ejections (CME), also known as geomagnetic storms. Solar flares are an important part of solar activity, associated with rapid and intense energy release in active regions of the solar atmosphere. In this book, Chapter One discusses the origin of solar flares and their threat to our civilization. Chapter Two presents a study of time and space variations of electron density characteristics during a solar X-ray flare influence. Chapter Three provides an analysis of the ionospheric D-region disturbances in response to the effects of solar X-ray flares. Chapter Four updates an analysis from January 2011 through July 2016 and discusses whether new research sheds any light on the ongoing Cycle 24 unusual structure and on its future. Chapter Five explores the latest news on zebra patterns in solar radio emissions.

Chapter 1 – Solar flares constantly evolve on the surface of the Sun. Occasionally they are of gigantic magnitude. When the mass ejection of such events hit the Earth they affect the magnetosphere generating intense aurora borealis events and the shielding capacity against cosmic rays. The largest solar flare event recorded was the Carrington event in 1859. The telegraph systems broke down. It occurred in pre-electric and pre-electronic times, however. Had it occurred today, the effects would have been disastrous. This calls for a deeper analysis of the situation. Considering new records of superflares of Sun-like stars and terrestrial records of possible “paleo-solar-flares,” we must conclude that our Sun seems capable of producing giant solar flares 10 to 100 times as strong as the Carrington event. In view of this solar flares emerge as the possibly greatest threat to modern life on planet Earth.

Chapter 2 – Solar X-ray flares play a very important role in the lower ionosphere dynamics. Previous researches have shown that the electron

density, as one of the most important plasma parameters in ionospheric investigations, can change by one or two orders of magnitude under the influence of the considered X-radiation in the lowest part of the ionosphere called the D-region. These changes are correlated with other parameters and must be known in various calculations needed in analyses of the ionospheric plasma properties. Among others, they represent changes in characteristics of the medium which are relevant to propagation of electromagnetic waves including telecommunication signals whose use is unavoidable in numerous aspects of the contemporary way of living. For these reasons the analyses of electron density variations are very important in both the pure scientific studies and practical applications in technology, and they represent the connection between the space weather and its influence on the Earth, and our daily life. In this research we present a study of time and space variations of electron density characteristics during a solar X-ray flare influence. The attention is focused on the electron density and its time and altitude derivatives which are the most relevant parameters for various further analyses and various practical applications. To show the main characteristics of the D-region response to the incoming X-radiation increase we compare time evolutions of the X-ray intensity detected by the GOES satellite with electron density properties, and point out differences during their specific phases. The calculations of the electron density are based on the low ionosphere monitoring by very low frequency (VLF) radio waves and, in the presented research, we process data related to the amplitude and phase of a signal emitted by the DHO transmitter in Germany and received in Serbia.

Chapter 3 – The sensitivity of Very Low Frequency (VLF, 3-30 kHz) and Low Frequency (LF, 30-300 kHz) propagation in the lower ionosphere makes it an ideal probe for remotely sensing the ambient state and localized perturbations of the lower ionosphere. During occurrence of solar X-ray flare the altitude distribution of the ionospheric electron density is a noticeable and interesting issue and known as Sudden Ionospheric Disturbance (SID). This is an important classical topic event for solar-terrestrial relations. The induced SID in the D-region causes perturbations in the received amplitude and phase on VLF/LF radio signals. The basis of this work is amplitude and phase data acquired by monitoring NAA/24.00 kHz, GQD/22.10 kHz, DHO/23.40 kHz, ICV/20.27 kHz and NSC/45.90 kHz, radio signals at Belgrade site (44.85° N, 20.38° E) Serbia by AbsPAL and AWESOME receivers since 2003 and 2008 up to 2015, respectively. We expected and estimated differences in amplitude and phase perturbations on VLF/LF radio signals induced by solar X-ray flares which occurrences are under different solar zenith angles over illuminated

propagation paths. Observed VLF perturbations at Belgrade site have sensitive dependence on: *X-ray flare intensity, solar zenith angle, solar flare duration and geophysical characteristics of VLF/LF path*. The model computations applied to the multiple path observations at Belgrade site are able to reproduce a number of the general features of the electron density enhancement induced by occurrence of solar X-ray flares during the period of the ascending phase and the maximum of the Solar Cycle 24.

Chapter 4 – The anomalous character of Solar Cycle 23, which ended in the summer of 2009, has been pointed out. It is even proposed that the solar dynamo is undergoing a transition from a state of “grand maximum” to one of “low activity cycles.” We analyze the time distribution of the number and energy of solar flares, and the duration of intervals between them, from Cycles 21 to the declining Cycle 24. The long duration of Cycle 23 (12.8 years based on sunspots, 13.2 years based on flares), the long interval with no C2+ flare between the end of Cycle 23 and the start of Cycle 24 (466 days) are remarkable compared to the two earlier cycles. The singular shape of Cycle 23 is increasingly striking: the first $\approx 70\%$ of the cycle display (on a logarithmic scale) linearly rising maxima, whereas minima are aligned along a descending slope for the latter part of the cycle. The energy flux oscillates between these and takes the shape of a bifurcation, starting near 2002. Inter-event intervals between successive C2+ flares undergo quasi-periodic (≈ 11 yr) oscillations between two distinct states, which we call “active” and “quiet,” with extremely sharp onset and termination. It has been proposed that anomalous Cycle 23 resembles Cycle 4, which was followed by reduced Cycles 5 and 6 at the time of the Dalton minimum in solar activity. The present, updated analysis of the evolution of solar flares and sunspots in Cycle 24 is in agreement with the hypothesis of a multi-decadal decline in solar activity, following the Grand Maximum that spanned Cycles 18 to 23. Specifically, the dynamics of the solar flare series along with the number of sunspots reveal a pattern of bimodal activity and the ongoing Cycle 24 fits remarkably well the behaviour observed in Cycles 5, 6, and 12, each of which has the total sunspot number in the lowest quartile of this value since 1700. Cycle 24 seems to be a member of this group of lowest solar activity cycles. It should fade away to the solar minimum in about 1 to 3 years.

Chapter 5 – The publications of the last three years concerning the study of the most intriguing fine structure in type IV solar radio bursts – zebra pattern (ZPs), are reviewed. The main attention is paid to new observations, irrespective of whether a paper includes detailed interpretation of an event or simply reports the beginning of operation of a new tool. The radiation

mechanism of a ZP based on a double plasma resonance (DPR) remains the most widespread and standard, though ten alternative mechanisms have been offered. However, in a number of works difficulties with the explanation of a complex zebra are noted, especially in combination with fiber bursts and spikes. Therefore, several papers in which description of the radiation mechanism of a ZP on the DPR is improved are considered in more detail. In spite of lack of spatial information in the radio data we can still follow the flare dynamics using SDO/AIA images in several EUV lines. In the discussion, the debatable questions regarding the comparison of mechanisms associated with DPR in terms of the model of interaction of plasma waves with whistlers are illuminated.

Chapter 1

SOLAR FLARES: ORIGIN AND THREAT TO OUR CIVILIZATION

*Nils-Axel Mörner**

Paleogeophysics and Geodynamics,
Stockholm, Sweden

ABSTRACT

Solar flares constantly evolve on the surface of the Sun. Occasionally they are of gigantic magnitude. When the mass ejection of such events hit the Earth they affect the magnetosphere generating intense aurora borealis events and the shielding capacity against cosmic rays. The largest solar flare event recorded was the Carrington event in 1859. The telegraph systems broke down. It occurred in pre-electric and pre-electronic times, however. Had it occurred today, the effects would have been disastrous.

This calls for a deeper analysis of the situation. Considering new records of superflares of Sun-like stars and terrestrial records of possible “paleo-solar-flares,” we must conclude that our Sun seems capable of producing giant solar flares 10 to 100 times as strong as the Carrington event.

In view of this solar flares emerge as the possibly greatest threat to modern life on planet Earth.

* E-mail: morner@pog.nu.

INTRODUCTION

Solar Flares refer to solar coronal mass ejections (CME), also known as geomagnetic storms. The strongest solar flare observed on the Sun up to today is the Carrington Event in 1859, lasting from August 28 to September 2. With an exceptionally high speed the solar wind plasma generated a large aurora event already on August 29 (Carrington 1860). Ground-based magnetometers recorded exceptionally large geomagnetic storms on September 1 and 2, with powerful aurora events observed as far south as in the Caribbean. The global telegraph systems broke down. Electric power network did not yet exist at the time of the Carrington event, however.

In 2013, Lloyd's of London estimated the cost of damage at 0.6 to 2.6 trillion USD, had a similar magnetic storm occurred in year 1913.

Would such an event occur today, a total disaster is likely to hit the developed world, because almost everything is built up around electricity and electronics. Only native people would pass the event without serious damage.

What makes the situation even worse is that we now have new observational reasons to fear future events even up to 10 to 100 times as strong as the 1859 Carrington event.

GIANT FLARES AND SUPERFLARES

Cliver and Svalgaard (2004) made a penetrating analysis of solar flare events in the last 150 years. As to different space weather effects, peak values were noted as follows:

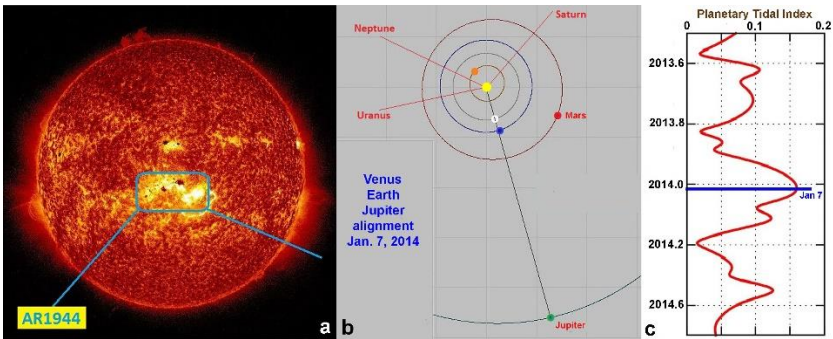
- Geomagnetic storm: max values at 14 March 1989 and 18 September 1941
- Solar wind: max value at 4 August 1972
- Solar energetic particles: max value at August-September 1859 (cf. Figure 3)
- Aurora: max value at 4 February 1872
- Sudden ionospheric disturbance: max value at 4 November 2003

They summarized their analysis in stating “after ~150 years, the first identified space weather event continues to be one of the largest ever recorded – across the activity spectrum.

For the evaluation of the threats of possible future solar flares, it is important to note that Cliver and Svalgaard (2004) concluded by saying “we should not be surprised if/when the space weather effects of future events exceed any or all of the current standards.”

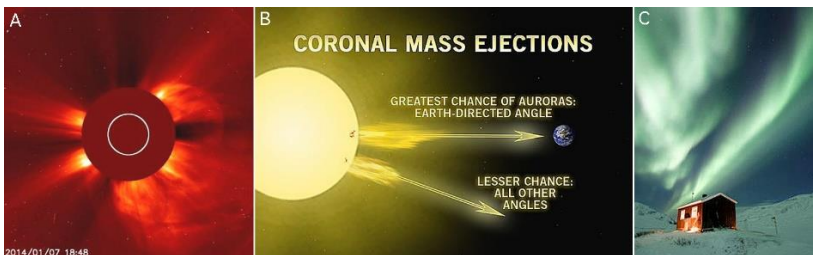
In recent years, giant solar flares have occurred in January 2014 and in March 2015.

The January 7 giant solar flare in 2014 is interesting because it can be linked to planetary conjunctions (Scafetta and Mörner 2014; Mörner et al., 2015). The triple conjunction of Venus, Earth and Jupiter is illustrated in Figure 1. The chain of events in the Sun-Earth interaction is shown in Figure 2. It is significant the coronal mass ejection was directed right towards the Earth, where spectacular aurora effects were recorded.



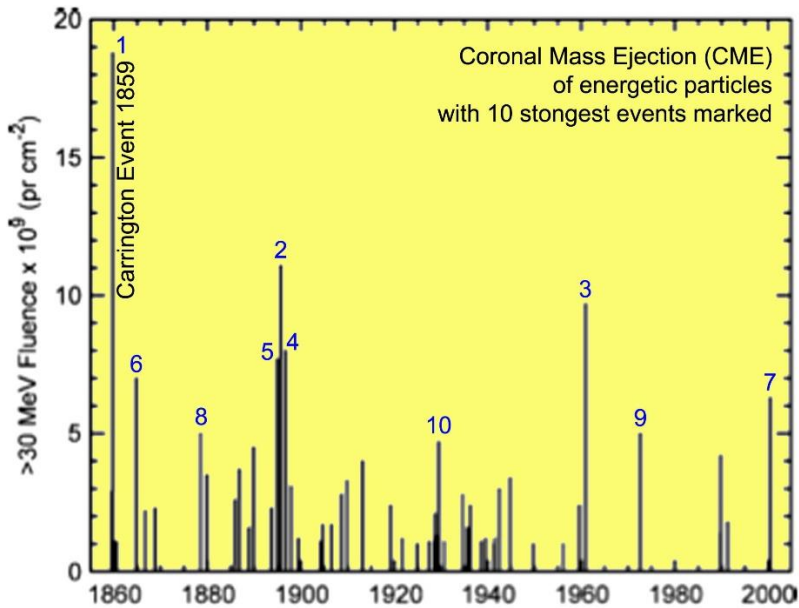
From Mörner et al., 2015.

Figure 1. (a) The giant solar flare in region AR1944 on January 7, 2014, (b) the triple planetary conjunction of Venus, Earth and Jupiter on January 7, and (3) the peak in the planetary tidal index of Scafetta (2012).



From Mörner et al., 2015.

Figure 2. The chain of events. A: coronal ejection January 7, B: coronal mass ejection with direct Earth direction, C: aurora at Abisko, north Sweden.



Modified from Cliver and Svalgaard, 2004.

Figure 3. Spectrum of solar flare events with fluences exceeding $30\text{MeV} \times 10^9\text{pr cm}^{-2}$.

The flow density and direction of coronal mass ejection (CME) of energetic particles seems to be the most significant parameter for the evaluation of threats to high-technology systems of human civilization. The spectrum of events from 1855 to 2000 is shown in Figure 3. It seems clear that the Carrington event in 1859 was an exceptionally strong event of energetic particle emission.

In general, the Carrington event has been considered to be some sort of a maximum solar flare event in our planetary system. This has recently changed with the discovery of stellar “superflares.”

Stellar Superflares

In 2015, a giant flare was reported in star KIC9655129 in the Milky Way with a magnitude 1000 times greater than any previously recorded flare (Pugh et al., 2015).

“Superflares” are large explosive events on stellar surfaces one to six orders-of-magnitude larger than the largest flares observed on the Sun

throughout the space age (Schaefer et al., 2000). Karoff et al., (2016) analysed 5648 solar-like stars, out of which 48 were superflare stars. They concluded: “*solar flares and superflares most likely share the same origin.*”

Whilst the Carrington event had an energy output of 5×10^{32} erg, superflares have energy output ranging from 10^{33} to 10^{38} erg according to Schaefer et al., (2000). Karoff et al., (2016) noted that 4 out of 30 superflare stars with energy outputs above 2×10^{34} have chromospheric emission levels comparable with the Sun (i.e., ~100 times greater than the Carrington event).

In conclusion, the Karoff group (Science Nordic 2016) found that the Sun’s magnetic field is capable of producing “small” superflares of magnitudes 100 times that of the Carrington event.

Aulanier et al., (2013), on the other hand, estimated the upper limit of solar flare energy at $\sim 6 \times 10^{33}$ erg, i.e., 10 times the energy of the Carrington event.

PAST GIANT SOLAR FLARES

In the geological-historical records of past changes on planet Earth, there might be traces of possible impacts from giant solar flares, too.

Nitrate spikes (NO_3^-) have been found to be indicative of supernovae events (e.g., Rood et al., 1979; Risbo et al., 1981; Motizuki et al., 2009).

Miyake et al., (2012) recorded a 1.2% spike in ^{14}C concentration within one single year in tree rings dated at AD 774/775. This generated a lot of discussion (e.g., Lovett 2012; Melott et al., 2012; Usaskin et al., 2013; Cliver et al., 2014; Jull et al., 2014; Miyake et al., 2015; Neuhäuser and Neuhäuser 2015; Mekhaldi et al., 2015). A similar event was also found in the tree rings of year AD 993/994 (Miyake et al., 2009; Mekhaldi et al., 2015).

Usoskin and Kovaltsov (2012) identified a number of “extreme solar particle events” (SPE) some of which might represent giant solar flares.

The most drastic claim of a giant solar flare event comes from LaViolette (2011). He proposed that in varve 12,837 \pm 10 years BP in the Cariaco Basin and nitrogen and ^{10}Be spikes in the GISP2 Greenland ice core are indicative of “a super-sized solar proton event,” which according to LaViolette (2011) was the ultimate cause of the mass extinction at the end of the Pleistocene.

Another special event is the Gothenburg Geomagnetic Flip (Mörner 1977; Mörner 2015a) at 12.400 C14-yrs BP (~16,500 cal.yrs BP), which implied a very rapid (maybe within some 15 years) shift of the VGP to an equatorial position. It coincides with a marked ^{10}Be peak, and is likely to represent a

major breakdown in Earth's geomagnetic shielding capacity or an exceptional large solar event. Finally, we have the drastic ^{14}C spike at about 2700 BP (Figure 4). This spike corresponds to a transpolar geomagnetic shift of 117° in 348 varve years at a mean rate of 0.36° per year (Mörner 2003). According to Dergachev et al., (2004), it represents a major geomagnetic excursion, with aurora borealis seen at down to the equator. It has the potential of representing a giant solar flare. In conclusions, there are multiple records of potential giant solar flare events in our geological-historical records. These "paleo-solar-flare events" are likely significantly to have exceeded the level of the Carrington event (according to Aulanier et al., 2013, by a factor of 10 and according to Karoff et al, 2016, by a factor of 100).

THE NEW THREAT

Giant solar flare events, 10-100 times stronger than the Carrington event implies a very severe increase in the level of threat such events would impose on life and human civilization on Earth (Mörner 2015b).

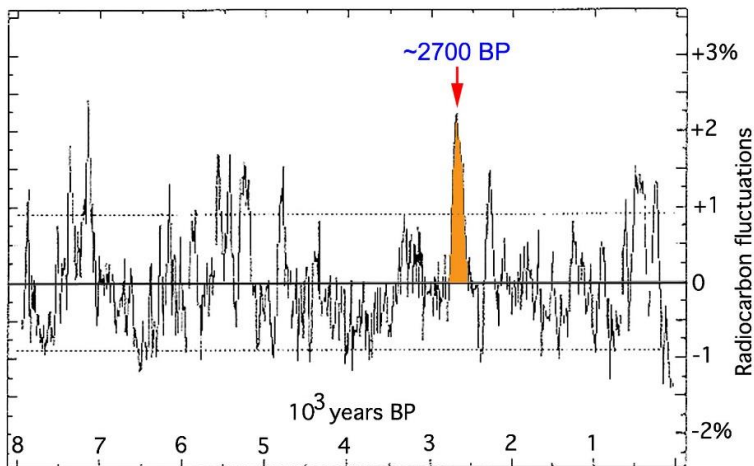


Figure 4. Fluctuations in atmospheric ^{14}C concentration during the last 8000 years with a spike at ~ 2700 BP. This spike corresponds to a geomagnetic excursion and a significant decrease in shielding capacity, which may signify a giant solar flare event. There are several other significant peaks (e.g., at 7125 BP, 7375 BP and 2280 BP) that might have a similar origin. At present, the 2700 BP spike is the only one linked to a major geomagnetic event, however.

Life and civilization on Planet Earth are constantly being threatened by different types of disastrous events; some are natural, some are man-made and some are just imagined. Some threats increase with our population growth and condensation to mega-cities and low-lying coastal areas. Plagues and famines have killed hundreds of millions of people through time. Here, the progress in medicine and human health care have changed the situation drastically. Some of our building constructions – dams for water and nuclear power plants for electricity – have emerged as new sources of man-made disasters. There are also a number of proposed disastrous processes that, in fact, are merely imagined, and products of our super-effective lobbying campaigns. Figure 5 illustrates the position of various disastrous threats in a triangle diagram bounded by natural, man-made and imagined disasters (from Mörner 2015b).

Threats to the Developed World

A giant solar flare 10-100 times stronger than the Carrington event would knock out our electronic systems; the electric supply would close down (no lamps, no heating, no cooking, etc.), the nuclear power plants would face approaching meltdowns, the GPS systems would break down, satellite communications would be lost, air planes may drop down, most cars would stop working, vital medical apparatuses would stop working, civil and military warning systems would become inoperative, banking would collapse, cell phones would be blocked, etc. etc. – the disaster of the developed world would be complete. We may well face a total collapse of “modern civilization.”

We can do nothing to prevent giant solar flares; if they come, they come. What we can do, however, is to prepare for how to cope in case of such an intensive giant solar flare that it would lead to disastrous effects on our electronic-electric systems on Earth (Parry 2015).

Native Communities

Depending upon the degree of electric and electronic utilization, native communities in various parts of the world may more or less unaffected pass a giant solar flare event, however. As to developing countries, the effects will depend on the degree of modernization and dependence of assistance from the industrialized world.

21 CO2-driven Global Warming, 22 Disastrous sea level rise, 23 Ocean acidification

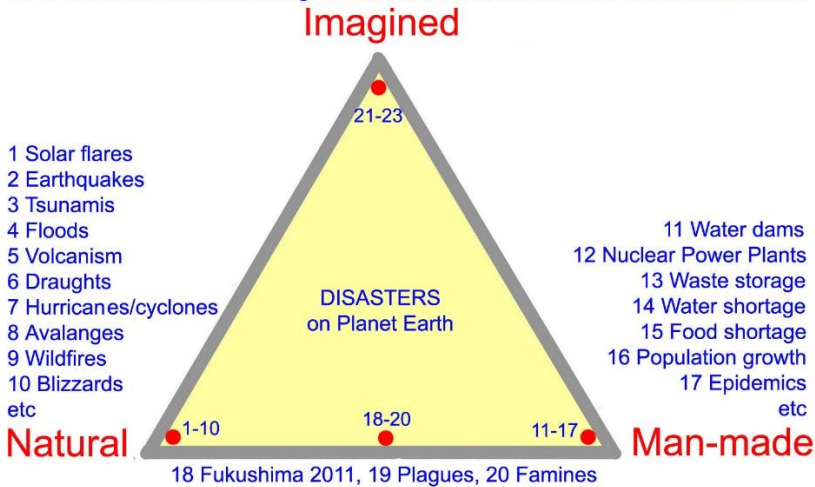


Figure 5. Planetary disasters group as natural, man-made and imagined (Mörner, 2015b). With the discovery that solar flare events 10-100 times as strong as the Carrington event in 1859, solar flares have recently emerged as one of the worst threats in the group of natural disasters.

Mega-Cities

Mega-cities are very vulnerable to changes. A giant solar flare affecting the global electric and electronic systems would be disastrous for the infrastructure and individual survival capacity.

Purgatorium in Dante's Divina Commedia would be brought to the surface of the Earth.

Panic and Chaos

In a worse case breaking down of our modern living conditions (electric energy, communications, traffic, banking, computers, medical care, warning systems, etc.) panic and chaos will inevitably spread like a tsunami wave. This, in its turn, is likely to kick off various types of violence.

In view of this, it is quite positive that the U.S. Government is now "preparing for a catastrophic solar flare, which could wipe out power across the world for months" (Parry 2015).

CONCLUSION

The Carrington giant solar flare event in 1859 struck the world in pre-electric and pre-electronic time; only the telegraph systems broke down. A similar event hitting the Earth today would have disastrous effects. But it is even worth; after analysing stellar supernovae and terrestrial records of “paleo-solar-flare” events, we must conclude that the Earth may experience solar flare events in the future of magnitudes 10 to 100 times that of the Carrington event.

In view of this, solar flares may now be considered *the Greatest Threat to Modern Life on Earth*.

REFERENCES

- Aulanier, G. et al., 2013. The standard flare model in three dimensions. II. Upper limit on solar flare energy. *AandA*, 549, A66.
- Carrington, R. C., 1859. Description of a singular appearance seen in the Sun on September 1, 1859. *Monthly Notices of the Royal Astronomical Society*, 20, 13-15.
- Cliver, E. W. and Svalgaard, L., 2004. The 1859 solar-terrestrial disturbance and the current limits of extreme space weather activity. *Solar Physics*, 224, 407-422.
- Cliver, E. W., Tylka, A. J., Dietrich, W. F. and Ling, A. G., 2014. On a solar origin for the cosmogenic nuclide event of 775A.D. *Astrophys. J.*, 781, 32.
- Dergachev, V. A., Raspopov, O. M., van Geel, B. and Zaitseva, G. I., 2004. The “Sterno-Etrussian” geomagneti excursion around 2700 BP and changes of solar activity, cosmic ray intensity, and climate. *Radiocarbon*, 46, 661-681.
- Jull, A. J. T. et al., 2014. Excursions in the ^{14}C record at A.D. 774-775 in tree rings from Russia and America. *GRL*, 41, 3004–3010.
- Karoff, C. and 13 others, 2016. Observational evidence for enhanced magnetic activity of superflare stars. *Nature Communications*, 24 Mar 2016, DOI: 10.1038/ncomms11058.
- LaViolette, P. A., 2011. Evidence for a solar flare cause of the Pleistocene mass extinction. *Radiocarbon*, 53, 303-323.
- Lovett, R. A., 2012. Mysterious radiation burst recorded in tree rings. *Nature News and Comment*, 03 June 2012.

- Mekhaldi, F. et al., 2015. Multiradionuclide evidence for the solar origin of the cosmic-ray events of AD 774/5 and 993/4. *Nat. Commun.*, 6, 8611.
- Melott, A. L. and Thomas, B. C., 2012. Causes of an AD 774-775 ^{14}C increase. *Nature*, 491, E1–E2 (2012).
- Miyake, F., Nagaya, K., Masuda, K. and Nakamura, T., 2012. A signature of cosmic-ray increase in AD 774-775 from tree rings in Japan. *Nature*, 486, 240–242.
- Miyake, F., Masuda, K. and Nakamura, T., 2013. Another rapid event in the carbon-14 content of tree rings. *Nat. Commun.*, 4, 1748.
- Miyake, F. et al., 2015. Cosmic ray event of A.D. 774-775 shown in quasi-annual ^{10}Be data from the Antarctic Dome Fuji ice core. *GRL*, 42, 84–89.
- Mörner, N.-A., 1977. The Gothenburg Geomagnetic Excursion. *Quaternary Res.*, 7, 413-427.
- Mörner, N.-A., 2003. The 2700 BP solar-terrestrial signal. *EGS-AGU-EGU meeting*, Nice 2003, Abstract ST1.
- Mörner, N.-A., 2015a. Threats and Disasters on Planet Earth. *International Journal of Engineering Research and Science*, 1 (9), 43-46.
- Mörner, N.-A., 2015b. The Bölling/Alleröd – Younger Dryas oscillation. In: *Planetary Influence on the Sun and the Earth, and a Modern Book-Burning*, N.-A. Mörner, ed., Chapter 7, p. 79-90. Nova Sci. Publ.
- Mörner, N.-A., Scafetta, N. and Solheim, J.-E., 2015. The January 7 Giant Solar Flare, the simultaneous triple planetary conjunction and additional records at Tromsø, northern Norway. *Planetary Influence on the Sun and the Earth, and a Modern Book-Burning*, p. 33-38. Nova Science Publishers.
- Motizuki, Y. and 10 others, 2009. An Antarctic ice core recording both supernovae and solar cycles. *arXiv: 0902.3446*.
- Neuhäuser, R. and Neuhäuser, D. L., 2015. Solar activity around AD 775 from aurorae and radiocarbon. *AN*, 336, 225–248.
- Parry, H., 2015. White House is preparing for catastrophic solar flares which could wipe out power around the world for months – bringing an end to modern civilization as we know it. *Daily Mail Online*, 3 November, 2015.
- Pugh, C. E., Nakariakov, V. M. and Broomhall, A.-M., 2015. A multi-period oscillation in a stellar super-flare. *AAS Astrophysical Journal Letters*, 813 (1), L5. <http://dx.doi.org/10.1088/2041-8205/813/1/L5>.
- Risbo, T., Clausen, H. B. and Rasmussen, K. L., 1981. Supernovae and nitrate in the Greenland Ice Sheet. *Nature*, 294, 637–639.
- Rood, R. T., Sarazin, C. L., Zeller, E. J. and Parker, B. C., 1979. X- or γ -rays from supernovae in glacial ice. *Nature*, 282, 701–703.

-
- Scafetta, N. and Mörner, N.-A., 2014. The giant solar flare event of January 7, 2014, in light of the planetary theory of solar variability. *Pattern Recogn. Phys.*, 2 (2), 31-34. <http://www.pattern-recognition-in-physics.com>.
- Schaefer, B. E., King, J. R. and Deliyannis, C. P., 2000. Superflares on ordinary solar-type stars. *Astrophys. J.*, 529, 1026-1030.
- Science Nordic, 2016. Sun can emit superflare every 1000 years. Posted on line 29 April, 2016. <http://sciencenordic.com/>.
- Usoskin, I. G. and Kovaltsov, G. A., 2012. Occurrence of extreme particle events: assessment from historical proxy data. *Astrophys. J.*, 757 (2), 1-6.
- Usoskin, I. B. G. et al., 2013. The AD 775 cosmic event revisited: the Sun is to blame. *AandA*, 552, L3.

Chapter 2

**ELECTRON DENSITY CHARACTERISTICS
IN IONOSPHERIC D-REGION
DURING SOLAR X-RAY FLARE**

*Aleksandra Nina**

Institute of Physics, University of Belgrade, Belgrade, Serbia

Abstract

Solar X-ray flares play a very important role in the lower ionosphere dynamics. Previous researches have shown that the electron density, as one of the most important plasma parameters in ionospheric investigations, can change by one or two orders of magnitude under the influence of the considered X-radiation in the lowest part of the ionosphere called the D-region. These changes are correlated with other parameters and must be known in various calculations needed in analyses of the ionospheric plasma properties. Among others, they represent changes in characteristics of the medium which are relevant to propagation of electromagnetic waves including telecommunication signals whose use is unavoidable in numerous aspects of the contemporary way of living. For these reasons the analyses of electron density variations are very important in both the pure scientific studies and practical applications in technology, and they represent the connection between the space weather and its influence on the Earth, and our daily life. In this research we present a study of time and space variations of electron density characteristics during a solar X-ray flare influence. The attention is focused on the electron

*E-mail address: sandrast@ipb.ac.rs

density and its time and altitude derivatives which are the most relevant parameters for various further analyses and various practical applications. To show the main characteristics of the D-region response to the incoming X-radiation increase we compare time evolutions of the X-ray intensity detected by the GOES satellite with electron density properties, and point out differences during their specific phases. The calculations of the electron density are based on the low ionosphere monitoring by very low frequency (VLF) radio waves and, in the presented research, we process data related to the amplitude and phase of a signal emitted by the DHO transmitter in Germany and received in Serbia.

1. Introduction

As a part of the terrestrial atmosphere the ionosphere is under permanent influence of different natural perturbers located in different parts of space (solar radiations (Nina et al., 2011; Nina and Čadež, 2013), gamma ray bursts (Inan et al., 2007; Nina et al., 2015a), terrestrial atmosphere (lightnings (Inan et al., 2010), atmospheric convective motions (Šindelářová et al., 2009), tropical cyclones (Peter and Inan, 2005)), terrestrial lithosphere (tectonic motions coming from the interior of the Earth) (Astafyeva and Afraimovich, 2006; Dautermann et al., 2009), and ocean motions including tsunamis (Rozhnoi et al., 2012). In addition to natural perturbers, there also exist those caused artificially by human modern technology such as, for example, rocket launchings (Kiryushkin et al., 2008), nuclear (Yang et al., 2012) and chemical explosions (Drobzheva and Krasnov, 2003). The ionosphere is therefore a medium of a highly complex nature concerning numerous physical, chemical and geometrical features that govern its versatile dynamics on various spatial and temporal scales.

The intensity of ionospheric disturbances and their duration depend on particular event properties. However, the solar radiation has the most important global influence on the ionosphere and solar X-ray flares produce one of the most pronounced changes in the ionospheric plasma which can last for several tenths of minutes. For this reason, the research of ionospheric responses to the intensification of solar X-radiation is in focus of numerous scientific studies.

The ionospheric research has versatile applications. In addition to pure scientific importance and possible utilization of ionospheric disturbances as precursors of natural disasters, a significant role of the ionosphere in modern human life is manifested in telecommunication technologies. For example, signals emitted from satellites and detected by the ground receivers are greatly influ-

enced by the ionospheric conditions (Kintner and Ledvina, 2005). Then, the long range radio communication at ground can be achieved owing to the property of the ionosphere to refract and reflect radio waves with frequencies up to few MHz depending on the part of the day. In addition to the possibility of communication, the HF frequency range (3-30 MHz) link establishment is being increasingly used also for the development of the so-called Over-The-Horizon Radar (OTHR) systems (Reinisch et al., 1997) for object detections.

As studies indicate, intensity of ionospheric perturbations induced by solar X-ray flares strongly depends on location which, as a result, changes the profile of electron density altitude distributions in time. Namely, the relative increase of radiation following such an event is more influential in the lower than in the upper ionosphere. This is concluded in investigations showing that not too intensive X-ray flares produced practically no changes to the columnal electron number density, called total electron content (TEC), described primarily by the F-region plasma. Here the electron density has the highest values in quiet conditions while during a very intensive increase of X radiation the height of the electron density maximum can be lowered to the E-region (Xiong et al., 2011). On the other side, at the same time, the electron density increases in the D-region altitudes (60 km - 90 km) by more than one order of magnitude (Nina et al., 2012a,b; Singh et al., 2014). For these reasons we can conclude that during solar X-ray flares of classes C and M more intensive perturbations are in the lowest ionospheric region - D-region and the analyses of this chapter are focused on the plasma of this area.

The theoretical equations for calculations of the electron density and its space and time variations are applied to an example of the low ionospheric perturbation induced by the solar X-ray flare that occurred on May 5, 2010. The electron density time and altitude dependencies are calculated from data obtained by the D-region monitoring using VLF radio signals emitted by the DHO transmitter located in Germany and recorded in Serbia by the AWESOME (Atmospheric Weather Electromagnetic System for Observation Modeling and Education) receiver (Cohen et al., 2010) within the Stanford/AWESOME Collaboration for Global VLF Research activities.

2. Observations

The technique of atmospheric monitoring depends on altitude of the considered medium. The location of the low ionosphere lies below the area being studied

by satellite observations and above the region where balloon measurements find their application. Its monitoring is based on rocket and radar measurements (Strelnikova and Rapp, 2010; Chau et al., 2014), and on technology involving the propagation of very low and low frequency (VLF/LF) radio waves. In this chapter we utilize the technique that uses data related to amplitude and phase of a VLF/LF signal recorded at the ground after the signal deflection from the ionosphere at heights below 90 km. This method is based on the fact that the considered signals propagate through the low ionosphere which affects characteristics of their propagation and, consequently, the shapes of registered VLF/LF wave variations in real time which indicates the presence of non-stationary physical and chemical conditions in the perturbed medium along the VLF/LF wave trajectories (for details see, for example Nina et al. (2011, 2012b)). Namely, perturbations make the local electron density and, consequently, the height of the wave reflection, time dependent (Nina et al., 2012a) which further alters the VLF/LF wave trajectory and causes the registered wave amplitude and phase time dependencies.

The global experimental setup for the VLF/LF monitoring technique consists of numerous transmitters and receivers distributed worldwide that enable observations of a large part of the low ionosphere and detections of local plasma perturbation patterns in the D-region. A number of the receivers are incorporated in some international networks like AWESOME (Cohen et al., 2010), SAVNET (Raulin et al., 2009) and AARDDVARK (Clilverd et al., 2009). A very important characteristic of this technique for ionospheric monitoring is a continuous emission and reception of radio signals with a very good time resolution (less than 1 s) allowing detections of sudden, and consequently non precisely predicted, events, as well as detection of short term ionospheric reactions.

To determine time and altitude dependencies of the electron density and its time and vertical derivatives we chose data for the 23.4 kHz VLF radio signal emitted by the DHO transmitter in Rhaderfehn (Germany) and recorded by the AWESOME VLF receiver located in Institute of Physics in Belgrade (Serbia) whose propagation path is shown in Fig. 1. The reason why we chose this signal (like in other our works) is the best quality of its recorded data due to the high emission power of the DHO transmitter (800 kW) and a relatively short signal propagation path. The latter property is important as it allows us to assume a quasi uniform horizontal plasma conditions along the signal trajectory.

To present how solar X-ray flares influence the low ionosphere we analyse

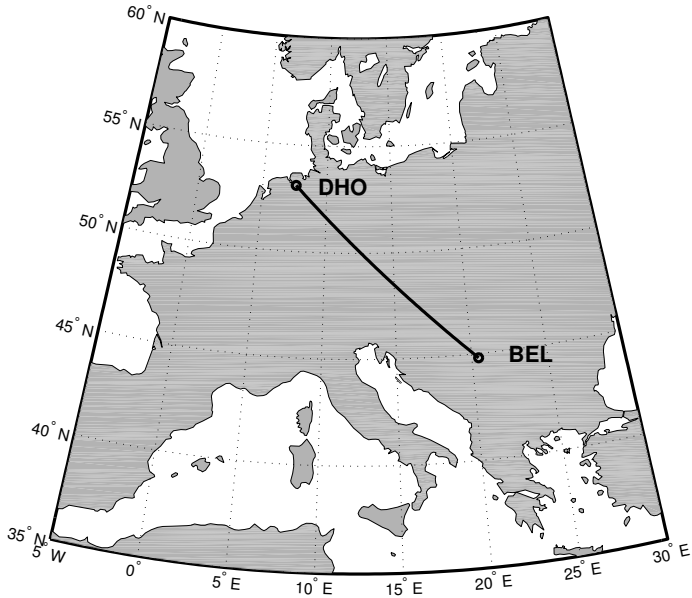


Figure 1. 23.4 kHz signal propagation path from Rhauderfehn (Germany) to Belgrade (Serbia).

an example of electron density variation between 11:40 UT and 12:50 UT, May 5, 2010 in presence of a particular flare recorded as a solar radiation increase within the wavelengths range 0.1 nm - 0.8 nm as shown in Fig. 1, the upper panel. The used data for the photon flux $I(t)$ are recorded by the National Oceanic and Atmospheric Administration (NOAA) satellite GOES-14 (http://satdat.ngdc.noaa.gov/sem/goes/data/new_full/2010/05/goes14/csv/g14_xrs_2s_20100505_20100505.csv). The corresponding amplitude $A_{rec}(t)$ and phase $P_{rec}(t)$ time variations of the recorded signal are shown in the Fig. 2 and their role in calculations of the electron density properties are explained in the next section.

This flare provoked a typical ionospheric reaction without visible additional influences of other possible perturbors as can be concluded from very smooth tendency of the amplitude and phase time evolution curves with monotonously increasing/decreasing domains (Fig. 2). In addition, it was not too intensive (class C8.8) so that this analysis also argues the need to include also the ef-

fects of less intensive ionospheric perturbers. For example, as our investigations show, these effects are not negligible and they contribute to total electron content (TEC) variations which are used in descriptions of measurements based on the satellite signal propagations (Todorović Drakul et al.). Of course, the induced changes are also very important in analyses of the ground-ground radio signal propagations in a wide frequency domain which is described in many studies (Bajčetić et al., 2015) This is important for practical applications because the X-ray flares of class C (X-ray emission in 0.1 nm - 0.8 nm with the maximum intensity of 10^{-6} W/m² - 10^{-5} W/m²) are more frequent than those of classes M and X (X-ray emission in 0.1 nm - 0.8 nm with the maximum intensity of 10^{-5} W/m² - 10^{-4} W/m² and above 10^{-4} W/m², respectively). This is noticed during the entire solar cycle period. For example, the GOES satellite recorded 28 and 0 events of C and M class solar X-ray flares, respectively, in 2009 (the solar cycle minimum), while the corresponding numbers were 1797 and 207 in 2014 (the solar cycle maximum).

For the reasons mentioned above, we treated the considered flare event in other analyses on several earlier occasions (Nina and Čadež, 2014; Bajčetić et al., 2015; Nina et al., 2015b; Todorović Drakul et al.).

3. Theory

The increase in incoming X-radiation during solar X-ray flares results in changes of numerous processes and properties of ionospheric plasma parameters. Namely, although the larger photoionization rate is the primary effect of solar X-ray flares, initial variations in the density of the local plasma constituents and temperature variations influence other processes among which the recombination processes are the most important in the D-region. As a consequence, the densities of particular plasma constituents become time dependent and affect the different phenomena occurring in this medium like propagation of the electromagnetic waves. Keeping in mind that the role of electrons is very important in different scientific studies and in practical applications of the ionospheric research in telecommunication, we focus here our attention on analysis of various aspects of this plasma constituent.

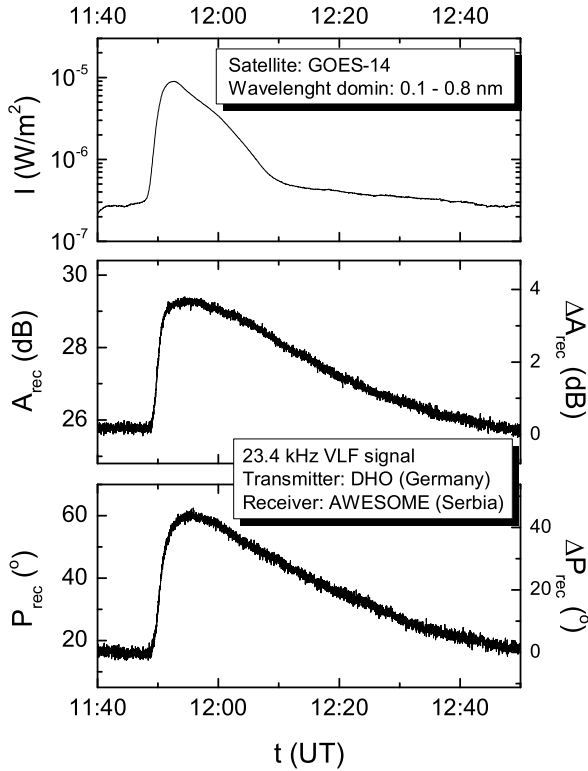


Figure 2. Time dependencies of the X radiation intensity I registered by the GOES-14 satellite in the wavelength domain between 0.1 and 0.8 nm (top panel), signal amplitude A_{rec} (middle panel) and phase P_{rec} (bottom panel) registered by the AWESOME receiver located in Belgrade (Serbia) during presence of the solar X- are occurred on May 5, 2010. The signal characteristic changes ΔA_{rec} and ΔP_{rec} are shown in the right axes in middle and bottom panels, respectively.

3.1. Electron Density Modeling in the D-Region

In this study we use the method for the electron density modeling during a X-ray flare given in Grubor et al. (2008) and also used in many other papers (see for

example Žigman et al. (2007); Kolarski et al. (2011); Nina et al. (2012a); Nina et al. (2015b)). This technique is based on matching the observed VLF signal data of the amplitude ΔA_{rec} and phase ΔP_{rec} changes with corresponding results of numerical simulations ΔA_{sim} and ΔP_{sim} of the VLF signal propagation. In this way we apply the theoretical and numerical models to experimentally data and to the obtained D-region electron density time and space distributions for the considered time period and the considered location.

3.1.1. Observing of Changes in VLF/LF Signal Characteristics

As we can see in Fig. 2, two middle panels, the observations by the used technique based on propagation of radio waves give information about time evolutions of amplitude A_{rec} and phase P_{rec} of the signal recorded by the VLF/LF radio receiver. The registered amplitude ΔA_{rec} and phase ΔP_{rec} changes are determined relative to the corresponding values under unperturbed conditions A_{rec}^0 and P_{rec}^0 , respectively:

$$\Delta A_{\text{rec}}(t) = A_{\text{rec}}(t) - A_{\text{rec}}^0. \quad (1)$$

$$\Delta P_{\text{rec}}(t) = P_{\text{rec}}(t) - P_{\text{rec}}^0. \quad (2)$$

In our case, these initial values reach $A_{\text{rec}}^0 = 25.6$ dB and $P_{\text{rec}}^0 = 16.2^\circ$ respectively.

3.1.2. Modeling Changes in VLF/LF Signal Characteristics

To model the time variations of amplitude and phase during the perturbed period we use the Long-Wave Propagation Capability (LWPC) numerical model developed by the Naval Ocean Systems Center (NOSC), San Diego, USA (Ferguson, 1998). This model is based on Wait's model of the horizontally stratified ionosphere (Wait and Spies, 1964) which is characterized by two independent parameters: the "sharpness" β and the signal reflection height H' . These parameters are the inputs for the LWPC numerical program that calculates the simulated values for the recorded amplitude $A_{\text{sim}}(\beta, H')$ and phase $P_{\text{sim}}(\beta, H')$ of the considered signal and receiver location. Their changes $\Delta A_{\text{sim}}(\beta, H')$ and $\Delta P_{\text{sim}}(\beta, H')$ with respect to values $A_{\text{sim}}(\beta_0, H'_0)$ and $P_{\text{sim}}(\beta_0, H'_0)$ in the initial period of the quiet ionospheric state are calculated using the approximative values $\beta_0 = 0.3 \text{ km}^{-1}$ and $H'_0 = 74 \text{ km}$ for Wait's parameters during the unperturbed conditions. These values are also used in numerous pervious studies

(Grubor et al., 2008; Nina et al., 2011, 2012a,b; Nina and Čadež, 2014). The corresponding expressions for changes of simulated VLF/LF signal amplitude and phase are then:

$$\Delta A_{\text{sim}}(\beta, H') = A_{\text{sim}}(\beta, H') - A_{\text{sim}}(\beta_0, H'_0) \quad (3)$$

and

$$\Delta P_{\text{sim}}(\beta, H') = P_{\text{sim}}(\beta, H') - P_{\text{sim}}(\beta_0, H'_0). \quad (4)$$

Here it is important to say that there exist several studies of how to determine the initial Wait's parameters. However, the detailed analysis given in Nina and Čadež (2014) for three solar X-ray fares including the analysed event based on results presented in McRae and Thomson (2000), Friedrich and Torkar (2001), and Han et al. (2011) shows that the resulting variations within the D-region are practically negligible and the obtained electron densities are not significantly different from those calculated for the pair of Wait's parameters which we use. The same conclusion is also obtained in Žigman et al. (2007) using a comparison with the procedure shown in McRae and Thomson (2000).

3.1.3. Matching the Observed and Modeled VLF/LF Signal Data

The criterion for numerical determination of the parameters β and H' in time t is the condition of the best fitting the experimental data with their numerical counterparts:

$$\Delta A_{\text{sim}}(\beta, H') \approx \Delta A_{\text{rec}}(t), \quad (5)$$

$$\Delta P_{\text{sim}}(\beta, H') \approx \Delta P_{\text{rec}}(t). \quad (6)$$

The electron density in time t and at altitude h can finally be calculated from the equation (Thomson, 1993):

$$N_e(h, t) = 1.43 \cdot 10^{13} e^{-\beta(t)H'(t)} e^{(\beta(t)-\beta_0)h}, \quad (7)$$

where N_e is in m^{-3} , $H'(t)$ and h are in km, β is in km^{-1} and $\beta_0 = 0.15 \text{ km}^{-1}$.

3.2. Modeling the Electron Density Time and Altitude Variations in the D-Region

The knowledge on the electron density in space and time is needed to calculate some plasma parameter properties like the effective recombination coefficient

(Nina et al., 2012b), electron production and loss rate (Nina and Čadež, 2014), contribution of the Ly α line influence in the ionization process at the X-ray flare intensity maximum (Nina et al., 2015b). Also, it is involved in modeling the plasma parameters such as the electron plasma frequency and index of refractivity (Bajčetić et al., 2015) needed to simulate the propagation of electromagnetic waves in the low ionosphere. In these simulations, the electron density changes in space, e.g. its gradient with altitude in the case of horizontal stratified ionosphere, is included in calculation. For this reason our attention in this study is focus to the properties of both electron density and its gradient.

The time dependence of the electron density gradient is analytically calculated using Eq. (7):

$$\frac{dN_e(h, t)}{dh} = 1.43 \cdot 10^{13} e^{-\beta(t)H'(t)} \frac{1}{\beta(t) - \beta_0} e^{(\beta(t) - \beta_0)h} = \frac{1}{\beta(t) - \beta_0} N_e(h, t), \quad (8)$$

In this study we first calculate numerically the derivatives $\frac{dN_e}{dh}$ and $\frac{d^2 N_e}{dh dt}$ and then $\frac{d^2 N_e}{dh dt}$ and $\frac{d^3 N_e}{dh dt^2}$ using the general numerical scheme:

$$\frac{f(h, t)}{dt} = \frac{f(h, t + \Delta t) - f(h, t - \Delta t)}{2\Delta t} \quad (9)$$

with the time step Δt is defined as the time resolution of used input data. In computations that follow, we take $\Delta t = 1$ s.

4. Results and Discussion

To apply the procedures explained in Section 3 we used data extracted from the DHO VLF signal recorded by the AWESOME receiver system in Belgrade, Serbia, at the time period of the ionospheric perturbations induced by the solar X-ray flare that occurred on May 5, 2010 (see Fig. 2).

As we can see from Eq. (7) the first step in data processing is to determine time evolutions of Wait's parameters. These values are obtained as final result of the numerical procedure for comparison of the recorded amplitude and phase variations with their computed values by LWPC numerical program for simulation of the VLF radio signal propagation (Ferguson, 1998) (explained in subsection 3.1). On the other hand, they represent the initial values for the electron density calculation by analytical expression and further used in different theoretical analyses. For these reasons we first present the obtained values for β and H' .

The knowledge of these time distributions allows us to calculate the electron density and its gradient using equations Eq. (7) and Eq. (8), and their first and second time derivatives according to Eq. (9). Here we separate the presentation of obtained time and altitude dependencies in three parts related to: 1) the electron density and its gradient, 2) their first time derivatives, and 3) their second time derivatives, respectively. In these analyses we first show the 3D graph of the considered value and its contour plot. After that, to point out its time evolution and altitude distributions, we plot corresponding dependencies for fixed altitudes and times, respectively.

Keeping in mind that considered values vary by several orders of magnitude, we present the obtained results in a log scale. For this reason, the negative values are separated and visualized as their absolute values. Also, we divide the considered quantities by their dimensional unit values to obtain correct expressions of mathematical forms. The details are given in the figure captions.

4.1. Determination of Wait's Parameters

According to Eq. (5) and Eq. (6), the obtained pairs of Wait's parameters are time dependent $\beta = \beta(t)$ and $H' = H'(t)$ as presented in Fig. 3 for the considered case. Here it can be seen that the VLF wave reflection height $H'(t)$ initially decreases in time, reaches a minimum and then rises again and returns to the approximately same value as in the period before the solar X-ray flare. The sharpness $\beta(t)$, characterizing the vertical gradient of the electron density, has a reversed time distribution, i.e. it first increases and attains a maximum at the same time when $H'(t)$ has its minimum. As in the case of H' , it finally reaches values that are very close to those from the period before the ionospheric perturbation. Here we can also see the presence of the diurnal variation in the incoming solar radiation in the D-region which primarily determines changes in the local plasma properties and does not allow the ionospheric parameters and, consequently, the signal path properties to fully return to the initial state.

As variations in the recorded quantities represent a summary effect of the time dependent influences of different perturbors, the derived values for $\beta(t)$ and $H'(t)$ are not smooth functions of time t . Consequently, the time derivative of the electron density as a function of these parameters is practically random and cannot represent the major influence of the solar X-ray flare. Because of that it is needed to fit the obtained discrete values of $\beta(t)$ and $H'(t)$ by smooth functions. In this study we use a continuous model function implemented in

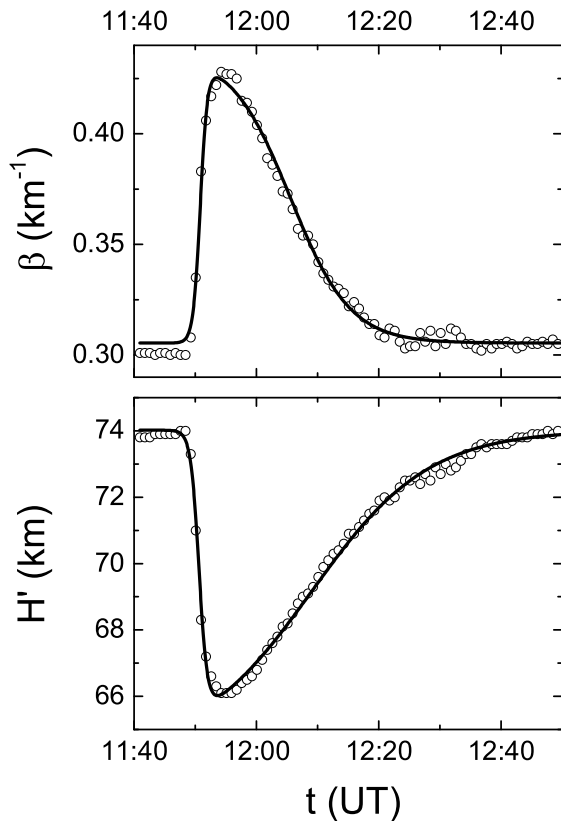


Figure 3. Time dependencies of the calculated Wait's parameters β (upper panel) and H' (bottom panel) during presence of the solar X- are occurred on May 5, 2010.

the Origin-8 program, also found in the NAG (Numerical Algorithms Group) library:

$$y = y_0 + \frac{A}{1 + e^{-\frac{x-x_c+w_1/2}{w_2}}} \left(1 - e^{-\frac{x-x_c+w_1/2}{w_3}} \right) \quad (10)$$

where x stands for time t in seconds starting from 11:40:00 UT and y stands for $\beta(t)$ and $H'(t)$. The numerical fitting constants y_0 , A , x_c , w_1 , w_2 and w_3 related to the considered physical quantities y in Eq. (10) were obtained as the

Table 1. Parameters used in Eq. (10)

y	y_0	A	x_c (s)	w_1 (s)	w_2 (s)	w_3 (s)
$\beta(t)$ (km)	0.30543	0.13129	0.49875	0.01023	4.03695E-4	0.00339
$H'(t)$ (km ⁻¹)	74.02009	-9.69627	0.4999	0.01281	4.68902E-4	0.00662

numerical program outputs and are presented in Table 1. So derived continuous time dependent functions will now be used in calculations of $N(h, t)$ and its characteristics.

Here we point out that the chosen function describes the whole period of the D-region perturbation because the implementation of a continuous function within the considered time interval is important for calculation of time derivatives. However, the analyses related to the specific phases of the ionospheric perturbation period, such as, for example, the duration of the solar X-ray flare intensity maximum (Nina et al., 2015b), and the D-region plasma relaxation (Nina and Čadež, 2014), allow application of other fitting functions which are more adequate for shorter time intervals.

4.2. Time and Altitude Distributions of the Electron Density and Its Vertical Gradient

The electron density $N_e(h, t)$ is calculated applying Eq. 7 to the fitted smooth functions $\beta(t)$ and $H'(t)$. The altitude and temporal dependencies of the resulting modeled electron density are shown in Fig. 4, the left upper panel, while a better visibility of the quantitative changes is achieved by the contour plot presented in the bottom left panel. Here it can be seen that the most pronounced electron density variation with height occurs at the time of the electron density maximum when it rises by three orders of magnitude, and that the maximum increase relative to the initial value is obtained at 90 km (by more than a factor of 250). In quiet conditions, altitude changes are between the order of magnitudes of $10^6 - 10^8 \text{ m}^{-3}$.

The obtained changes are consequences of variations in the rates of numerous chemical processes in the D-region plasma. Namely, the local electron density depends here on the ionization, through the electron gain and electron

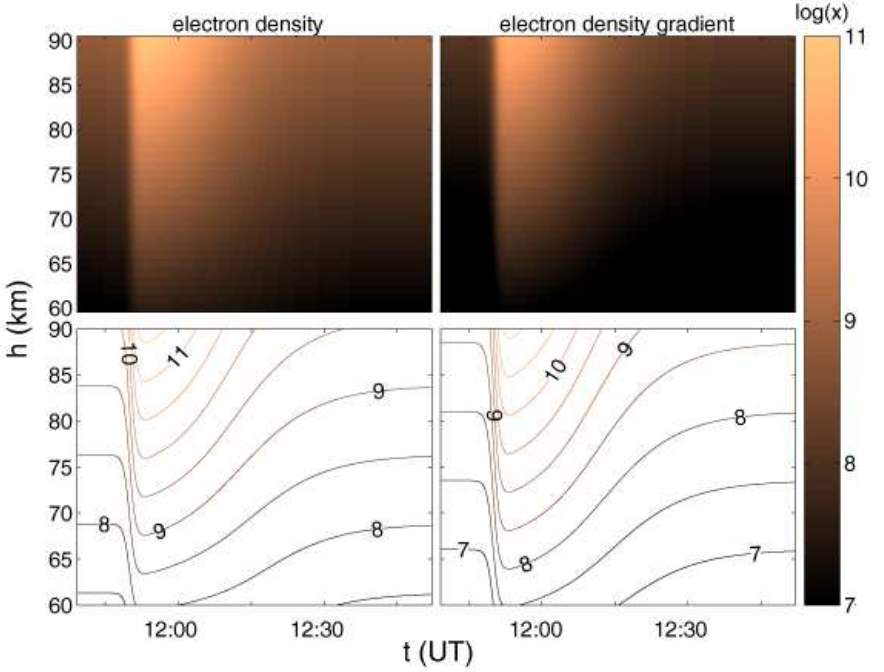


Figure 4. Surface (upper graphs) and contour (bottom graphs) plots of the electron density (left panels) and the electron density gradient normalized to their unit values $N_e^0 = 1 \text{ m}^{-3}$ and $(dN_e/dh)^0 = 1 \text{ m}^{-3}\text{km}^{-1}$, respectively, as a function of time t and altitude h during the considered solar X-ray flare. The plotted values x are calculated using equations $x = \log(N_e^*(t, h)) = \log(N_e/N_e^0(t, h))$ (left panels) and $x = \log((dN_e/dh)^*(t, h)) = \log((dN_e/dh)(t, h)/((dN_e/dh)^0(t, h)))$ (right panels).

loss processes:

$$\frac{dN_e(r, t)}{dt} = G(\vec{r}, t) - L(\vec{r}, t), \quad (11)$$

where G and L are the rates of the electron production, and loss, respectively. Eq. (11) is the general form in which the influence of transport processes is neglected as they become important at altitudes above 120-150 km (Blaunstein and Christodoulou, 2006) and they are generally not included in models of the D-region plasma (Turunen et al., 1992; William and Foley, 1978). The ioniza-

tion in the unperturbed bottom part of the D-region is primarily induced by cosmic radiation while the $\text{Ly}\alpha$ photons coming from the Sun is the major source of ionization of the lowest ionospheric region in quiet conditions. However, the X-radiation dominates in the electron production when the radiation in this frequency domain is sufficiently large (Nina et al., 2015b). For this reason we can assume the photoionization to be the major ionization process during the solar X-ray flare. On the other side, recombination processes play very important role in the electron loss rate. For example, at heights around 70 km, the dominant recombination processes are the electronion, ionion and three-body recombination characterized by a common effective recombination coefficient (Žigman et al., 2007). In the case of unperturbed, quasi-stationary ionosphere, the electron gain and electron loss processes are in equilibrium, i.e. mutually balanced. During a solar flare, the electron density is raised due to the increased photoionization and this time period can be named as the photoionization (P) regime. After a flare maximum when the rate of recombination becomes larger than the photoionization rate, the electron concentration starts to decrease and the ionosphere enters a recombination (R) regime (Nina et al., 2012b). These regimes are clearly visible in Fig. 5, the upper left panel, where we can see that the R-regime is lasting longer than the P-regime. The Wait's model of ionosphere gives an exponential altitude dependency of the electron density in both regimes as can be seen in the bottom left panel of this figure.

Comparing Figs. 2, the upper panel, and 3 and 5 it can be noticed that the time distribution of Wait's parameters and, consequently, the electron density, follow the time variation pattern of the solar flux recorded on the GOES-14 satellite which is visible in the initial period (the start of ionospheric perturbations and signal deviation), of the part of the relevant variations of maxima, and, finally in the time of the return of the considered time evolutions to the unperturbed state. The explanation of these delays can be made by using the equation for the electron density Eq. (11) in the form:

$$\frac{dNe(r, t)}{dt} = G_0(\vec{r}, t) + K(\vec{r}, t)I(t) - \alpha_{\text{eff}}(\vec{r}, t)N_e^2(\vec{r}, t). \quad (12)$$

Here, $G_0(\vec{r}, t)$ is the initial electron gain rate for ionization processes where the X-radiation is not involved because its negligible effect, the parameter $K(\vec{r}, t)$ is the electron gain scaling coefficient for satellite data on the X-radiation intensity, $K(\vec{r}, t)I(t)$ is the electron gain rate for the X-radiation, $\alpha_{\text{eff}}(\vec{r}, t)$ represents the electron gain scaling coefficient (it is considered as the effective recombination coefficient for ionized plasma constituents in the case when the influence

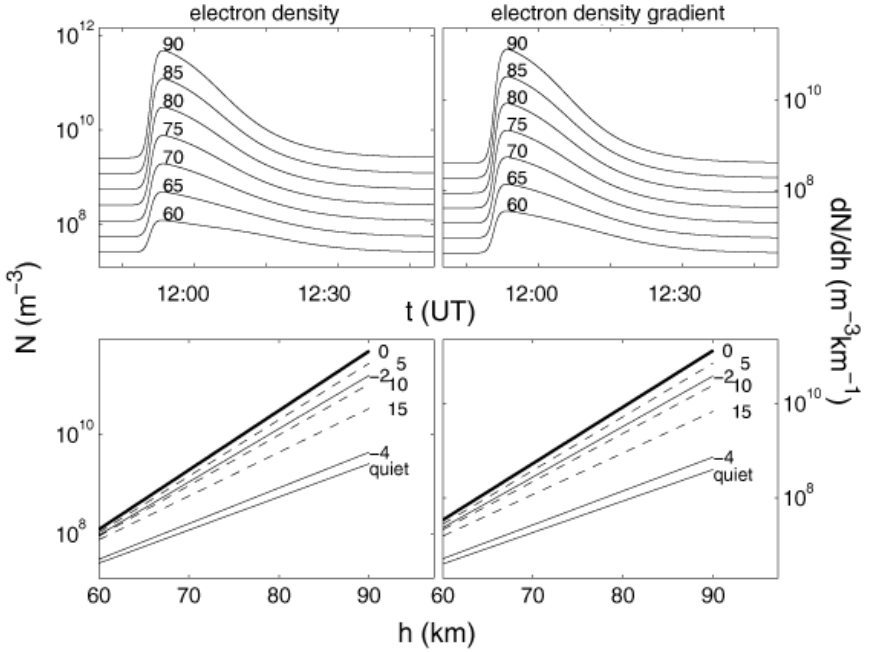


Figure 5. Time (upper panels) and altitude (bottom panels) dependencies of the electron density (left panels) and the electron density gradient (right panels). The considered altitudes for the time evolutions are given in km in upper panels. The altitude dependencies in the photoionization regime are presented by solid lines and labeled by negative minutes (minutes before the electron density maximum at 75 km) while those in the recombination regime (labeled by minutes after the electron density maximum) are shown as dash lines.

of recombination processes dominates in the electron loss rate). The first two terms describe the electron production while the third term relates to the electron loss processes which are represented by $G(\vec{r}, t)$ and $L(\vec{r}, t)$ in Eq. (11), respectively:

$$G(\vec{r}, t) = G_0(\vec{r}, t) + K(\vec{r}, t)I(t) \quad (13)$$

and

$$L(\vec{r}, t) = \alpha_{\text{eff}}(\vec{r}, t)N_e^2(\vec{r}, t). \quad (14)$$

In the cases of particular flare phases some additional approximations can be assumed:

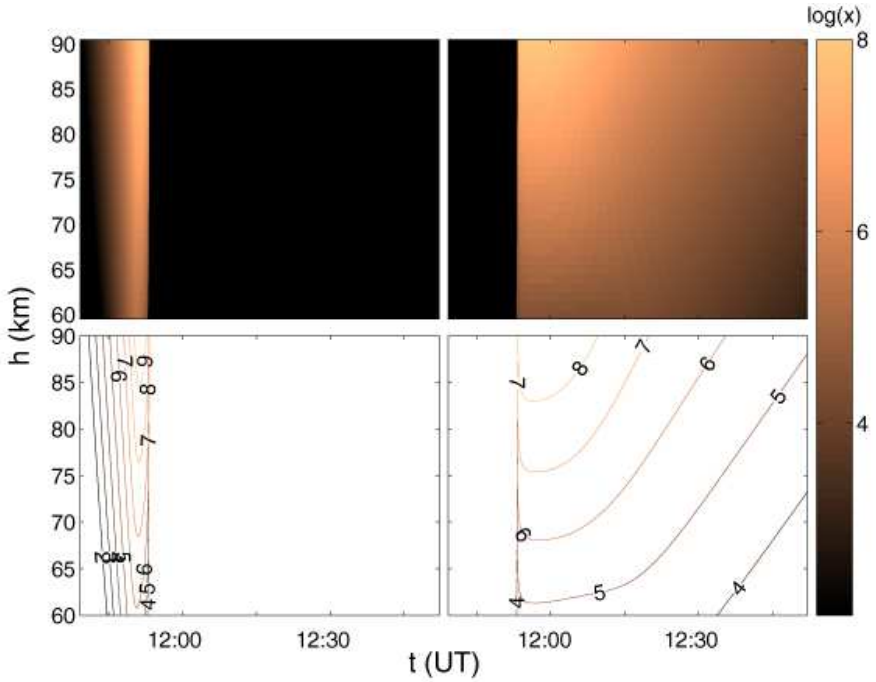


Figure 6. Surface (upper graphs) and contour (bottom graphs) plots of the electron density time derivative dN_e/dt normalized to its unit values $(dN_e/dt)^0 = 1 \text{ m}^{-3}\text{s}^{-1}$ during the photoionization (left panels) and recombination (right panels) regime, as a function of time t and altitude h during the considered solar X-ray flare. The plotted values x are calculated using equation $x = \log((dN_e/dt)^*(t, h)) = \log((dN_e/dt)/(dN_e/dt)^0(t, h))$.

- *Initial period.* In the unperturbed conditions the contribution of the X-radiation in the ionization process in the D-region is negligible ($G_0(\vec{r}, t) \gg K(\vec{r}, t)I(t)$). Because of that the intensity I must reach sufficiently large values so that the term $K(\vec{r}, t)I(t)$ has a measurable influence on electron production. Consequently, the start of recorded plasma perturbation has a delay with respect to the onset of the solar X-ray flare.
- *Period of the time evolutions maxima.* The time delay in the ionospheric response can be explained by assuming $\alpha_{\text{eff}}(\vec{r}, t)$, $G_0(\vec{r}, t)$ and $K(\vec{r}, t)$

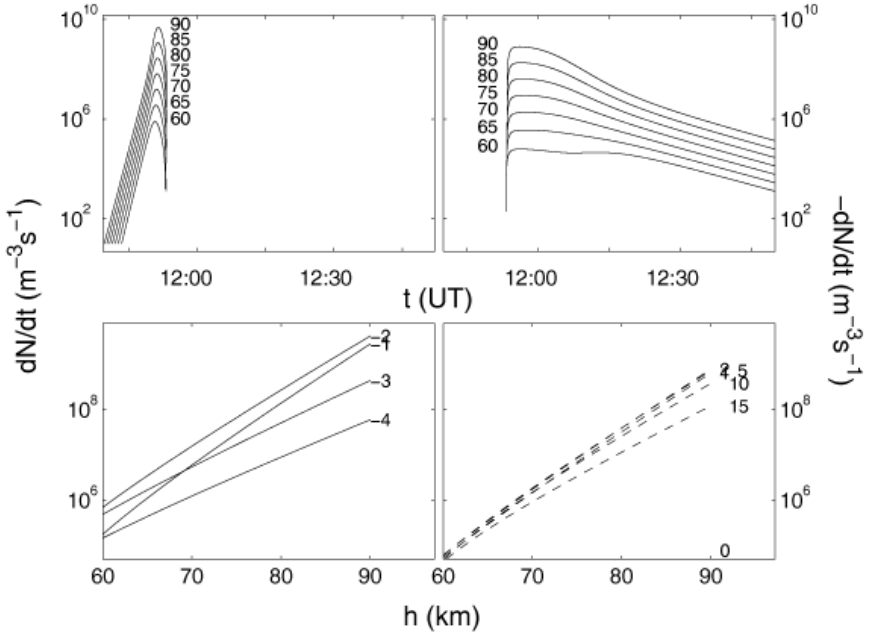


Figure 7. Time (upper panels) and altitude (bottom panels) dependencies of the electron density time derivative dN_e/dt during the photoionization (left panels) and recombination (right panels) regime. The considered altitudes for the time evolutions are given in km in upper panels. The altitude dependencies in the photoionization regime are presented by solid lines and noted by negative minutes (minutes before electron density maximum at 75 km) while those in recombination regime (noted by minutes after electron density maximum) are shown as dash lines.

approximately stationary in the time domain around the maximum of $N_e(t)$ ($dN_e(t)/dt = 0$). This yields the following relation:

$$K(\vec{r}, t) \frac{dI(t)}{dt} = \frac{dN_e^2(r, t)}{dt^2}. \quad (15)$$

From $dN_e^2/dt^2 < 0$ at the maximum of N_e , and $K > 0$ we conclude that $dI/dt < 0$ i.e. the X-radiation intensity decreases in time meaning that the maximum in I already occurred earlier. Physically speaking, the density takes time to respond to the increased flux and, as a result, their

peaks do not align with each other in time.

- *Time of ends of variations.* The electron density $N_e(t)$ does not respond instantaneously to variations of the X-radiation flux $I(t)$. In this sense, when $I(t)$ drops below the detection threshold value, the electron concentration N_e goes on decreasing due to dominant electron loss processes according to Eq. (11) with $K(\vec{r}, t)I(t) = 0$:

$$\frac{dN_e(r, t)}{dt} = G_0(\vec{r}, t) - \alpha_{\text{eff}}(\vec{r}, t)N_e^2(\vec{r}, t) \quad (16)$$

until the conditions of the unperturbed ionosphere are achieved. This occurs typically in less than one hour time (Žigman et al., 2007) after the influence of the solar flare becomes negligible.

The corresponding characteristics of the electron density gradient are shown in the rights panels of Figs 4 and 5. We can see that both the altitude and time distributions have practically the same shapes as in the case of the electron density. Keeping in mind that the propagation of the electromagnetic waves depends on the electron density, the deviation in the propagation path is more pronounced when electron density gradient is larger. Quantitatively, media can be described as the wave refraction at the border between two horizontal stratified media of thickness Δh with different indices of refractivity n_1 and n_2 using Snell's law:

$$\frac{\sin(\varphi_1)}{\sin(\varphi_2)} = \frac{n_2}{n_1}. \quad (17)$$

where φ_1 and φ_2 are the angles with respect to the vertical in the first and second medium, respectively. Assuming that the index of refractivity is:

$$n_i = \left[1 - \frac{79.21 \times N_e}{f^2} \right]^{1/2} \quad (18)$$

where N_e and f are taken in m^{-3} and Hz, respectively, Eq. (17) can be expressed as:

$$\frac{\sin(\varphi_1)}{\sin(\varphi_2)} = \left[\frac{79.21 \times \frac{\Delta N_e(h_1, h_2)}{\Delta h} \Delta h}{f^2 - 79.21 \times N_e(h_1)} \right]^{1/2}, \quad (19)$$

where $\Delta N_e(h_1, h_2) = N_e(h_1, h_2) - N_e(h_1)$ and $\Delta h = h_2 - h_1$. As we can see from the last expression, the increase of both the electron density and its

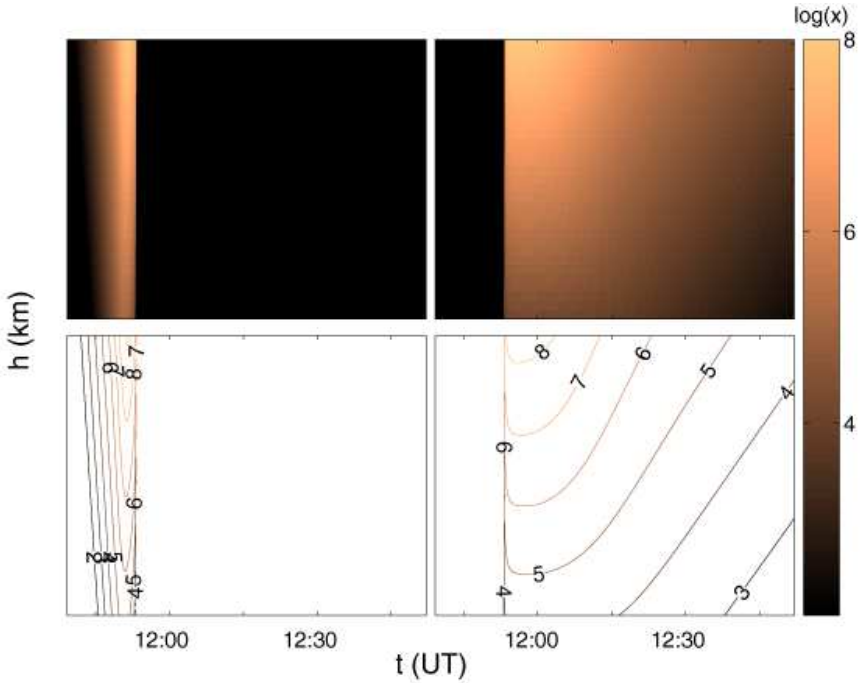


Figure 8. The same as in Fig. 6 but for time derivative of the electron density gradient. The plotted values x are calculated using equation $x = \log((d^2N_e/dhdt)^*(t, h)) = \log((d^2N_e/dhdt)/(d^2N_e/dhdt)^0(t, h))$ where $(d^2N_e/dhdt)^0 = 1 \text{ m}^{-3}\text{km}^{-1}\text{s}^{-1}$ is the unit value of time derivative of the electron density gradient.

gradient leads to a larger deviation in the propagation path of a fixed frequency signal. From the previous analysis we can conclude that the D-region plasma influence in the telecommunication technology is more important during large perturbation than in the quiet conditions especially at the top of this ionospheric medium.

4.3. Time and Altitude Distributions of Time Derivatives of Electron Density and Its Gradient

As we can see in Figs 4 and 5 the electron density and its gradient are not linearly dependent on altitude and time. For this reason their time derivatives

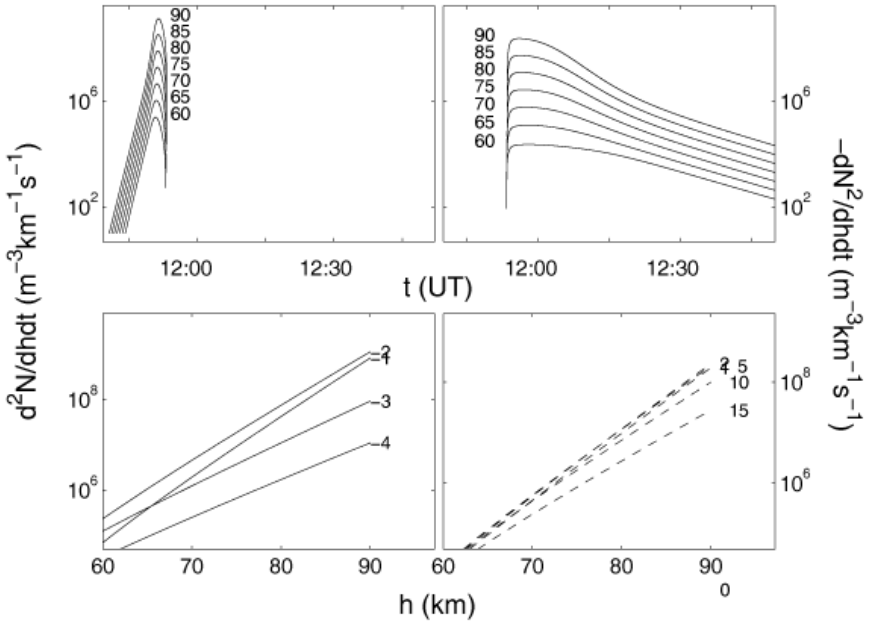


Figure 9. The same as in Fig. 6 but for time derivative of the electron density gradient $d^2 N_e/dhdt$.

are time dependent which is visualized in Figs 6-9 where we separately consider time derivatives of the electron density (the first two figures) and of its gradient (the second two figures). The positive and negative values are presented in the left and right panels, respectively.

The description of tendencies in the electron density time evolution given in Section 4.2 shows that the positive and negative sign of the time derivative dN_e/dt indicates the photoionization and recombination regime, respectively. In addition, although the times of the electron density maximum depends on altitude (this can be concluded from the time derivative of Eq. (7)) these differences are very small and can be negligible. Consequently, in both analyses the left and right panels represent the P and R regime, respectively.

As in the case of the previous analysis, the shapes of distributions of dN_e/dt and $d^2 N_e/dhdt$ are very similar which allows us to draw a common explanation.

The analyses of the considered dependencies and their comparisons in the P and R regime give the following conclusions:

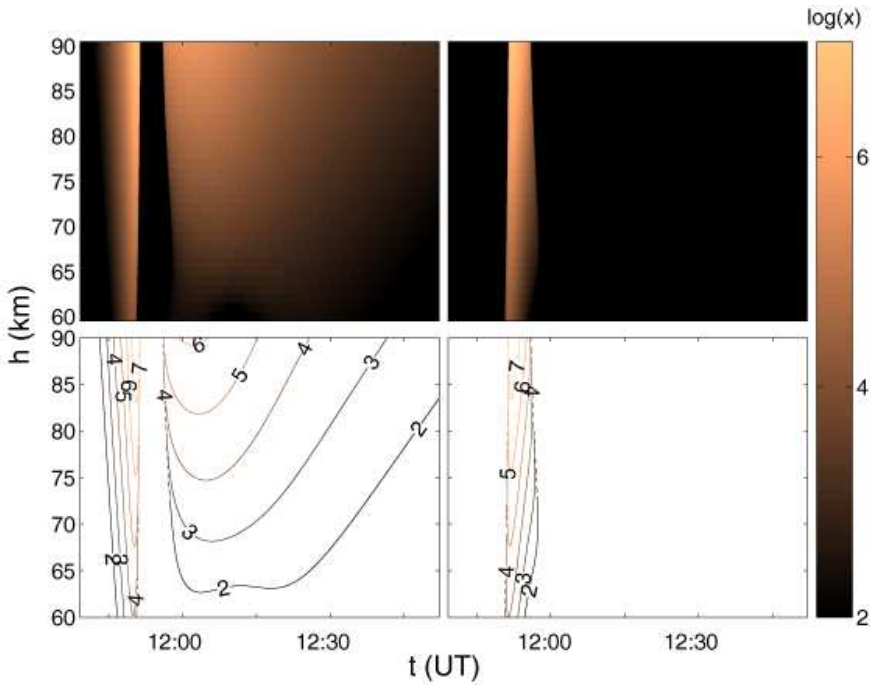


Figure 10. The same as in Fig. 6 but for the second time derivative of the electron density d^2N_e/dt^2 . The plotted values x are calculated using the relation $x = \log((d^2N_e/dt^2)^*(t, h)) = \log((d^2N_e/dt^2)/(d^2N_e/dt^2)^0(t, h))$ where $(d^2N_e/dt^2)^0 = 1 \text{ m}^{-3}\text{s}^{-2}$ is the unit value of the second time derivative of the electron density.

- The time variations of N_e and dN_e/dh are more pronounced in the P- than in the R-regime.
- Maxima of their time derivative are in the P-regime in the period before the electron density maximum.
- The considered values at fixed time t have exponential altitude dependencies and reach maxima at the top of the D-region. However, the slopes of corresponding lines presented in the bottom panels of Figs 7 and 9 are different. This is more visible in the P- than in the R-regime.

Physically speaking, the time variation in electron density characteristics

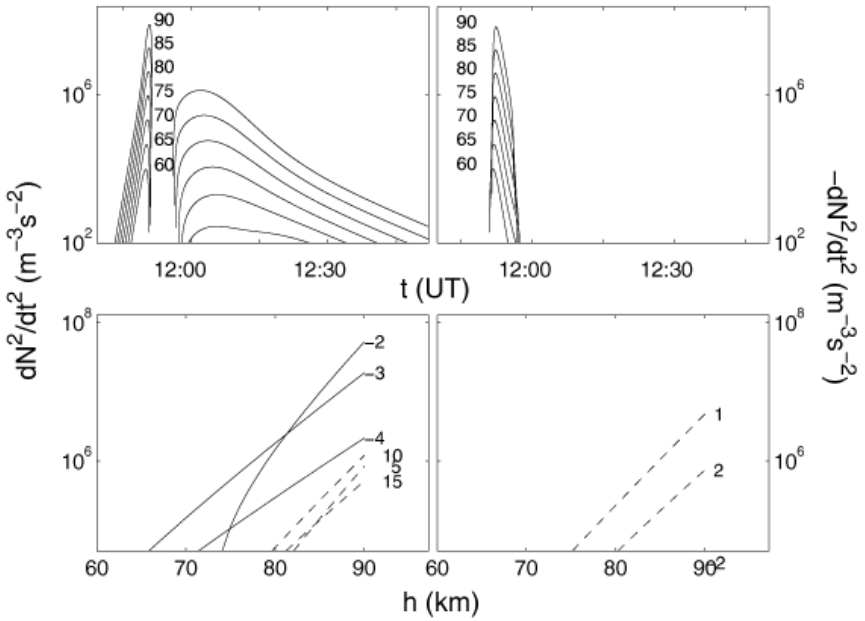


Figure 11. The same as in Fig. 6 but for the second time derivative of the electron density d^2N_e/dt^2 .

and, consequently, in signal propagation are the most intensive in the P-regime before the time when the electron density reaches its maximum.

4.4. Time and Altitude Distributions of the Second Time Derivative of the Electron Density and Its Gradient

Finally, in Figs (10)-(13) we present the time and altitude distributions of the second time derivative of the electron density and its gradient which values are especially significant in the period of the X-radiation maximum (see Eq.(15)). Contrary to the first time derivative there are several properties that indicate a more complex analysis of variations in this case:

- The positive and negative values are present in both the P- and R-regime.
- The decrease in time variations of N_e and dN_e/dh is obtained at the end of the P-regime and in the beginning of the R-regime.

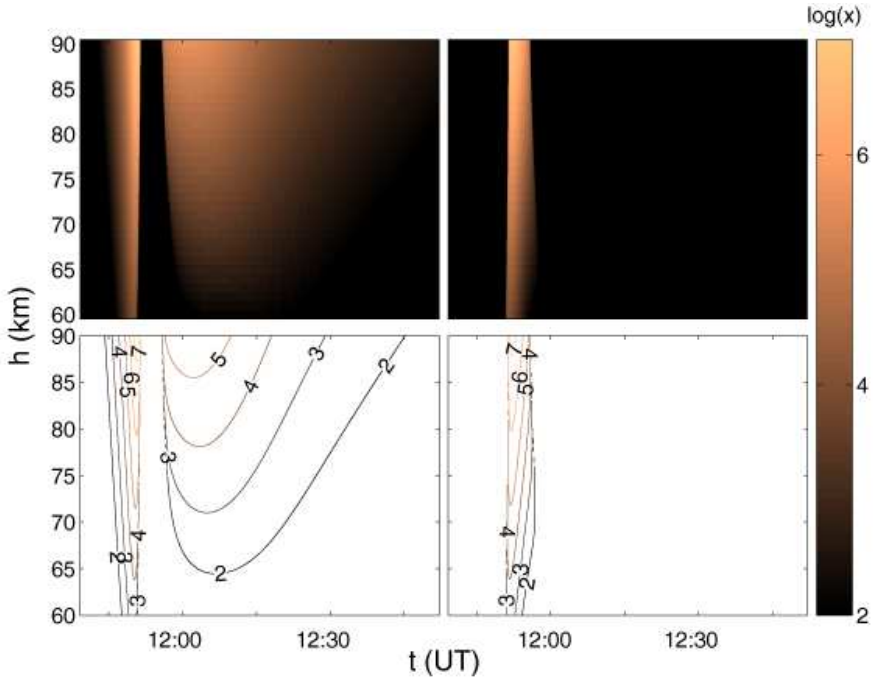


Figure 12. The same as in Fig. 6 but for the second time derivative of the electron density gradient $d^3N_e/dhdt^2$. The plotted values x are calculated using equation $x = \log((d^3N_e/dhdt^2)^*(t, h)) = \log((d^3N_e/dhdt^2)/(d^3N_e/dhdt^2)^0(t, h))$ where $(d^3N_e/dhdt^2)^0 = 1 \text{ m}^{-3}\text{km}^{-1}\text{s}^{-2}$ is the unit value of the second time derivative of the electron density.

- The times when the considered second derivatives change sign are altitude dependent especially in the R-regime.

As in previous analyses the corresponding panels for the electron density and its gradient second time derivatives are very similar.

Conclusion

Motivated by a very significant role that electrons have in various physical and chemical processes in the ionosphere as well as its influence on electromagnetic

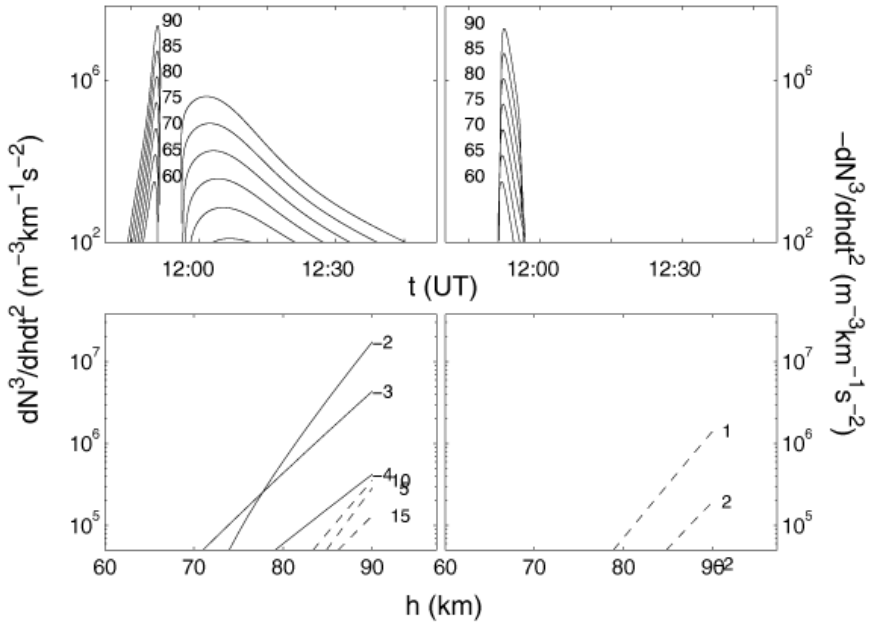


Figure 13. The same as in Fig. 6 but for the second time derivative of the electron density gradient $d^3N_e/dhdt^2$.

wave propagation and, consequently, in telecommunications, we present in this paper a study on variations in the electron density under the influence of solar X-ray flares as one of the most important source of ionospheric disturbances. As this astrophysical phenomenon induces the largest relative perturbations in the lowest ionosphere our attention is focused on the D-region. The diagnostic is made by the technique based on the VLF/LF radio signal propagations.

Here we present the modeling of the electron density distribution in space and time and apply the procedure that includes experimental observations, numerical simulations, and theoretical analyses to the D-region monitored by the 23.4 kHz VLF signal emitted in Germany and received in Serbia during the influence of the solar X-ray flare recorded by the GOES-14 satellite on May 5, 2010.

The main presented characteristics of the D-region electron density during the considered time period can be summarized by the following conclusions:

- The electron density can significantly increase during solar X-ray flares

(more than by one order of magnitude).

- The electron density time evolution is similar to that of the X-radiation intensity but specific times related to the start and end of the variation as well as the time of the electron density maximum follow the corresponding times related to the X-radiation time variation.
- The electron density changes are a consequence of variations in the electron gain and loss processes. Keeping in mind that photoionization and recombination are the most important processes in the D-region, and that the domination of one of them influences the increase and decrease in the electron density that can be represented as the photoionization (P) and recombination (R) regime, respectively.
- The R regime lasts longer than the P regime.
- The changes in the electron density time variations are represented by its time derivative which is larger in the P-regime its the maximum occurs before the electron density maximum.
- The second time derivative has both the positive and negative values in the two regimes.
- The intensity of the considered changes in local electron density and, in resulting, variations of the medium influence on telecommunication signals, increases with altitude.
- The qualitative properties of the vertical gradient of electron density are practically the same as those of the electron density.

In this study we show that influence of not too intensive solar X-ray flares can be important in the D-region plasma which indicates the importance of investigation of the space weather influence on the ionosphere from scientific (especially in geophysics and astrophysics) point of view, as well as concerning its practical applications of the described analysis in telecommunications.

Acknowledgments

A. N. acknowledges support of the Ministry of Education, Science and Technological Development of the Republic of Serbia through the projects III 44002

and 176002. The author is also grateful to Vladimir M. Čadež for very useful suggestions and comments. The data for this paper collected by GOES-14 satellite is available at NOAA's National Centers for Environmental information (http://satdat.ngdc.noaa.gov/sem/goes/data/new_full/2010/05/goes14/csv/g14_xrs_2s_20100505_20100505.csv). Requests for the VLF data used for analysis can be directed to the author.

References

- Astafyeva, E. I. and Afraimovich, E. L. (2006). Long-distance traveling ionospheric disturbances caused by the great Sumatra-Andaman earthquake on 26 December 2004. *Earth Planets Space*, 58:1025–1031.
- Bajčetić J., Nina A., Čadež, V. M. and Todorović B. M. (2015). Ionospheric D-region temperature relaxation and its influences on radio signal propagation after solar X-flares occurrence. *Therm. Sci.*, 19, Suppl. 2:S299-S309.
- Blaunstein, N. and Christodoulou, C. (2006). *Radio Propagation and Adaptive Antennas for Wireless Communication Links: Terrestrial, Atmospheric and Ionospheric*, Wiley, USA.
- Chau, J. L., Rottger, J., and Rapp, M. (2014). PMSE strength during enhanced D region electron densities: Faraday rotation and absorption effects at VHF frequencies. *J. Atmos. and Sol.-Terr. Phy.*, 118, Part A(0):113 – 118.
- Clilverd, M. A., Rodger, C. J., Thomson, N. R., Brundell, J. B., Ulich, T., Lichtenberger, J., Cobbett, N., Collier, A. B., Menk, F. W., Seppälä, A., Verronen, P. T., and Turunen, E. (2009). Remote sensing space weather events: Antarctic-Arctic Radiation-belt (Dynamic) Deposition-VLF Atmospheric Research Konsortium network. *Space Weather*, 7:4001.
- Cohen, M. B., Inan, U. S., and Paschal, E. W. (2010). Sensitive Broadband ELF/VLF Radio Reception With the AWESOME Instrument. *IEEE T. Geosci. Remote*, 48:3–17.
- Dautermann, T., Calais, E., Lognonné, P., and Mattioli, G. S. (2009). Lithosphere-atmosphere-ionosphere coupling after the 2003 explosive eruption of the Soufriere Hills Volcano, Montserrat. *Geophy. J. Int.*, 179:1537–1546.

- Drobzheva, Y. V. and Krasnov, V. M. (2003). The acoustic field in the atmosphere and ionosphere caused by a point explosion on the ground. *J. Atmos. and Sol.-Terr. Phys.*, 65:369–377.
- Ferguson, J. A. (1998). *Computer Programs for Assessment of Long-Wavelength Radio Communications, Version 2.0, Space and Naval Warfare Systems Center, San Diego.*
- Friedrich, M. and Torkar, K. M. (2001). FIRI: A semiempirical model of the lower ionosphere. *J. Geophys. Res.*, 106:21409–21418.
- Grubor, D. P., Šulić, D. M., and Žigman, V. (2008). Classification of X-ray solar flares regarding their effects on the lower ionosphere electron density profile. *Ann. Geophys.*, 26:1731–1740.
- Han, F., Cummer, S. A., Li, J., and Lu, G. (2011). Daytime ionospheric D region sharpness derived from VLF radio atmospheric. *J. Geophys. Res.-Space*, 116:5314.
- Inan, U. S., Cummer, S. A., and Marshall, R. A. (2010). A survey of ELF and VLF research on lightning-ionosphere interactions and causative discharges. *J. Geophys. Res.-Space*, 115:0.
- Inan, U. S., Lehtinen, N. G., Moore, R. C., Hurley, K., Boggs, S., Smith, D. M., and Fishman, G. J. (2007). Massive disturbance of the daytime lower ionosphere by the giant γ -ray flare from magnetar SGR 1806-20. *Geophys. Res. Lett.*, 34:8103.
- Kintner, P. M. and Ledvina, B. M. (2005). The ionosphere, radio navigation, and global navigation satellite systems. *Adv. Space Res.*, 35(5):788 – 811.
- Kiryushkin, V. V., Afraimovich, E. L., and Disenov, A. A. (2008). GPS monitoring of ionospheric disturbances generated during rocket launches at large distances from launch sites. *Geomagn. Aeron.*, 48:352–366.
- Kolarski, A., Grubor, D., and Šulić, D. (2011). Diagnostics of the Solar X-Flare Impact on Lower Ionosphere through Seasons Based on VLF-NAA Signal Recordings. *Balt. Astron.*, 20:591–595.

- McRae, W. M. and Thomson, N. R. (2000). VLF phase and amplitude: daytime ionospheric parameters. *J. Atmos. and Sol.-Terr. Phys.*, 62:609–618.
- Nina, A., Čadež, V., Srećković, V. A., and Šulić, D. (2011). The Influence of Solar Spectral Lines on Electron Concentration in Terrestrial Ionosphere. *Baltic Astronomy*, 20:609–612.
- Nina, A., Čadež, V., Srećković, V., and Šulić, D. (2012a). Altitude distribution of electron concentration in ionospheric D-region in presence of time-varying solar radiation flux. *Nucl. Instrum. Methods in Phys. Res. B*, 279:110–113.
- Nina, A., Čadež, V., Šulić, D., Srećković, V., and Žigman, V. (2012b). Effective electron recombination coefficient in ionospheric D-region during the relaxation regime after solar flare from February 18, 2011. *Nucl. Instrum. Methods in Phys. Res. B*, 279:106–109.
- Nina, A. and Čadež, V. M. (2013). Detection of acoustic-gravity waves in lower ionosphere by vlf radio waves. *Geophys. Res. Lett.*, 40(18):4803–4807.
- Nina, A. and Čadež V.M. (2014). Electron production by solar Ly- α line radiation in the ionospheric D-region. *Adv. Space Res.*, 54(7):1276–1284.
- Nina, A., Simić, S., Srećković, V. A. and Popović, L. Č. (2015a). Detection of short-term response of the low ionosphere on gamma ray bursts. *Geophys. Res. Lett.*, 42:8250–8261.
- Nina, A., Čadež, V. M. and Bajčetić, J. (2015b). Contribution of solar hydrogen Ly α line emission in total ionization rate in ionospheric D-region during the maximum of solar X-flare *Serb. Astron. J.*, 191:51–55.
- Peter, W. B. and Inan, U. S. (2005). Electron precipitation events driven by lightning in hurricanes. *J. Geophys. Res.-Space*, 110:5305.
- Raulin, J.-P., Correia de Matos David, P., Hadano, R., Saraiva, A. C. V., Correia, E., and Kaufmann, P. (2009). The South America VLF NETwork (SAVNET). *Earth Moon and Planets*, 104:247–261.
- Reinisch, B. W., Haines, D. M., Bibl, K., Galkin, I., Huang, X., Kitrosser, D. F., Sales, G. S., and Scali, J. L. (1997). Ionospheric sounding in support of over-the-horizon radar. *Radio Sci.*, 32(4):1681–1694.

- Rozhnoi, A., Shalimov, S., Solovieva, M., Levin, B., Hayakawa, M., and Walker, S. (2012). Tsunami-induced phase and amplitude perturbations of subionospheric VLF signals. *J. Geophys. Res.-Space*, 117:9313.
- Singh, A. K., Singh, A., Singh, R., and Singh, R. (2014). Solar flare induced d-region ionospheric perturbations evaluated from vlf measurements. *Astrophys. Space Sci.*, 350(1):1–9.
- Strelnikova, I. and Rapp, M. (2010). Studies of polar mesosphere summer echoes with the EISCAT VHF and UHF radars: Information contained in the spectral shape. *Adv. Space Res.*, 45:247–259.
- Thomson, N. R. (1993). Experimental daytime VLF ionospheric parameters. *J. Atmos. and Sol.-Terr. Phy.*, 55:173–184.
- Todorović Drakul M., Čadež, V. M., Bajčetić J., Blagojević. D., and Nina, A. Behaviour of electron content in the ionospheric D-region during solar X-ray flares. *Serb. Astron. J.*, accepted paper.
- Turunen, E., Tolvanen, J., H., M., and Ranta, H. (1992). *D Region Ion Chemistry Model* In: Schunk, R.W. (Ed.), STEP Handbook of Ionospheric Models. Boulder, Colorado, USA.
- Žigman, V., Grubor, D., and Šulić, D. (2007). D-region electron density evaluated from VLF amplitude time delay during X-ray solar flares. *J. Atmos. and Sol.-Terr. Phy.*, 69:775–792.
- Šindelářová, T., Burešová, D., and Chum, J. (2009). Observations of acoustic-gravity waves in the ionosphere generated by severe tropospheric weather. *Stud. Geophys. Geod.*, 53:403–418.
- Wait, J. R. and Spies, K. P. (1964). *Characteristics of the Earth-ionosphere waveguide for VLF radio waves*, NBS Technical Note 300, National Bureau of Standards, Boulder, CO.
- William, s. and Foley, C. I. (1978). *Steady-state Multi-ion Disturbed D-region Model*, Hanscom AFB, Mass.: Aeronomy Division, Air Force Geophysics Laboratory, USA.

-
- Xiong, B., Wan, W., Liu, L., Withers, P., Zhao, B., Ning, B., Wei, Y., Le, H., Ren, Z., Chen, Y., He, M., and Liu, J. (2011). Ionospheric response to the x-class solar flare on 7 september 2005. *J. Geophys. Res.-Space*, 116(A11):A11317.
- Yang, Y.-M., Garrison, J. L., and Lee, S.-C. (2012). Ionospheric disturbances observed coincident with the 2006 and 2009 North Korean underground nuclear tests. *Geophys. Res. Lett.*, 39:2103.

Complimentary Contributor Copy

Chapter 3

**ANALYSIS OF THE IONOSPHERIC D-REGION
DISTURBANCES IN RESPONSE TO THE
EFFECTS OF SOLAR X-RAY FLARES**

Desanka M. Šulić^{1,}, Vladimir A. Srećković^{2,†}
and Anatolij A. Mihajlov^{2,‡}*

¹University Union - Nikola Tesla, Belgrade, Serbia

²University of Belgrade, Institute of Physics, Pregrevica, Belgrade, Serbia

ABSTRACT

The sensitivity of Very Low Frequency (VLF, 3-30 kHz) and Low Frequency (LF, 30-300 kHz) propagation in the lower ionosphere makes it an ideal probe for remotely sensing the ambient state and localized perturbations of the lower ionosphere. During occurrence of solar X-ray flare the altitude distribution of the ionospheric electron density is a noticeable and interesting issue and known as Sudden Ionospheric Disturbance (SID). This is an important classical topic event for solar-terrestrial relations. The induced SID in the D-region causes perturbations in the received amplitude and phase on VLF/LF radio signals. The basis of this work is amplitude and phase data acquired by monitoring NAA/24.00 kHz, GQD/22.10 kHz, DHO/23.40 kHz, ICV/20.27 kHz and NSC/45.90 kHz, radio signals at Belgrade site (44.85° N, 20.38° E) Serbia

* E-mail: desankasulic@gmail.com.

† E-mail: vlada@ipb.ac.rs.

‡ E-mail: mihajlov@ipb.ac.rs.

by AbsPAL and AWESOME receivers since 2003 and 2008 up to 2015, respectively. We expected and estimated differences in amplitude and phase perturbations on VLF/LF radio signals induced by solar X-ray flares which occurrences are under different solar zenith angles over illuminated propagation paths.

Observed VLF perturbations at Belgrade site have sensitive dependence on: *X-ray flare intensity, solar zenith angle, solar flare duration and geophysical characteristics of VLF/LF path*. The model computations applied to the multiple path observations at Belgrade site are able to reproduce a number of the general features of the electron density enhancement induced by occurrence of solar X-ray flares during the period of the ascending phase and the maximum of the Solar Cycle 24.

1. INTRODUCTION

The Earth's atmosphere processes are dependent on the wavelength of solar radiation. The very short wavelengths like X-rays and ultraviolet are completely absorbed by the atmosphere resulting in photoionization and photo dissociation and are responsible for establishment of the ionosphere at heights above ~ 60 km. Also, the longer wavelengths (the visible and infrared light) although partially absorbed by the atmosphere, manage to reach the Earth surface influencing the Earth's climate (Leckner 1978; Bird & Riordan 1986). The observation of solar radiation, and its influence on Earth's ionosphere, especially by the explosive events like solar flares, becomes a requirement and important thing nowadays.

As it is known the ionosphere is the part of the atmosphere that contains ionized gases. The degree of ionization depends on the incident radiation. The primary process is photoionization of thermospheric gases by the Sun's extreme ultraviolet and X-ray radiations. Both these radiations are approximately hundred times stronger at the solar maximum than at solar minimum. Secondary processes include ionization by photoelectrons and scattered or reemitted radiation. The ionosphere, at all latitudes, has a tendency to separate in different regions, despite of the fact that different processes dominate in different latitudinal domains. These regions named D, E, and F are distinct only in the daytime ionosphere at middle latitudes. The different regions are generally characterized by a density maximum at a certain altitude, and density decreases with altitudes on both sides of the maximum. Methods of researching ionosphere are numerous. Depending on the ionospheric

composition, preferred techniques and mainly its height (altitude) for investigation are used *rockets, satellites, balloons, digisonde, GPS, different ground based measurements like radars, VLF/LF radio measurements, optical instruments*, and etc. (see e.g., Hargreaves 1992; Prolss 2004). For instance, at ionospheric F-region (150–800 km), it is possible to perform direct satellites and probes measurements. The part of the ionosphere below ~90 km requires special methods for its study, and special theories for its explanation, it is called the D-region.

The parts of the spectrum that penetrate to the D-region have wavelengths less than about 1 nm (X radiation) or greater than 102.7 nm. During quiet solar conditions the D-region is formed primarily by the action of solar Lyman-alpha radiation (121.6 nm) on nitric oxide. Daytime electron density in this region is about or less than $N_e \sim 10^8\text{-}10^9 \text{ m}^{-3}$. During the nighttime the ionization rate drops and recombination processes continue duration. Even at night there is a sufficient ionization in the lowest region of ionosphere to affect VLF/LF radio signals. A range of dynamic phenomena occur in the D-region and cause diurnal and seasonal variations in connection with solar activity (Goodman 2005a, b).

VLF and LF bands are below the critical frequencies of the D-region. Most of the energy radiated by the VLF/LF transmitters is trapped between the ground and the D-region, forming the Earth-ionosphere waveguide. Subionospheric VLF/LF signals reflect from the D-region of the ionosphere (during daytime ~70-75 km and during nighttime ~90 km). This propagation is stable both in amplitude and phase and has relatively low attenuation. VLF/LF radio signals propagate over Earth trapped between the imperfect mirrors of the ground and the ionosphere. The effective reflection height depends on the ionization levels of the D-region. The only possible method of probing the D-region is VLF/LF subionospheric radio signals (Budden 1961; Wait 1962; Mitra 1974; Inan et al., 1985; Barr et al., 2000; Thomson et al., 2011).

Any variations on the ionospheric D/E-region lead to changes in the propagation conditions for VLF/LF radio signals propagating subionosphericly, and hence changes in the observed amplitude and phase of VLF/LF transmissions are due to different kinds of perturbation sources:(1) solar flares, (2) geomagnetic storms (and the corresponding particle precipitation), (3) the direct effect of lightning and (4) effect of earthquakes (or seismic activity) on to the lower ionosphere (see e.g., Mitra 1974; Carpenter et al., 1984; Bar et al., 2000; Hayakawa 2000, Bothmer & Daglis 2007; Prölss 2004; Thomson et al., 2005).

The phenomenon such as solar X-ray flare illuminating the daytime ionosphere induces unpredictable effects that are associated with space weather. When the solar X-ray flares appear, the X-ray fluxes suddenly increase and the ones with the appreciable wavelength below 1 nm are able to penetrate down to the D-region and increase the ionization rate there (see Mitra 1973; Thomson 2001, 2014 and reference therein).

The purpose of this paper is to study effects of illuminating D-region with *sudden, rapid, and intense variation in X-ray flux* and consequences of this event to propagation characteristics of amplitude and phase on VLF/LF radio signals (SID VLF/LF signatures).

2. METHOD OF ACQUIRENT DATA FOR ANALYSIS SID VLF SIGNATURES

2.1. Observations at VLF and LF Frequencies

All the data were recorded at a Belgrade site by two receiver systems: Absolute Phase and Amplitude Logger (Abs PAL) system and Atmospheric Weather Electromagnetic System for Observation Modeling and Education (AWESOME).

In 2003 the Abs PAL system was installed and brought to stable operation. The Abs PAL Belgrade VLF station has been developed by the Radio and Space Physics Group of Otago University, New Zealand (for details see Zigman et al., 2007). The receiver has been in stable operation since 2003, providing simultaneous data (amplitude in dB above $1\mu\text{V}/\text{m}$, and phase in deg). The Abs PAL was used for receiving, monitoring and for the storage of amplitude and phase delay of VLF data in the regular diurnal and seasonal behavior of the lower ionosphere and also for tracking the signature of solar flares. The Abs PAL VLF receiver can log up to six transmitters at a time, logging phase and amplitude with time resolutions ranging from 50 ms to 60 s.

The second VLF/LF receiver-AWESOME facility is developed by the Stanford University, Stanford USA. The receiver has been in stable operation since 2008, continuously collecting data and providing simultaneous VLF amplitude and phase from worldwide transmitters. The system consists of two loop magnetic antennas, GPS, preamplifier, cables, and equipment connected to the PC (AD card). The software is based on *python* and *mat lab*, which is especially developed for this use by the Stanford University VLF group.

Recorded data are generally saved in two different resolutions - high resolution (50 Hz) and low resolution (1 Hz). Narrowband data can be recorded in a continuous fashion, even in case when as many as 15 transmitters are being monitored (Cohen et al., 2010).

In this chapter we confine our attention to the analysis of amplitude and phase data acquired by monitoring VLF radio signals emitted by five transmitters during a seven-year period (2008-2014). This period covers the ascending phase and the maximum of the Solar Cycle 24. All the data were recorded at a Belgrade site by two receiver systems.

The five transmitter signals in this work are listed in Table 1. Each of these transmitters operates continuously (with the exception of maintenance down time, typically less than several hours per week) and normally transmit data at a bit rate of $R_b = 220$ bits/s using minimum-shift keying (MSK) modulation.



Figure 1. Great Circle Paths (GCPs) of subionospherically propagating VLF radio signals recorded at Belgrade site.

VLF radio signals received at Belgrade site include: NAA/24.00 kHz, GQD/22.10 kHz, DHO/23.40 kHz, ICV/20.27 kHz and NSC/45.90 kHz. The transmitter of NAA/24.00 kHz is located in Maine USA (in Time zone UTC - 5.00). The NAA/24.00 kHz propagates in the Earth-ionosphere waveguide over Atlantic Ocean and Central Europe. The distance of NAA-BEL path is 6540 km and it belongs to the group of *long paths*. The transmitter of GQD/22.10 kHz is located in the UK, but a radio signal propagates over great

segment of path in the same time zone where the receiver is. The distance of GQD-BEL path is 1980 km. The three European transmitters of DHO/23.40 kHz, ICV/20.27 kHz and NSC/45.90 kHz radio signal are located in the same time zone (Time zone UTC +1.00) as a receiver site. The distances of these three paths are in the range $956 < D < 1300$ km. Locations of these five transmitters and receivers are shown in Figure 1.

The details of the VLF transmitting and receiving sites and the path geometries are provided in Table 1 and Table 2.

2.2. Acquired Data of X-Ray Flux

The analysis and comparison of VLF data has been carried out together with the examination of the corresponding solar X-ray fluxes.

Table 1. Main characteristics of VLF/LF transmitters

Transmitter	Frequency (kHz)	Site	Geographic coordinates (deg)	GCP (km)	Orientation of propagation path
NAA	24.00	Main, USA	44.63 ⁰ N, 67.28 ⁰ E	6540	west to east
GQD	22.10	Skelton, UK	54.73 ⁰ N, 2.880 W	1980	northwest to southeast
DHO	23.40	Rhauderhent, Germany	53.08 ⁰ N, 7.61 ⁰ E	1300	northwest to east
ICV	20.27	Isola di Tavolara, Italy	40.92 ⁰ N, 9.730 E	976	southwest to northeast
NSC	45.90	Sicily, Italy	38.00 ⁰ N, 13.50 ⁰ E	956	southwest to northeast

Table 2. Main characteristics of VLF/LF receiving systems

Receiver	Class	Start year	Site	Geographic coordinates (deg)
AbsPAL	Electric antenna	2003	Belgrade, Serbia	44.85 ⁰ N, 20.38 ⁰ E
AWESOME	Loop magnetic antenna	2008	Belgrade, Serbia	44.85 ⁰ N, 20.38 ⁰ E

Table 3. X-ray peak flux intensities in band 0.1-0.8 nm for different classes of solar flares

Class	Peak flux intensities (W/m^2)
A	$I_x < 10^{-7}$
B	$10^{-7} \leq I_x < 10^{-6}$
C	$10^{-6} \leq I_x < 10^{-5}$
M	$10^{-5} \leq I_x < 10^{-4}$
X	$10^{-4} \leq I_x$

The intensity of solar X-ray flux is recorded by the GOES satellites (Geostationary Operational Environmental Satellite). The GOES satellites records the X-ray fluxes in two wavelength bands: 0.1-0.8 nm, referred to as “long” or “XL” and 0.05-0.4 nm, referred to as “short” or “XS” (Menzel & Purdom 1994; Hillger & Schmit 2007, 2009, 2011).

The main important data in our work are data of intensity of X-ray flux in the band 0.1-0.8 nm. The satellite data are available from National Oceanic and Atmospheric Administration USA, via the web site: www.swpc.noaa.gov/ftpmenu/lists/xray.html.

Scientists classify solar flares in A, B, C, M, and X classes according to the peak flux in W/m^2 of 0.1-0.8 nm X-rays near Earth. Each category for X-ray flares is also partitioned the different levels and has subdivisions ranging from 1.0 to 9.9, e.g., C1.0 to C9.9, M1.0 to M9.0, and X1.0 to X9.9 (Hillger & Schmit 2011).

The A class and B class solar flares are too weak to make noticeably affect on propagation of VLF/LF radio signals but C class induced changes of amplitude and phase on VLF/LF radio signals. The M class solar flares induce significant disturbances on VLF/LF propagation and beside this can cause some damages (short radio blackouts and minor radiation storms). And then the X class solar flares are more powerful and have the most significant effects on Earth ionosphere (Goodman 2005; Jakowski et al., 2008).

3. PHYSICAL PROPERTIES OF THE D-REGION

The high atmosphere provides a low pressure laboratory without walls where the reactions occur between electrons, ions and neutral particles. The ionosphere is part of the Earth atmosphere which is mostly ionized by the solar

radiation. This region of electroneutral plasma is located in the terrestrial atmosphere at altitudes between around fifty kilometers and several hundreds of kilometers above the Earth's surface. In the ionosphere the presence of charged particles plays a significant role in the propagation of radio waves.

The D-region is located approximately at altitudes ~60-90 km above the Earth's surface. Solar electromagnetic waves propagating below 85 km in the atmosphere are: X-rays of wavelength <1 nm; Lyman-alpha; and wavelengths greater than 180 nm. These radiations can induce ionization of molecular nitrogen and oxygen; nitric oxide; and various atoms such as sodium and calcium. Molecular oxygen and nitrogen are also ionized by cosmic rays. It is possible to explain normal conditions of ionization by cosmic rays and Lyman-alpha. Above 85 km, the behavior of the ionization is related to the formation of the *E-region*. The electron density in the D-region is usually about $\sim 10^8$ - 10^9 electron/m³.

During nighttime condition in the D-region occur suddenly changes of electron density altitude profile. The electron density in the D-region drops as a consequence of disappearing solar radiation. Namely, recombination processes overcome the ionization process causing the movement of reflection height at about 90 km, which is at the bottom of the nighttime E-region (Retcliffe 1972; Mitra 1972; Woods et al., 2009; Prolss 2004; Kelley 2009).

The production of electrons in the D-region is a consequence of space weather conditions. The enhanced X-ray radiation during a solar flare leads to an increased rate of production electrons. The largest difference between quiet and active solar conditions occurs at altitudes between 65 and 75 km. Although the D-region ionization is low compared to the E and F-regions, it does have a huge effect on propagation of radio waves. SIDs, are studied in many scientific institutions and also in our VLF/LF Laboratory, Institute of Physics, Belgrade University, Belgrade.

3.1. Model of Ambient and Disturbed D-Region

In this work, we primarily consider ionospheric disturbances which occur during daytime. We restrict our attention to the study of effects of sudden increase in X-ray irradiance on the lowest altitudes of the ionosphere, specifically the altitude below ~ 70 km in the D-region. A two-parameter analytical expression for the altitude dependence of the D-region electron density was given by Wait and Spies (1964) as:

$$N_e(h, H') = 1.43 \cdot 10^{13} \exp(-0.15 \cdot H') \exp[(\beta - 0,15) \cdot (h - H')] \quad \text{m}^{-3}$$

Eq. (1)

where N_e is electron density in electrons/m³, h is the height in km and β and H' are model parameters having units of km⁻¹ and km, respectively. The parameter β (km⁻¹) describes the “sharpness” of the profile. The parameter H' (km) was shown to be a good representation of the approximate height at which VLF reflections occur. The Wait and Spies (1964) model has been successfully used in previous comparisons of VLF measurements and theory (e.g., Mitra 1972; Thomson 1993; Cummer et al., 1998; McRae and Thomson 2000) and we also use it in our work.

For propagation of radio waves below the F-region, the effective electron-neutral collision frequency profile, largely determined by the relatively stable neutral density, is important in addition to electron density. In all cases, the exponential altitude profile of collision frequency is given by:

$$\nu(h) = 1.82 \cdot 10^{11} \exp(-0.15 \cdot h)$$

Eq. (2)

where ν is in s⁻¹ and h in km (Wait and Spies, 1964).

This model has been used to simulate altitude electron density profile in the D-region at regular conditions (Thomson, 1993; McRae and Thomson, 2000), as well as for the perturbed conditions by solar flares (McRae and Thomson 2004; Thomson et al., 2005, Nina et al., 2011, 2012a, b).

3.2. Method of Simulations Propagation of VLF/LF Radio Signals

The radio waves in VLF and LF bands propagate from transmitters through a waveguide bounded by the Earth's surface (ground or sea) and the D-region. The Earth-ionosphere waveguide propagation theory developed by Budden (1962) takes into account: *the Earth's curvature, geomagnetic field, altitude profiles of electron-neutral collision frequency and electron density* and serves as the basis for the numerical modeling codes. A two-dimensional model was developed at the Naval Research and Development Laboratory (Ferguson et al., 1989 and references therein).

This model, known as the Long Wave Propagation Capability (LWPC) code, is software package of several separate programs, and each of them is designed for execution of specific tasks. The LWPC software package takes as the input path variables: *frequency, transmitter and receiver coordinates, and the orientation of the transmitting and receiving antenna and the boundaries of the operating area*. The program automatically selects paths along geographic bearing angles to ensure that the operating area is fully covered. The diurnal conditions and other relevant parameters are then determined along each path. After the mode parameters along each path are determined, the signal strength along each path is computed.

In this chapter, we used a few step process to estimate the perturbed VLF signal amplitude and phase during a solar flare. Simultaneous observations of amplitude $A_{disturbed}$ and phase $\phi_{disturbed}$ on VLF radio signals during solar X-ray flares could be applied for calculations of electron density profile and ionization rates and effective electron recombination coefficients in the D-region using this method:

1. Using the LWPC code package, we define conditions *in normal ionosphere* over VLF propagation path in order to simulate VLF propagation and to get the best fitting pairs of Wait's parameter β_{nor} and H'_{nor} . Here, *nor* means normal condition.
2. In further investigation (step two) we use the method presented in papers (Mitra 1974; Thomson 1993; Grubor 2008) in order to simulate propagation of VLF radio signal through the waveguide in the *disterbed D-region* induced by additional X-ray radiation during an flare event. The amplitude and phase changes, named as SID VLF signatures are:

$$\Delta A = A_{disturbed} - A_{normal}$$

$$\Delta \phi = \phi_{disturbed} - \phi_{normal}$$

are directly measured using reared VLF/LF data during an solar flare event and under normal ionospheric condition (see Figure 5).

3. In the next step we successevely change values of β and H' in LWPC code to obtain: $\Delta A_{calculated}$ and $\Delta \phi_{calculated}$. By a *trial and error* method we have to vary the values of β and H' in LWPC code in order to match as good as posible a pair; $\Delta A_{calculated}$; $\Delta \phi_{calculated}$ with recorded

pair ΔA , $\Delta\phi$. With the help of this fitting procedure we find the best values of β and H' to simulate disturbed ionospheric density profiles.

4. In fourth step the variation of the D-region electron density height profile $N_e(h)$ is reconstructed, and analyzed throughout different solar flare events.

Moreover, recently is shown in the literature (Thomson 2005; Grubor et al., 2008) that the classification of X-ray solar flares can be performed regarding their effects on the VLF wave propagation along the Earth-ionosphere waveguide, and that is the one of the reason for its modeling.

4. THE IONOSPHERIC EFFECTS INDUCED BY SOLAR FLARES ON VLF/LF PROPAGATION

4.1. VLF/LF Propagation under Normal Ionospheric Condition in the D-Region

In literature, the first results about diurnal amplitude variations on VLF signals were published in 1933. Yokoyama and Tanimura (1933) studied propagation of 17.7 kHz and 22.9 kHz, over long distances $D > 5\text{Mm}$. They gave explanation for amplitude fading based on single-ray geometrics optics. Budden (1961) and Wait (1985, 1962, 1964) suggested that many rays are needed to explain VLF propagation over long paths. Crombie (1964) and Walker (1965) put forward an explanation based on the use of modes in the earth-ionosphere waveguide. VLF/LF radio signals are reflected from the lowest region in the ionosphere. An apart from sunrise and sunset, exhibit propagation characteristics are very stable in both amplitude and phase. Typically, VLF radio signals propagate with less attenuation during nighttime due to much lower ionization levels in the D-region. The phenomenon of sunrise and sunset development of amplitude minima is characterized by periodic and repeatable variations in amplitude and phase. These variations are a consequence of moving the sunrise/sunset terminator along a VLF propagation path. Daytime propagation is taken to occur when the solar zenith angle at both the transmitter and the receiver is less than 90° .

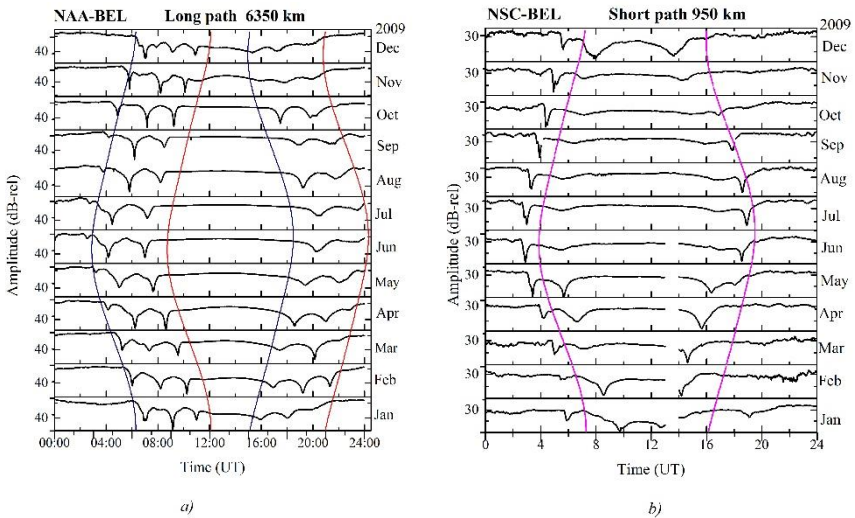


Figure 2. *a)* Typical diurnal amplitude variations on NAA-BEL long path against universal time for each month during 2009, respectively. With blue and red colors are plotted times of sunrise and sunset at Belgrade and Maine, respectively. *b)* Typical diurnal amplitudes variations on NSC-BEL short path for each month during 2009. With magenta color are drawn curves of sunrise and sunset during year, respectively for Belgrade.

For studying the phenomenon of sunrise and sunset development of amplitude minima followed by changes in phase we have selected NAA-BEL long path. Observations of the diurnal amplitude and phase variations of the NAA/24.00 kHz have been made at the Belgrade site for many years. The path is sufficiently long and correctly oriented (west-east) to show sunrise and sunset development of amplitude minima. The transmitter is located in Maine, USA in Time zone UTC -5 and the receiver in Time zone UTC +1. Typical diurnal amplitude records for one day in each month for 2009 are shown in Figure 2 a. Continually changes in time of appearing sunrise and sunset at Belgrade (blue color) and Main (red color) for whole year 2009 are also shown in Figure 2a.

The first point is that the recordings of NAA/24.00 kHz radio signal at Belgrade show three amplitude minima during sunrise. Similar but less evident changes occur during sunset. Secondly it is clear that during sunrise on all twelve curves the amplitude minima which occur at the latest times are the deepest. This minimum occurs when the sunrise line is closest to the transmitter (the western end of the path). Figures 2a shows that amplitude minimum occurs while the sunrise or sunset line lies between the transmitter

and receiver. Figure 3 (panel 2) shows that at the times of amplitude minima the rate of phase changes becomes noticeable on the NAA-BEL path. Timing of occurrences the amplitude minima shows seasonal variation of appearing sunrise or sunset line over path. Our results are in good correlation with results published by Crumbier (1964) and Walker (1965).

Main characteristics of propagation the NAA/24.00 kHz radio signal over long path to Belgrade are developments of three amplitude minima during time interval between sunrise at Belgrade and Maine (difference in time is ~ 6 h). Similar but less evident changes occur during time interval defined by sunsets at Belgrade and Maine. These amplitude minima are followed with changes of phase values over whole year.

As an example of propagation LF radio signal is shown in Figure 2b. Radio signal with frequency NSC/45.90 kHz (Sicily, Italy) propagates from South west to Northeast over short path 950 km. Transmitter and receiver are in same Time zone.

Typical diurnal amplitude records for one day in each month for 2009 are shown in Figure 2 b. Two curves presenting the appearing of sunrise and sunset at Belgrade (magenta color) for whole year 2009 are shown in Figure 2b. The diurnal variation of amplitude has larger values during nighttime than in daytime condition, because of lower absorption during night. Figure 2b shows well defined amplitude minima on all amplitude registrations against time during year. It is evidently that an amplitude minimum occurs before happening sunrise and one after the sunset at Belgrade. Timings of these developments the amplitude minima are in good correlation with appearing sunrise and sunset at the middle of the propagation path. During daytime there is one pair of amplitude minima whose creation is a consequence of destructive interference of modes. The temporal variability in their creation is correlated with number of light hours for each day during year. The amplitude minima in dawn and morning are sharper than in afternoon and dusk and are the sharpest during summer (Tulip et al., 2016).

Under daytime condition over NSC-BEL path two amplitude minima are observed in morning and afternoon. The lowest values of these amplitude minima are recorded under solar zenith angle in morning $\chi = 74^\circ$ and in the afternoon $\chi = 71^\circ$. These amplitude minima are followed with suddenly decreasing of phase values.

4.2. VLF/LF Propagation in Disturbed Ionosphere Conditions

VLF/LF propagation as noted above provides some insight on the way ionization builds up and decays, and provides a routine monitor for the detection and time change of solar-geophysical disturbances. VLF/LF radio signals steeply incident on the ionosphere are reflected from heights within the D-region, and exhibit a cosinusoidal diurnal variation of phase. Such a phase change can be interpreted as giving a measure of the height in the D-region.

Sudden changes in the amplitude and phase of long and short distances subionospheric VLF propagations have been found at daytime in association with events of solar flares. The intensities of VLF and LF radio waves change during an SID in way that it depends on the frequency and on the angle of reflection (Retcliffe, 1972). Behaviors of amplitude and phase perturbations on VLF/LF radio signals induced by different intensity of solar X-ray fluxes, observed on Belgrade site, were examined and these results are presented in recent papers: Grubor et al., 2005, 2008; Zigman et al., 2007; Nina et al., 2012; Šulić and Srećković 2014; Šulić et al., 2016).

4.2.1. SID Effects on VLF Signal Propagation over a Long West-East Path

For example, the diurnal variations of amplitude and phase on NAA/24.00 kHz radio signal against universal time recorded at Belgrade during 05 (normal day) and 08 March 2011 are presented on Figures 3a and 3b.

The first panel of Figure 3a shows the solar X-ray radiation against universal time on 08 March as monitored by GOES-15 satellite. The eruptions of extreme X-ray radiation induce successively four solar flares M class. The solar flares classes: M5.37 ($I_x = 5.37 \cdot 10^{-5} \text{ Wm}^{-2}$ of X-ray flux in the band 0.1-0.8 nm, peak at 10:44 UT) and M4.46 ($I_x = 4.46 \cdot 10^{-4} \text{ Wm}^{-2}$, peak at 18:28 UT) induced phase and amplitude perturbations on NAA/24.00 kHz radio signal which are noticeable in comparing these registrations with NAA/24.00 kHz data recorded 05 March 2011.

As presented in Figure 3a phase (panel 2) and amplitude (panel 3) variations of the NAA/24.00 kHz radio signal track the intensity of X-ray flux quite closely during developments of solar flares.

The solar flare M5.37 class occurred close to local noon at Belgrade and in local morning in Maine, which means illuminations of whole long path NAA-BELL. Very high changes of X-ray radiation induced large huge production of electron in the D-region. The evidence of this SID is measurable with analysis of rising amplitude and phase in according to normal daytime

levels. For example, SID VLF signatures are: $\Delta A \sim 12$ dB and $\Delta\phi \sim 120^\circ$ at timing the maximum of X-ray radiation.

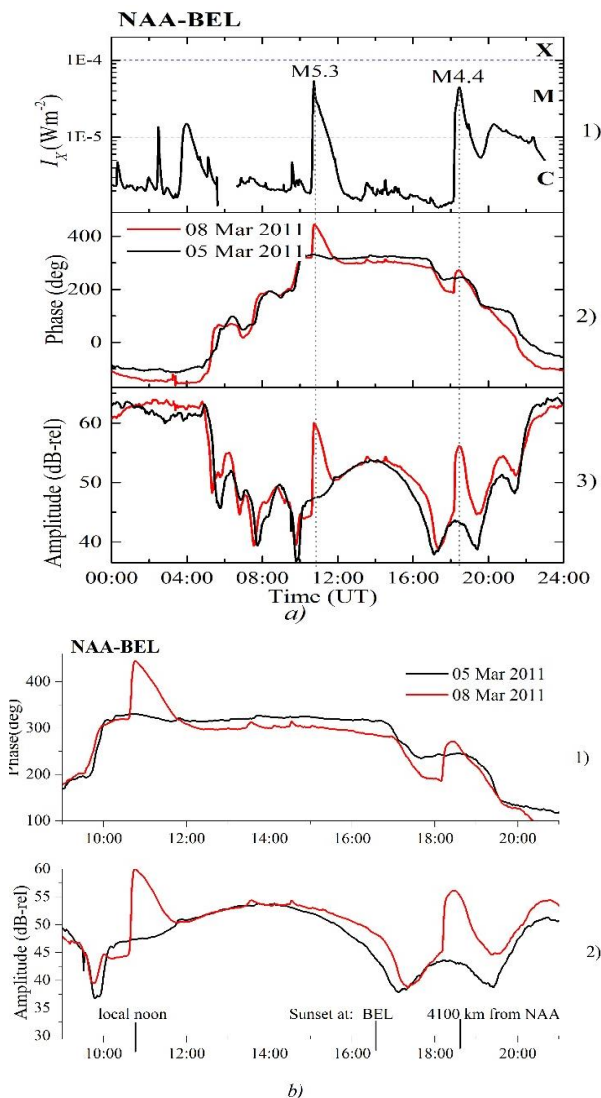


Figure 3. a) Variation of X-ray irradiance (panel 1), phase (panel 2) and amplitude (panel 3) on NAA/24.00 kHz radio signal recorded at Belgrade against universal time on 05 (normal day) and 08 March 2011. The transmitter and receiver are in Time zones UTC-5 and UTC+1, respectively. b) Phase (panel 1) and amplitude (panel 2) on NAA/24.00 kHz radio signal recorded at Belgrade in time interval 10:00-21:00UT.

On 08 March 2011 occurred the solar flare M4.46 ($I_x = 4.46 \cdot 10^{-5} \text{ Wm}^{-2}$ at 18:28 UT) class and induced significant variations of amplitude and phase on NAA/ kHz radio signal. On the panel 3 of Figure 3a, are noticeable three amplitude minima which occurred during time interval defined by sunsets at Belgrade and Maine. The maximum of X-ray radiation was reached at 18:28 UT, approximately two hours later than sunset occurred at Belgrade on 08 March 2011. Following plotted results on Figure 3b (panel 3) timing of solar flare events is between timings of the first and the second amplitude minima during sunset. Using LWPC code we simulated moving the sunset terminator along NAA-BEL path. The maximum of X-ray flux occurred at 18:28 UT and in that moment a sunset terminator was at ~ 4100 km from the NAA transmitter. Propagation of NAA/24.00 kHz radio signal from transmitter to Belgrade has west to east orientation. During this event radio signal propagates under daytime, dusk and nighttime conditions. Changes of amplitude and phase on NAA/24.00 kHz radio signal through the illuminated segment of waveguide were on sufficient levels to be recorded in Belgrade.

On 05 June 2013 southern sunspot AR1762 erupted, producing a long-duration M1.31 ($1.31 \cdot 10^{-5} \text{ Wm}^{-2}$) class solar (begin 08:14 UT, peak 08:57 UT, and 09:26 UT). We selected this event to study the influence of isolated solar flare event and their manifestation on NAA-BEL path. The registrations of amplitude and phase on NAA/24.00 kHz radio signal during normal (black color) and disturbed ionospheric (red color) conditions are shown on Figure 4a. Sudden phase increases produced by solar flare indicate changes of reflection height (Figure 4a panel 1). These changes of phase are following with continuously rising of amplitude (Figure 4a panel 3).

Table 4 SID VLF signatures and calculated data by LWPC code in a function of intensity of X-ray flux during solar flare class M1.31

Date: 05 Jun 2013		NAA-BEL path				
Time UT him	I_x (Wm^{-2})	SID VLF signatures		Calculated data by LWPC code		
		ΔA (dB)	$\Delta \phi$ (deg)	β (km^{-1})	H' (km)	$Ne(H')$ (m^{-3})
08:00	3.55E-7	0	0	0.300	74.0	2.18E + 06
08:23	1.24E-6	0.8	10.7	0.315	73.0	2.49E + 06
08:30	2.54E-6	1.57	18	0.330	72.0	2.93E + 08
08:35	4.5E-6	2.3	26.5	0.348	71.0	3.34E + 08
08:38	6.61E-6	2.9	34	0.368	70.0	3.93E + 08
08.43	9.97E-6	3.42	44.4	0.387	69.0	4.63E + 08
08:56	1.31E-5	3.77	54.4	0.392	68.3	5.05E + 08

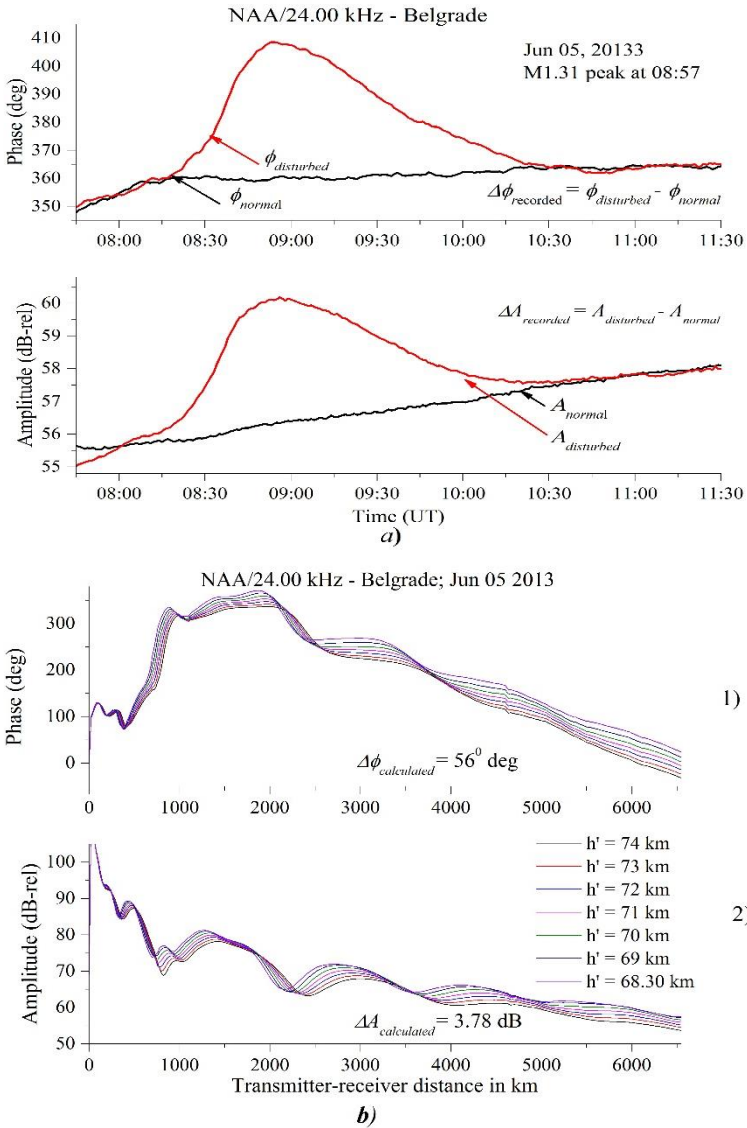


Figure 4. *a*) Diurnal variation of X-ray irradiance (panel 1) and amplitudes (panel 2) on NAA/24.00 kHz radio signal for two days in June 2013. An AbsPAL recording of amplitude during normal day is black line while a recording of amplitude during perturbed day (05 June 2013) is red line; *b*) NAA phase (panel 1) and amplitude (panel 2) signal variations along GCP distance from Maine to Belgrade during M1.31 flare event (05 June 2013).

Using the LWPC code we simulated the propagation of NAA/24.00 kHz radio signal through waveguides where an altitude electron density profile was successively changed. After the mode parameters along each path are determined, the signal strength and phase along each path is computed. In Table 4 are presented calculated results and in this case there is movement of the reflection height H' from 74 km to 68.3 km. The parameter β (km^{-1}) the “sharpness” of the electron profile changes from 0.300 to 0.392.

Variation of phase (panel 1) and amplitude (panel 2) of the radio signal along NAA-BEL path are calculated for seven different reflection heights as it successively moving on lower values. Results for event occurred on 05 June 2013 are presented on Figure 4b. The modal interference minima (Wait, 1962) of the amplitude and phase variation along the NAA-BEL path at regular conditions are displayed on the normal day (black color). During occurrence of M1.31 class solar flare, all modal minima are seen to move towards the transmitter (Thomson and Clilverd, 2001). The typical movement of the modal minima is strongly dependent on the lowering of the reflection height, and it is evidently from Figure 4b.

4.2.2. SID Affects on VLF Signal Propagation over a Short Pat

Sudden changes in the amplitude and phase of long and short distances subionospheric VLF propagations have been found at daytime in association with events of solar flares. The intensities of VLF and LF radio waves change during an SID in way that it depends on the frequency and on the angle of reflection (Retcliffe, 1972). Behaviors of amplitude and phase perturbations on VLF/LF radio signals induced by different intensity of solar X-ray fluxes, observed on Belgrade site, were examined and these results are presented in recent papers: Grubor et al., 2005, 2008; Zigman et al., 2007; Nina et al., 2012; Šulić and Srećković 2014; Šulić et al., 2016).

Our statistical results show that both increases and decreases in signal strength have been observed, depending on: *the intensity of solar X-ray radiation, solar zenith angle and frequency*

DHO/23.40 kHz radio signal propagates from Rhaderhent, Germany to the Belgrade receiver site across an all land path (transmitter and receiver are in the same Time zone). VLF radio signal propagates Northwest to Southeast and the distance between transmitter and receiver site is $D = 1300$ km.

A radio signal with frequency GQD/22.10 kHz (Skelton, UK) propagates from West to East over short path $D = 1980$ km. Radio signal propagates over Central Europe. Perturbations of amplitude on GQD/22.10 kHz exhibit rising

and decreasing during occurrences of solar flares with different levels of intensity on X-ray flux. A phase change on this path is complicated; displaying rise, decrease and oscillation under the occurrences of different classes solar flares.

Solar flare class C6.8 ($I_x = 6.8 \cdot 10^{-6} \text{ Wm}^{-2}$) occurred on 27 February 2014 with intensity maximum at 12:30 UT. Figure 5 gives an instructive example of induced amplitude and phase perturbations on DHO/23.40 kHz and GQD/22.10 kHz, radio signals observed in Belgrade during this event.

On DHO-BEL path the amplitude and phase increase under enhancement of electron density induced by solar flare. Values of SID VLF signatures, $\Delta A = 4.2 \text{ dB}$; $\Delta\phi = 70^\circ$ are in correlation with the intensity of solar X-ray irradiance. Amplitude perturbations on GQD/22.10 kHz radio signal show decreasing with time until the intensity of X-ray radiation reaches the maximum. Phase changes show a different character, displaying increase and also decrease during the occurrence of solar flare C6.8 class. T the moment of intensity maximum of X-ray irradiance SID VLF signature are $\Delta A = -5.4 \text{ dB}$ and $\Delta\phi = 10^\circ$

The intensities of VLF and LF radio waves change during an SID in way that it depends on the frequency and on the angle of reflection (Retcliffe, 1972).

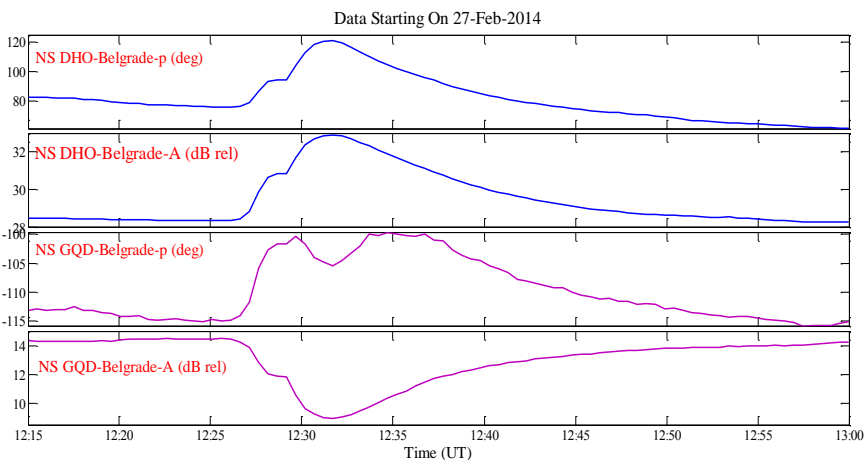


Figure 5. Variation of phase and amplitude on DHO/23.40kHz and GQD/22.10 kHz radio signals recorded at Belgrade against universal time on 27 February 2014.

4.2.3. SID VLF Signatures on a Short Path as a Function of the Intensity Solar X-Ray Radiation

Modified amplitude and phase on GQD/22.10 kHz radio signal by increased X-ray radiation and SID were analyzed during the ascending phase and the maximum of Solar Cycle 24. The monitored amplitude and phase changes on GQD/22.10 kHz radio are results of increased electron density and a decrease in height of the ionosphere boundary. Ionospheric incubation times and duration of perturbations on VLF radio signal are related to intensity of X-ray flare. Characteristics of amplitude and phase on the GQD/22.10 kHz radio signal are presented in papers mentioned earlier. Under normal ionospheric condition stable daytime propagation in waveguide can be characterized by Waits' parameters: $\beta = 0.3$ and $H' = 74$ km. Great segment of GQD-BEL path covers the same time zone where the receiver is, it can be assumed that the whole path is similar illuminated in time sector around local noon in according to the receiver. Amplitude and phase perturbations on GQD/kHz radio signal are strongly dominated by intensity of X-ray radiation and duration of a flare.

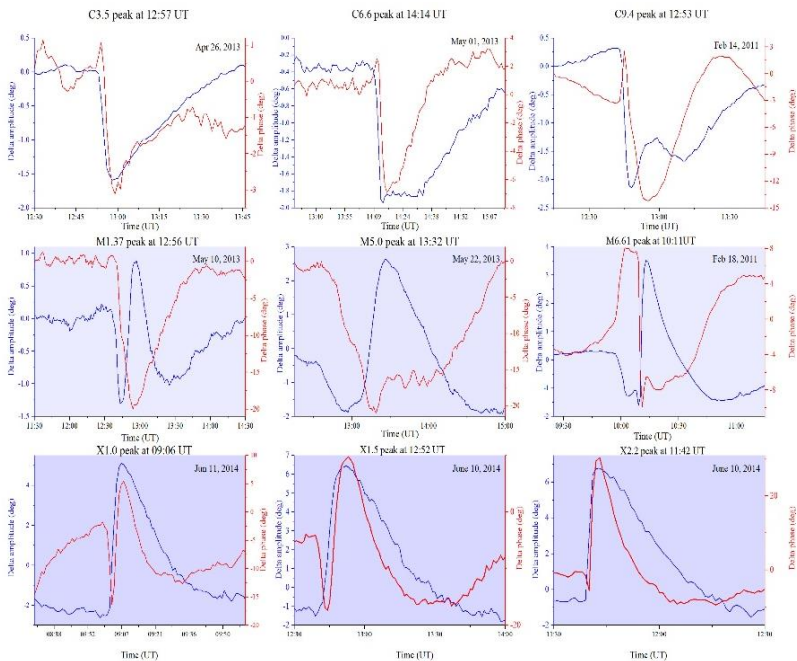


Figure 6. VLF SID signatures of nine solar flare events (ranging from class C3.6 to X2.2) observed on GQD/22.10 kHz radio signal at Belgrade. All events occurred during the ascending phase and the maximum of Solar Cycle 24.

For studying SID VLF signatures on GQD/22.10 kHz we have selected solar flare events whose occurrences were in time intervals of few hours around local noon at Belgrade. All selected nine events (ranging from C3.6 to X2.2 class) were recorded under similar solar zenith angles. Our results are presented on Figure 6 as: *three examples of C class, M class and X class solar flares*. Perturbations of the GQD/22.10 kHz radio signal are presented as temporal changes of ΔA and $\Delta\phi$ during solar flare event.

Table 5. SID VLF signatures and calculated data by LWPC code in a function of intensity of X-ray flux during nine solar flare events (ranging from class C3.6 to X2.2) observed on GQD/22.10 kHz radio signal at Belgrade

GQD-BEL path							
Date	Time UT	I_x Wm ⁻²	SID VLF signatures		Calculated data by LWPC code		
			ΔA dB	$\Delta\phi$ deg	β km ⁻¹	H' km	Ne m ⁻³
	11:00	$5 \cdot 10^{-7}$	0	0	0.30	74.0	2.18E+8
2013/04/26	12:57	C5.57 $3.57 \cdot 10^{-6}$	-1.85	-3	0.36	70.0	9.12 E+8
2013/05/01	14:15	C6.6 $6.6 \cdot 10^{-6}$	-1.9	-6.9	0.38	69.1	1.39 E+9
2011/02/14	12:54	C9.4 $9.4 \cdot 10^{-6}$	-1.5	-14	0.42	67.5	3.31 E+9
2013/05/10	12:57	M1.3 $1.37 \cdot 10^{-5}$	+0.85	-19.4	0.45	65.4	1.04 E+10
2013/05/22	13:32	M5.0 $5.0 \cdot 10^{-5}$	+2.64	-17	0.46	64.4	1.79E+10
2011/02/18	10:11	M6.61 $6.61 \cdot 10^{-5}$	+3.51	-9	0.44	63.95	1.84E+10
2014/06/10	09:06	X1.1 $1.1 \cdot 10^{-4}$	+5.1	+5.0	0.46	62.3	4.70E+10
2014/06/10	09:59	X1.5 $1.5 \cdot 10^{-4}$	+6.46	+10	0.52	61.1	1.78E+11
2014/06/10	11:43	X2.2 $2.2 \cdot 10^{-4}$	+6.74	+30	0.53	59.5	4.70 E+11

Two examples induced by C3.5 ($I_x = 3.5 \cdot 10^{-6} \text{ Wm}^{-2}$ at 12:57 UT) and C6.6 ($I_x = 6.6 \cdot 10^{-6} \text{ Wm}^{-2}$ at 14:14 UT) class solar flares show decreasing of amplitude and phase to minima of values following the rising of intensity of X-ray radiation. The third example of event induced by C9.4 ($I_x = 9.4 \cdot 10^{-6} \text{ Wm}^{-2}$ at 12:57 UT) class solar flare occurred on 14 February 2010. An abrupt decrease of amplitude to minimum precedes the X-ray radiation maximum. Also decrease of phase is noticeable for the plotted results.

Three examples of SID VLF signatures caused by M ($I_x = 1.37 \cdot 10^{-5} \text{ Wm}^{-2}$, $I_x = 5.0 \cdot 10^{-5} \text{ Wm}^{-2}$ and $I_x = 6.1 \cdot 10^{-5} \text{ Wm}^{-2}$) class solar flares are shown in Figure 6. Amplitude and phase perturbations on GQD/22.10 kHz exhibit *decreasing, oscillating and rising* during the duration of solar flares.

Changes of amplitude on GQD signals during three X class solar flares perform as well defined enhancement that follow the development of the maximum in X-ray radiation. Perturbations of phase are not so clearly in rising, the phase maxima are close to peak of X-ray radiation. We scaled the SID VLF signatures at times when X-ray radiations have peaks. Scaled and calculated data by LWPC code are given in Table 4. It is possible to follow the tendency of transformation from negative into positive growth amplitude and phase during these nine solar flare events. For example, a reflection height is lowered from $H' = 74 \text{ km}$ to $H' = 70 \text{ km}$ during C3.5 class solar flare, while during X2.2 class solar flare event a reflection height falls for 14 km. During X2.2 class solar flare event electron density changes for three order of value at reference height $h = 74 \text{ km}$ in according to ambient value.

4.2.4. Calculation of Altitude Electron Density Profile during SIDs

The amplitude and phase of the VLF/LF radio signal received at any point depend on the electrical conductivity of the lower ionosphere as well as the ground. Under the right circumstances the observed properties of VLF/LF radio signals can be used to determine the spatial and temporal structures of disturbances in the lower ionosphere. Typical daytime ionospheric electron density profile shows an increase with altitude. As input parameters in LWPC code we use $\beta = 0.3$ and $h' = 74 \text{ km}$ and calculated electron density profile is defined with $Ne = \sim 10^7 \text{ m}^{-3}$ at $h \sim 55 \text{ km}$ and $Ne \sim 2 \cdot 10^9 \text{ m}^{-3}$ at $h \sim 90 \text{ km}$.

For this paper we selected amplitude and phase perturbations on ICV/20.27 kHz radio signal recorded at Belgrade. Radio signal ICV/20.27 kHz (Isola di Tavolara, Italy) propagates from Southwest to Northeast over short path 980 km.

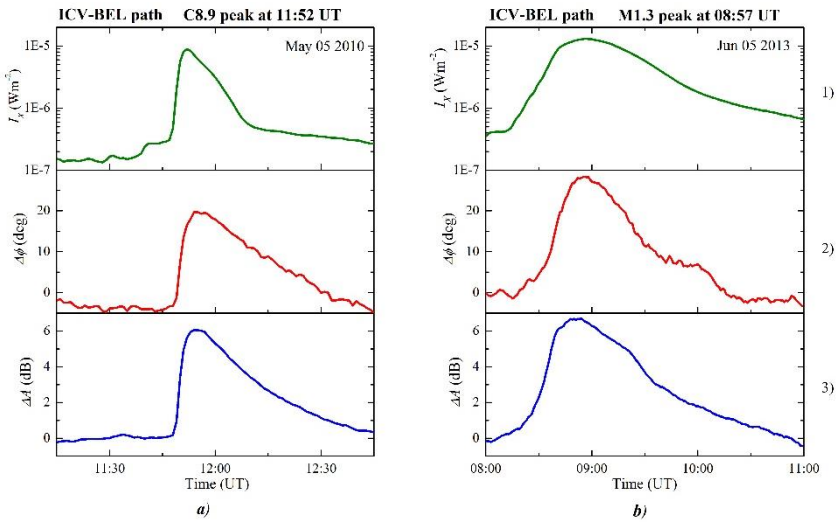


Figure 7. *a*) Variation of X-ray irradiance (panel 1), phase increase (panel 2) and amplitude increase (panel 3) on ICV/20.27 kHz radio signal recorded at Belgrade against universal time on 5 May 2010. *b*) Same as in *a*) but for the 5 Jun 2013.

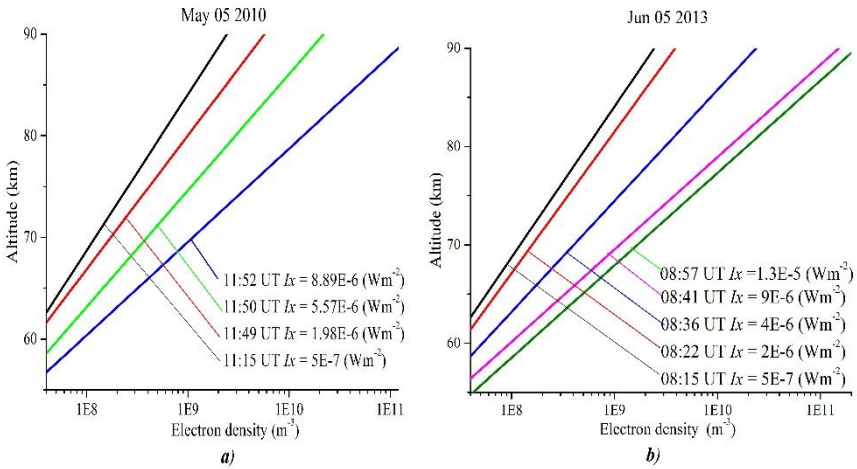


Figure 8. *a*) Electron density height profiles during C8.9 class X-ray solar flare occurred on 5 May 2010. *b*) Same as in *a*) but for the 5 Jun 2013.

On 05 May 2010 occurred suddenly changes in X-ray radiation started at 11:37 UT, reached peak at 11:52 UT and ended at 11:58 UT. The C8.9 ($I_x = 8.8 \cdot 10^{-6} \text{ Wm}^{-2}$) class solar flare induced significant increasing of amplitude and

phase on ICV/20.27 kHz radio signal recorded at Belgrade. The event occurred on 05 June 2013 at 08:14 UT started suddenly changes of X-ray radiation which reached peak at 08:57 UT and ended 09:26 UT. This solar flare M1.31 ($I_x = 1.31 \cdot 10^{-5} \text{ Wm}^{-2}$) belongs to long duration flare. The basis for modeling altitude profile of electron density during event of solar flare are measured amplitude and phase increases (ΔA , $\Delta \phi$) on ICV/20.27 kHz radio signal recorded at Belgrade.

Figure 7a shows variation of X-ray radiation (panel 1), phase increase (panel 2) and amplitude increase (panel 3) on ICV/20.27 kHz radio signal recorded at Belgrade during duration of C8.9 class solar flare. Figure 7b shows variations of X-ray radiation, phase increase and amplitude increase over ICV-BEL path during duration of M1.31 class solar flare. The main difference between these two solar flares is not in intensity of them but in their times of duration.

Under the right defining of Waits' parameters β and H' they are used to determine the spatial structures of disturbances in the lower ionosphere. For our calculations we selected times during which intensity of X-ray radiation uniform changes. Results of electron density profiles calculated in times during durations of C8.9 and M1.31 class solar flares are shown on Figure 8a and 8b, respectively.

There are no great differences in enhancements of electron densities during these two solar flares. At reference height $h = 74 \text{ km}$:

1. $N_e = 3.05 \cdot 10^9 \text{ m}^{-3}$ on 10 May 2010 at 11:52 UT
2. $N_e = 4.44 \cdot 10^9 \text{ m}^{-3}$ on 05 June 2013 at 08:57 UT.

4.2.5. Calculation of Temporal Variation of Electron Density during SID

In this work VLF propagation in the presence of ionospheric disturbances is quantitatively modeled using LWPC code to determine temporal structures of disturbances in the D-region. For this propose we selected solar flare event occurred on 10 May 2013, starting at 12:37 UT Intensity of X-ray radiation reached peak of $I_x = 1.37 \cdot 10^{-5} \text{ Wm}^{-2}$ at 12:58 UT. Suddenly rising of intensity induced additional ionization in the D-region and has implication on amplitude and phase on GQD/22.10 kHz radio signal recorded at Belgrade. Figure 9a shows recordings of phases and amplitudes on GQD/20.10 kHz radio signal on 09 May 2013 (black color) and 10 May 2013 (red color) Recorded data during 09 May 2013 are used as reference level for normal ionospheric condition. The M1.31 class solar flare induces a phase decrease to minimum value and an

oscillation of amplitude. During the duration of the solar flare event amplitude perturbation lays in range $-1.34 < \Delta A < 0.9$ dB.

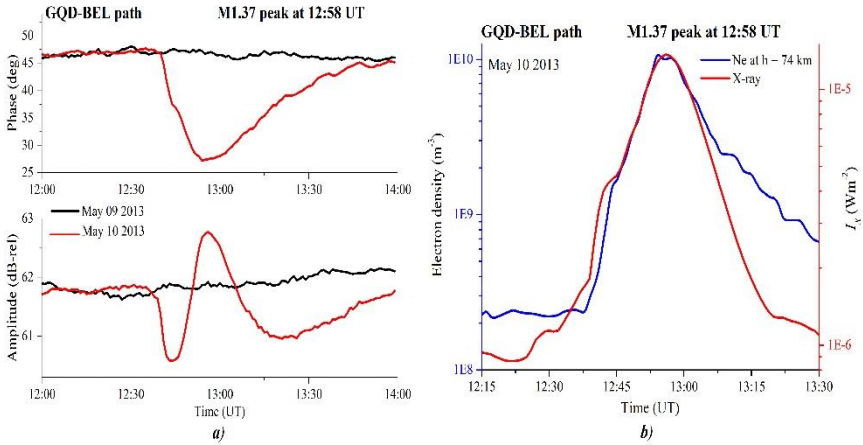


Figure 9. *a)* Variation of phase and amplitude on GQD/22.10 kHz radio signal recorded at Belgrade against universal time on 09 May 2013 and 10 May 2013. *b)* The electron density profile obtained from measured perturbed amplitude and phase of the GQD/22.10 kHz signal at the Belgrade station on 10 May 2013 during M1.37 class solar flare.

In the time interval from 12.00 to 14:00 with step of one minute we calculated Waits parameters' β and H' using observed ΔA and $\Delta\phi$.

Figure 9b shows calculated electron densities and intensity of X-ray irradiance against time. Results show good correlation between intensity of X-ray radiation and electron density variation at reference height $h = 74$ km during duration of M1.31 class solar flare.

CONCLUSION

In this study the amplitude and phase data acquired by monitoring NAA/24.00 kHz, GQD/22.10 kHz, DHO/23.40 kHz, ICV/20.27 kHz and NSC/45.90 kHz radio signals at Belgrade site by AbsPAL and AWESOME receivers from 2008 have been analyzed. This period covers the ascending phase and the maximum of the Solar Cycle 24.

We studied the effect, during quiet solar conditions as well as during the enhancements of X-ray flux due to the solar flares, on the propagating signal.

The VLF/LF perturbations of the radio signals emitted from the world wide transmitters, received and recorded at Belgrade site, and the solar X-ray fluxes monitored by GOES satellites have been brought into correlation with the flare events occurring in this period. By comparative analyzing SID affects on VLF/LF signal propagation over a different path it can be notice that observed VLF/LF perturbations at Belgrade site, during SID, have sensitive dependence on: *X-ray flare intensity, solar zenith angle, solar flare duration and geophysical characteristics of VLF/LF path.*

On the basis of monitored and analyzed VLF data, the model computation (LWPC code) is applied to determine the spatial and temporal structures of disturbances in the D-region, during occurrences of solar C class, M class and X class solar flares. The calculated data are presented in tabulated form as well as in figures. From these results it can be concluded that the explosive X-ray radiation leads to an increased rate of electron production and depending on the flare class the electron density can increase more than few order of magnitudes.

The obtained results confirmed the successful use of applied technique for detecting various explosive space weather phenomena such as solar flares as well for describing and modeling the D-region physical properties during SIDs.

ACKNOWLEDGMENTS

The authors are thankful to the Ministry of Education, Science and Technological Development of the Republic of Serbia for support of this work within projects 176002 and III4402.

REFERENCES

- Barr, R., Jones, D. L., & Rodger, C. J. (2000). ELF and VLF radio waves. *Journal of Atmospheric and Solar-Terrestrial Physics*, 62(17), 1689-1718.
- Bird, R. E., & Riordan, C. (1986). Simple solar spectral model for direct and diffuse irradiance on horizontal and tilted planes at the earth's surface for cloudless atmospheres. *Journal of Climate and Applied Meteorology*, 25(1), 87-97.

- Bothmer, V. and I. A. Daglis (2007). Space weather: physics and effects. *Springer Science & Business Media*.
- Budden, K. G. (1961). Radio waves in the ionosphere: the mathematical theory of the reflection of radio waves from stratified ionised layers. Cambridge University Press.
- Carpenter, D. L., Inan, U. S., Trimpi, M. L., Helliwell, R. A., & Katsufraakis, J. P. (1984). Perturbations of subionospheric LF and MF signals due to whistler-induced electron precipitation bursts. *Journal of Geophysical Research: Space Physics*, 89(A11), 9857-9862.
- Crombie, D. D. (1964). Periodic fading of VLF signals received over long paths during sunrise and sunset. *Journal of Research National Bureau of Standards, Radio Science D*, 68, 27-34.
- Cummer, S. A., Inan, U. S., & Bell, T. F. (1998). Ionospheric D region remote sensing using VLF radio atmospherics. *Radio Science*, 33(6), 1781-1792.
- Ferguson, A., (1998). Computer Programmes for Assessment of Long-Wavelength Radio Communications. Space and Naval Warfare Systems Center, San Diego, CA, Version 2.0., Technical document 3030.
- Goodman, J. M. (2005b). Space weather & telecommunications. *Springer Science & Business Media*.
- Goodman, John M. (2005a) "Operational communication systems and relationships to the ionosphere and space weather." *Advances in Space Research* 36.12: 2241-2252.
- Grubor, D. P., Šulić D. M., and Žigman V. (2008). Classification of X-ray solar flares regarding their effects on the lower ionosphere electron density profile. *Annales Geophysicae* 26, 1731–1740.
- Grubor, D., Šulić, D., and V. Žigman (2005). Influence of Solar X-ray Flares on the Earth-Ionosphere Waveguide. *Serb. Astron. Jour.* 171, 29–35.
- Hargreaves, John K. (1992). *The solar-terrestrial environment*. Cambridge Press.
- Hayakawa, M., & Molchanov, O. A. (2000). Effect of earthquakes on lower ionosphere as found by subionospheric VLF propagation. *Advances in Space Research*, 26(8), 1273-1276.
- Hillger, D. W. and Schmit, T. J. (2011) The GOES-15 Science Test: Imager and Sounder Radiance and Product Validations, NOAA TR NESDIS 104, 101 pp., Washington DC.
- Hillger, D. W., and Schmit, T. J. (2009). The GOES-13 Science Test: A Synopsis, *Bull. Amer. Meteor. Soc.*, 90, 6-11.

- Hillger, D. W., and Schmit, T. J. (2007). Imager and Sounder Radiance and Product Validation for the GOES-13 Science Test. *NOAA Technical Report, NESDIS 125*, (September), 75 pp.
- Inan, U. S., Carpenter, D. L., Helliwell, R. A., & Katsufakis, J. P. (1985). Subionospheric VLF/LF phase perturbations produced by lightning-whistler induced particle precipitation. *Journal of Geophysical Research*, 90(A8), 7457-7469.
- Jakowski, N., Mielich, J., Borries, C., Cander, L., Krankowski, A., Nava, B., & Stankov, S. M. (2008). Large-scale ionospheric gradients over Europe observed in October 2003. *Journal of Atmospheric and Solar-Terrestrial Physics*, 70, 1894-1903.
- Leckner, Bo. (1978). "The spectral distribution of solar radiation at the Earth's surface elements of a model." *Solar energy* 20.2 143-150.
- McRae, W. M., Thomson, N. R., (2000). VLF phase and amplitude: daytime ionospheric parameters. *J. Atmos. Sol.-Terr. Phys.* 62, 609–618.
- McRae, W. M., Thomson, N. R., (2004). Solar flare induced ionospheric D region enhancements from VLF amplitude observations. *J. Atmos. Sol.-Terr. Phys.* 66, 77–87.
- Menzel, P. and Purdom, J. (1994). Introducing GOES-I: The First of a New Generation of Geostationary Operational Environmental Satellites. *Bull. Amer. Meteor. Soc.*, 75,757–781, doi:10.1175/15200477(1994) 075 <0757:IGITFO> 2.0.CO; 2.
- Mitra, A. P., & Rowe, J. N. (1972). Ionospheric effects of solar flares—VI. Changes in D-region ion chemistry during solar flares. *Journal of Atmospheric and Terrestrial Physics*, 34(5), 795-806.
- Mitra, A. P., (1974). *Ionospheric Effects of Solar Flares*, Astrophysics and Space Science Library, vol. 46. D. Reidel Publishing Company, Boston.
- Nina, A., Čadež, V., Srećković, V. A., & Šulić, D. (2011). The Influence of Solar Spectral Lines on Electron Concentration in Terrestrial Ionosphere. *Baltic Astronomy*, 20, 609-612.
- Nina, A., Čadež, V., Srećković, V. A., Šulić, D., (2012a). Altitude distribution of electron concentration in ionospheric D-region in presence of time varying solar radiation flux. *Nucl. Instrum. Methods B* 279, 110–113.
- Nina, A., Čadež, V., Srećković, V. A., Žigman, V., (2012b). Effective electron recombination coefficient in ionospheric D-region during the relaxation regime after solar flare from February 18, 2011. *Nucl. Instrum. Methods B* 279, 106–109.
- Prölss, G. (2004). *Physics of the Earth's space environment: an introduction.* Springer Science & Business Media.

- Ratcliffe, J. A. (1972). Introduction to the ionosphere and magnetosphere. Cambridge University Press, New York.
- Šulić Desanka M, Srećković Vladimir A (2014). A Comparative Study of Measured Amplitude and Phase Perturbations of VLF and LF Radio Signals Induced by Solar Flares, *Serbian Astronomical Journal*, vol. 188, 45-54.
- Šulić Desanka M, Srećković Vladimir A, Mihajlov Anatolij A (2016). A study of VLF signals variations associated with the changes of ionization level in the D-region in consequence of solar conditions, *Advances in Space Research*, vol. 57, 4, 1029-1043.
- Thomson, N. R. and Clilverd, M. A. (2001). Solar flare induced ionospheric D-region enhancements from VLF amplitude observations. *Journal of Atmospheric and Solar-Terrestrial Physics* 63, 1729–1737.
- Thomson, N. R., Clilverd, M. A., & Rodger, C. J. (2014). Low-latitude ionospheric D region dependence on solar zenith angle. *Journal of Geophysical Research: Space Physics*, 119(8), 6865-6875.
- Thomson, N. R., Rodger, C. J. and Clilverd, M. A. (2011). Daytime d region parameters from long-path vlf phase and amplitude. *Journal of Geophysical Research: Space Physics (1978–2012)* 116(A11).
- Thomson, N. R., (1993). Experimental daytime VLF ionospheric parameters. *Journal of Atmospheric and Solar-Terrestrial Physics* 55 (2), 173–184.
- Thomson, N. R., Clilverd, A. M., (2000). Solar cycle changes in daytime VLF subionospheric attenuation. *J. Atmos. Solar Terr. Phys.* 62, 601–608.
- Thomson, N. R., Rodger, C. J., Clilverd, M. A., (2005). Large solar flares and their ionospheric D region enhancements. *J. Geophys. Res.* 110, A06306.
- Wait, J. R. (1962). Electromagnetic Waves in Stratified Media. UK: Pergamon Press, Oxford, UK.
- Wait, J. R. and K. P. Spies (1964). in *Characteristics of the Earth-ionosphere waveguide for VLF radio waves*, Technical Note 300, National Bureau of Standards. CO: Boulder CO.
- Walker, D., (1965). Phase steps and amplitude fading of VLF signals at dawn and dusk. Radio Sci. 69D, Journal of Research National Bureau of Standards.
- Woods, T. N., Tobiska, W. K., Rottman, G. J. and Worden, J. R. (2000), Improved solar Lyman-alpha irradiance modeling from 1947 through 1999 based on UARS observations, *J. Geophys. Res.*, 105, 27195–27215.
- Yokoyama, E., & Tanimura, I. (1933). Some long-distance transmission phenomena of low-frequency waves. *Proceedings of the Institute of Radio Engineers*, 21(2), 263-270.

Žigman, V., Grubor, D. and Šulić D. (2007). D-region electron density evaluated from VLF amplitude time delay during X-ray solar flares. *Journal of Atmospheric and Solar-Terrestrial Physics* 69, 775–792.

BIOGRAPHICAL SKETCH

Sreckovic Vladimir

Affiliation: Institute of Physics, University of Belgrade, Serbia

Education:

- 2000. B.Sc. Diploma in Physics, Faculty of Physics, University of Belgrade, Serbia
- 2006 M.Sc. in Physics, Faculty of Physics, University of Belgrade, Serbia
- 2010 Ph.D. Thesis in Physics, Faculty of Physics, University of Belgrade, Serbia

Research and Professional Experience:

Research Interests:

- Numerical simulations and modeling of astrophysical plasma.
- High performance computing.
- Space Weather studies of Upper Atmosphere, Ionospheric plasma Irregularities using VLF, Atmospheric studies.
- The analysis of large datasets, i.e., “Big Data” and “Extreme Data.”
- Development of databases and work with very massive database.

Dr. Sreckovic V. participated in few national and international and bilateral projects. He is supervisor of PhD dissertations and leader of national projects. Reviewer in several international journals and projects. Dr. Sreckovic also work in popularization of science. He is the recipient of several awards in research. Dr. Sreckovic has been a presenter for several tens of workshops and conferences.

Scientific papers and lectures:

32 papers in ISI international journals, More than hundreds of proceedings papers, and a lot of invited lectures at international conferences.

Professional Appointments:

2003 – 2006 Junior Researcher Institute of Physics, University of Belgrade, Belgrade, Serbia

2006 – 2010 Research Assistant Institute of Physics, University of Belgrade, Belgrade, Serbia

2010 – 2015 Assistant Professor Institute of Physics, University of Belgrade, Belgrade, Serbia

2015 - Associate Professor Institute of Physics, University of Belgrade, Belgrade, Serbia

Honors: The award for the best master thesis at the Faculty of Physics, Belgrade University, for 2005/06. year from the fund, “prof. Dr. Ljubomir Ćirković.”

Publications:***Papers in international journals:***

1. Šulić, D. M.; Srećković, V. A.; Mihajlov, A. A. (2016) *A study of VLF signals variations associated with the changes of ionization level in the D-region in consequence of solar conditions* Advances in Space Research, Volume 57, Issue 4, p. 1029-1043
2. Mihajlov, A.A.; Srećković, V.A.; Ignjatović, Lj. M.; Dimitrijević, M. S. (2016) *Atom-Rydberg-atom chemi-ionization processes in solar and DB white-dwarf atmospheres in the presence of (n - n')-mixing channels* Monthly Notices of the Royal Astronomical Society, Volume 458, Issue 2, p.2215-2220
3. Nina, A., Simić, S., Srećković, V. A. & Popović, L. Č. (2015). *Detection of short-term response of the low ionosphere on gamma ray bursts.* Geophysical Research Letters, 42, 8250-8261.
4. Arefieff K.N., Miculis K., Bezuglov N.N., Dimitrijevic M.S., Klyucharev, A. N., Mihajlov A.A. & V.A., Sreckovic. (2015). *Dynamics Resonances in Atomic States of Astrophysical Relevance*, Journal of Astrophysics and Astronomy, 36, Issue 4, pp.613-622

5. Mihajlov, A., Ignjatovic, L. M., Sreckovic, V., Dimitrijevic, M. & Jevremovic, D. (2015). *Ion-Atom and Atom-Atom Collisional Processes and Modeling of Stellar Atmospheres*. *Astronomicheskij Tsirkulyar*, 1626, 1-13.
6. Mihajlov A.A., Sreckovic V.A. & N.M., Sakan. (2015a). *Inverse Bremsstrahlung in Astrophysical Plasmas: The Absorption Coefficients and Gaunt Factors*, *Journals of Astrophysics and Astronomy*, 36, Issue 4, pp.635-642
7. Mihajlov A.A., V.A.Sreckovic, Ignjatovic L.J.M., Klyucharev A.N., Dimitrijevic M.S. & N.M. Sakan. (2015). *Non-elastic processes in atom - Rydberg atom collisions: Review of state of art and problems*, *Journal of Astrophysics and Astronomy*, 36, Issue 4, pp.623-634
8. Vujcic V., Jevremovic D., Mihajlov A.A., Ignjatovic L.J.M., Sreckovic V.A., Dimitrijevic M.S. & M., Malovic. (2015). *MOL-D A Collisional Database and Web Service within the Virtual Atomic and Molecular Data Center*, *Journals of Astrophysics and Astronomy*, 36, Issue 4, pp.693-703
9. Ignjatović, Lj.M., Srećković, V.A., Mihajlov, A.A. and Dimitrijević, M.S. (2014) *Absorption non-symmetric ion-atom processes in helium-rich white dwarf atmospheres*, *Monthly Notices of the Royal Astronomical Society* Vol: 439 Issue: 3 Pages: 2342-2350 ISSN: 0035-8711 DOI: 10.1093/mnras/stu058
10. Ignjatović, Lj.M., Mihajlov, A.A., Srećković, V.A. and Dimitrijević, M.S. (2014) *The ion-atom absorption processes as one of the factors of the influence on the sunspot opacity*, *Monthly Notices of the Royal Astronomical Society* Vol 441 Issue: 2 Pages: 1504-1512 ISSN: 0035-8711 DOI: 10.1093/mnras/stu638
11. Bezuglov, N. N., Klyucharev, A. N., Mihajlov, A. A. and Srećković, V. A. (2014) *Anomalies in radiation-collisional kinetics of Rydberg atoms induced by the effects of dynamical chaos and the double Stark resonance*, *Advances in Space Research* Vol 54 Issue: 7 Pages: 1159-1163 ISSN: 0273-1177 DOI: 10.1016/j.asr.2013.08.028
12. Šulić, D. M. and Srećković, V. A. (2014) *A comparative study of measured amplitude and phase perturbations of VLF and LF radio signals induced by solar flares*, *Serbian Astronomical Journal* Vol 188 Pages: 45-54 ISSN: 1450-698X DOI: 10.2298/saj1488045s
13. Srećković, V. A., Mihajlov, A. A., Ignjatović, Lj M. and Dimitrijević, M. S. (2014) *Ion-atom radiative processes in the solar atmosphere: quiet Sun and sunspots*, *Advances in Space Research* Vol 54 Issue: 7 Pages: 1264-1271 ISSN: 0273-1177 DOI: 10.1016/j.asr.2013.11.017

Conference papers:

- Vinković, D.; Gritsevich, M.; Srećković, V.; Pečnik, B.; Szabó, G.; Debattista, V.; Škoda, P.; Mahabal, A.; Peltoniemi, J.; Mönkölä, S.; Mickaelian, A.; Turunen, E.; Kákona, J.; Koskinen, J.; Grokhovsky, V. *Big data era in meteor science* Proceedings of the International Meteor Conference, Egmond, the Netherlands, 2-5 June 2016, Eds.: Roggemans, A.; Roggemans, P., ISBN 978-2-87355-030-1, pp. 319-329
- Vladimir A. Sreckovic, VLF Data Acquisition and database storing, *The book of abstracts: The BigSkyEarth workshop*, Brno, Czech Republic 2016 p.45
- Vladimir A. Sreckovic, A.A. Mihajlov, D.M.Sulic, A.Nina and Lj.M.Ignjatovic, VLF Remote Sensing of the Lower Ionospheric Disturbance Caused by Intense Solar Radiation, *The book of abstracts SCSLSA 2015*, Eds. L.C.Popovic, M.S.Dimitrijevic, Sasa Simic, pp.66
- A.A.Mihajlov, Vladimir A. Sreckovic, M.S.Dimitrijevic and A.N.Kljucharev, Non-elastic processes in atom - Rydberg atom collisions: Review of state of art and problems, *The book of abstracts SCSLSA 2015*, Eds. L.C.Popovic, M.S.Dimitrijevic, Sasa Simic, pp.50
- A. Nina, V. M. Čadež, L. Č. Popović, D. Jevremović, M. Radovanović, A. Kolarski, V. A. Srećković, J. Bajčetić, B. Milovanović, A. Kovačević, "Low Ionospheric Perturbations and Natural Hazards" *Proceedings of The International Conference "Natural disasters - links between science and practice,"* 23-24. April 2015, Saransk, Russia, ISBN 978-5-7103-3078-4, УДК 502.1:001.4 ББК Б1 pp: 2013-2018
- A.A. Mihajlov, N.M. Sakan and V.A.Sreckovic, The Inverse bremsstrahlung in astrophysical plasmas: The absorption coefficients and Gaunt factors, *The book of abstracts SCSLSA 2015*, Eds. L.C.Popovic, M. S. Dimitrijevic, Sasa Simic, p.49
- D. Jevremovic, A. A. Mihajlov, V. A. Sreckovic, L. M. Ignjatovic, M. S. Dimitrijevic, and V. Vujcic, MOL-D a Collisional Database Repository and Web Service Within the Virtual Atomic and Molecular Data Centre, *The book of abstracts SCSLSA 2015*, Eds. L. C. Popovic, M. S. Dimitrijevic, Sasa Simic, p.39
- D. Jevremovic, A. A. Mihajlov, V. A. Sreckovic, L. M. Ignjatovic, M. S. Dimitrijevic, and V. Vujcic, MOL-D A Database for Photo-Dissociation Cross-Sections for Individual Ro-Vibrational States of Diatomic Molecular Ions *The book of abstracts The Twenty-fourth Colloquium on High Resolution Molecular Spectroscopy*, August 24 – 28, 2015

- Universit´e Bourgogne Franche-Comte Dijon – France, Eds Vincent Boudon, p.277
- A. A. Mihajlov, V. A. Srećkovic and M. S. Dimitrijevic, Chemi-Ionization Processes Caused by the Creation of Quasi Molecular Complexes in Atom - Rydberg Atom Collisions *The book of abstracts The Twenty-fourth Colloquium on High Resolution Molecular Spectroscopy*, August 24 – 28, 2015 Universit´e Bourgogne Franche-Comte Dijon – France, Eds Vincent Boudon p.278
- Srećković V.A., Mihajlov A.A., Ignjatović L.M., Dimitrijević M.S. *The Non-Symmetric Ion-Atom Absorption Processes in the Helium Rich White Dwarf Atmospheres in UV and EUV Region* (PR) SPIG 2014 International Symposium on the Physics of Ionized Gases; 2014; Belgrade, *Journal of Physics: Conference Series* Volume 565 012022(12) 10.1088/1742-6596/565/1/012022.
- Sakan N.M., Mihajlov A.A., Srećković V.A. *Inverse Bremsstrahlung Absorption coefficients for Dense Hydrogen Plasma in Cut- Off Coulomb Potential Model*. 27th SPIG 2014 International Symposium on the Physics of Ionized Gases 2014, Belgrade Book of Contributed Papers & Abstracts of Invited Lectures and Progress Reports (Eds. Dragana Marić, Aleksandar R. Milosavljević and Zoran Mijatović) p 513-516.
- Nina A., Čadež V.M., Popović L.Č., Srećković V.A., Simić S. *Application of terrestrial low ionospheric plasma diagnostic for detection astrophysical phenomena*, X PDP Symposium on Physics and Diagnostics of Laboratory and Astrophysical Plasmas; 2014; Belgrade. Proceedings (Eds. M.M.Kuraica, B.M.Obradovic and N.Cvetanovic) p. 66-69.
- Srećković V., Joković D., Šulić D., Maletić D., Savić M., Nina A., et al., *Comparative study of solar events with ground based CR and VLF stations*. ECRS 2014, 24th European Cosmic Ray Symposium; 2014; Kiel, Germany, p. 61.
- Nina A, Čadež V.M., Popović L.Č., Srećković V.A., Simić S. *Differences in detection of D-region perturbations induced by UV, X and γ radiation from outer space using VLF signals* (IX BSACA) Astronomical Conference: Astroinformatics 2014; 1-4 July, 2014, SOFIA, Bulgaria, Book of abs. p. 34.
- Nina A., Cadez V.M., Popovic L.C., Srećkovic V.A., Simic S. *Detection of terrestrial ionospheric perturbations caused by different astrophysical phenomena.*, XVII NKAS; Belgrade, Serbia 2014. Book of abstracts, (eds. S. Segan, S. Ninkovic, A. Kovacevic and B. Novakovic) p. 94. ISBN:978-86-7589-089-0.

-
- Mihajlov A.A., Ignjatović L.M., Srećković V.A., Dimitrijević M.S., *Sunspots opacity: the ion-atom absorption processes*, XVII NKAS; Belgrade, Serbia 2014. Book of abstracts, (eds. S. Segan, S. Ninkovic, A. Kovacevic and B. Novakovic) p. 81. ISBN:978-86-7589-089-0.
- Srećković V.A. and Šulić D.M., *Untypical perturbations on VLF radio signals during solar flares*, XVII NKAS; Belgrade, Serbia 2014. Book of abstracts, (eds. S. Segan, S. Ninkovic, A. Kovacevic and B. Novakovic) p. 87. ISBN:978-86-7589-089-0

Chapter 4

SOLAR FLARES ON TRANSITION FROM THE GRAND MAXIMUM TO THE MINIMUM?

V. G. Kossobokov^{1,2,*}, J. L. Le Mouél² and V. Courtillot²

¹Institute of Earthquake Prediction Theory and Mathematical Geophysics,
Russian Academy of Sciences, Moscow, Russian Federation

²Department of Geomagnetism and Paleomagnetism, Institut de Physique
du Globe de Paris, Paris, France

ABSTRACT

The anomalous character of Solar Cycle 23, which ended in the summer of 2009, has been pointed out. It is even proposed that the solar dynamo is undergoing a transition from a state of “grand maximum” to one of “low activity cycles.” We analyze the time distribution of the number and energy of solar flares, and the duration of intervals between them, from Cycles 21 to the declining Cycle 24. The long duration of Cycle 23 (12.8 years based on sunspots, 13.2 years based on flares), the long interval with no C2+ flare between the end of Cycle 23 and the start of Cycle 24 (466 days) are remarkable compared to the two earlier cycles. The singular shape of Cycle 23 is increasingly striking: the first $\approx 70\%$ of the cycle display (on a logarithmic scale) linearly rising maxima, whereas minima are aligned along a descending slope for the latter part of the

* Corresponding author: V. G. Kossobokov, Institute of Earthquake Prediction Theory and Mathematical Geophysics, Russian Academy of Sciences, 84/32 Profsoyuznaya Street, Moscow, Russian Federation; E-mail: volodya@mitp.ru.

cycle. The energy flux oscillates between these and takes the shape of a bifurcation, starting near 2002. Inter-event intervals between successive C2+ flares undergo quasi-periodic (≈ 11 yr) oscillations between two distinct states, which we call “active” and “quiet,” with extremely sharp onset and termination. It has been proposed that anomalous Cycle 23 resembles Cycle 4, which was followed by reduced Cycles 5 and 6 at the time of the Dalton minimum in solar activity. The present, updated analysis of the evolution of solar flares and sunspots in Cycle 24 is in agreement with the hypothesis of a multi-decadal decline in solar activity, following the Grand Maximum that spanned Cycles 18 to 23. Specifically, the dynamics of the solar flare series along with the number of sunspots reveal a pattern of bimodal activity and the ongoing Cycle 24 fits remarkably well the behaviour observed in Cycles 5, 6, and 12, each of which has the total sunspot number in the lowest quartile of this value since 1700. Cycle 24 seems to be a member of this group of lowest solar activity cycles. It should fade away to the solar minimum in about 1 to 3 years.

Keywords: solar activity, international sunspot numbers, solar flares, the Dalton minimum

INTRODUCTION

Predictions of future solar activity are used by space weather specialists and are of interest as tests of our understanding of the physics of the solar dynamo. In 2008, *Pesnell* analyzed 54 early predictions of the amplitude of then upcoming Solar Cycle 24, i.e., predictions made before the occurrence of the solar minimum, and attempted to rate them. The wide range of predicted solar activity, with maximum sunspot number ranging from 40 to 185 (with an average of 117 ± 33), underlined our inability to make robust predictions. Several studies that appeared also in 2008 illustrated the large remaining uncertainties. We may quote *Baranovski et al.*, (2008), who developed a nonlinear dynamics approach (see also an earlier attempt by *Sello*, 2001) and concluded that Cycle 24 would be neither very strong nor very weak, and *Duhau and de Jager* (2008), who suggested that the solar dynamo was undergoing a state transition from a Grand Maximum to Regular Oscillations.

The extremely long duration of the Cycle 23 to 24 minimum came as an unexpected surprise, providing new challenges for the prediction of a potentially exceptional Cycle 24. *Hathaway and Rightmire* (2010, 2011) found that meridional flow velocity had been higher than usual during that minimum,

and Russell et al., (2010) pointed out that the end of Cycle 23 would occur at least two years after the expected date and that indicators of solar and geomagnetic activity were at their historical lows. A recent, comprehensive review of predictions of solar activity has been published by Clette and Lefevre (2012). These authors underline unprecedented anomalies in Cycle 23: “a long period of low activity,” “unprecedented low levels for various series of solar irradiance and particle flux measurements”), “a strong global deficit of the smallest sunspots starting around 2000.” They conclude that the Sun “seems to be actually returning to a past and hardly explored activity regime ending before the 1955-1995 Grand Maximum.”

Interestingly, Clette and Lefevre (2012) noted that mutual relations between solar indices and fluxes seem to have changed at the time of the minimum. Le Mouél et al., (2012) have studied secular changes in correlation between geomagnetic indices and variations in solar activity and found strong losses of correlation during the declining phase of Cycle 20 and in Cycle 23; Blanter et al., (2013) find some evidence of divergence between two ranges of 27-day periods in geomagnetic indices occurring in Cycles 21 and also 23. Comparing magnetic cycles 20-21 and 23-24, they discuss the ways in which this drop of correlation in Cycle 23 may announce unusual properties of Cycle 24. On-going Solar Cycle 24 indeed appears to violate many past predictions, of both magnitude and timing. Clette and Lefevre (2012) raised several questions on mechanisms of spot formation and decay, and on local near-surface vs global deep-seated dynamos. They predicted that the maximum of Cycle 24 would take place between 2012.9 and 2014.1.

Solar flares are an important part of solar activity, associated with rapid and intense energy release in active regions of the solar atmosphere. Their source is the energy stored in magnetically highly stressed configurations of the corona: they are triggered by instabilities in magnetic configuration. During flares, energy is converted into accelerated non-thermal particles, electromagnetic radiation, and heating (and motions within) the coronal/chromospheric plasma. The amount of energy released in flares as reported to this date varies between 10^{17} and 10^{26} joules. The behavior of solar flares can now be observed in detail and their physics is rather well understood (e.g., Aschwanden, 2006 and references therein).

In a previous paper (Kossobokov et al., 2012) we analyzed the temporal distribution of the number and energy of solar flares, and the duration of intervals between them, over Cycles 21 to 23. We considered flares of class C2 and larger (C2+) from the Geostationary Operational Environmental Satellites (GOES) catalogue. Daily values of X-ray flux (wavelengths 1 to 8

Å) have been computed by summing the energy proxies of the events. The series of daily numbers of C2+ solar flares are strongly correlated to their daily energy flux. The long duration of Cycle 23 (12.8 years based on sunspots, 13.2 years based on flares) and the long interval with no C2+ flare between the end of Cycle 23 and the start of Cycle 24 (466 days) are remarkable compared to the two earlier cycles. Inter-event intervals between successive C2+ flares undergo quasi-periodic (≈ 11 years) oscillations between two distinct states, which we called “active” and “quiet,” with extremely sharp onset and termination. We proposed that anomalous Cycle 23 resembles Cycle 4, which was followed by reduced Cycles 5 and 6 at the time of the Dalton minimum in solar activity, often associated with a cooler global climate. In the present paper, we update the analysis from January 2011 through July 2016 and discuss whether this inclusion sheds light on the unusual structure of ongoing Cycle 24 and on its future.

DATA

As in (Kossobokov et al., 2012), we use the catalogue of soft X-ray (SXR) solar flares compiled from observations of the Geostationary Operational Environmental Satellites (GOES). The catalogue consists of more than 77,500 events from September 1st 1975 to July 31st 2016, and covers the three most recent solar cycles 21-23 and the on-going cycle 24. The catalogue and details about event selection criteria can be found at <ftp://ftp.ngdc.noaa.gov/>.

In order to rank the intensity of flares detected by GOES, an index named *GOES X-ray Class* is used, which corresponds to the peak burst intensity I_p measured in the wavelength band 1-8 Å. The classes are defined in the following way: A class if $10^{-8} < I_p < 10^{-7} \text{ Wm}^{-2}$, B class if $10^{-7} < I_p < 10^{-6} \text{ Wm}^{-2}$, C class if $10^{-6} < I_p < 10^{-5} \text{ Wm}^{-2}$, M class if $10^{-5} < I_p < 10^{-4} \text{ Wm}^{-2}$, and X class if $I_p > 10^{-4} \text{ Wm}^{-2}$. Each event in a class is written with a letter followed by a number which allows one to fully identify the value of I_p (e.g., C4.6 class means that $I_p = 4.6 \times 10^{-6} \text{ Wm}^{-2}$). The integrated flux (from event start to end) is also provided in the catalogue, beginning in January 1997. A comparison of the integrated flux and the peak burst intensity shows a reasonably good proportionality between the two quantities (Kossobokov et al., 2008), allowing us to consider the GOES X-ray class as a good proxy for energy flux.

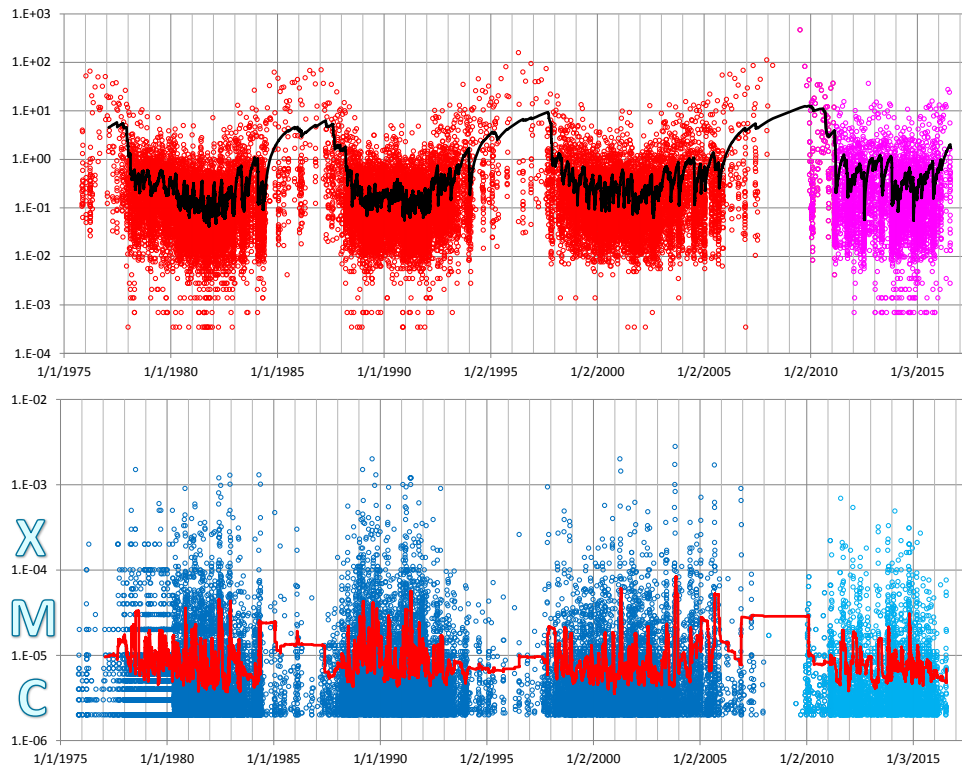


Figure 1. Upper part - Inter-event intervals between successive C2+ events in GOES catalogue of flares. Black line is moving 100-event average. Lower part - Energy flux of GOES X-ray Class of C2+ flares in 1975-2016, in Wm^2 . Red line is moving 100-event average. Logarithmic scales in both parts of the Figure.

Complimentary Contributor Copy

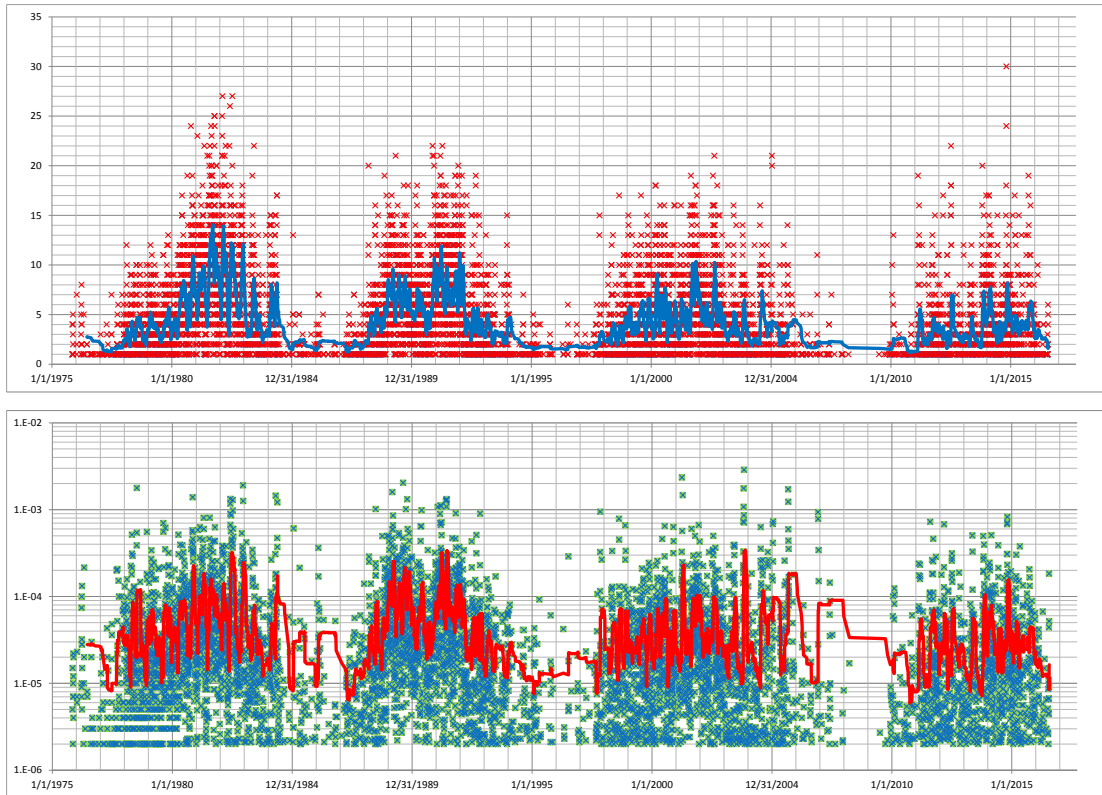


Figure 2. Daily number of Class C2 or larger solar flares $DN(t)$ (above) and daily energy flux proxy $DX(t)$ in Wm^{-2} (below) with their moving 30-days average.

Complimentary Contributor Copy

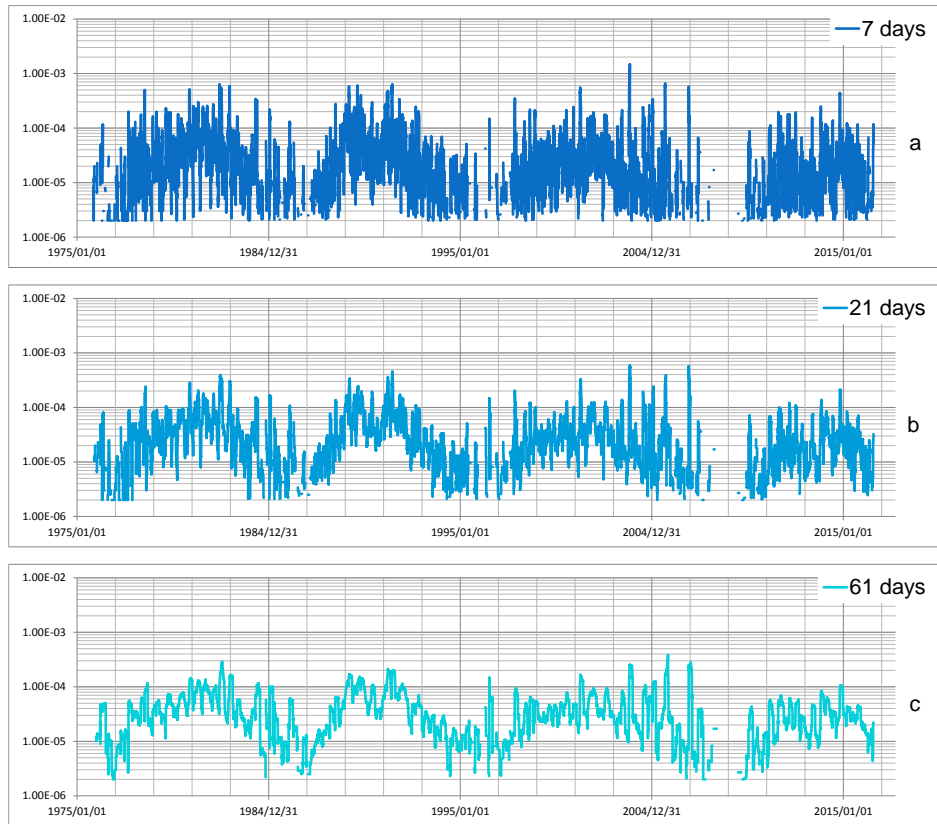


Figure 3. (Continued).

Complimentary Contributor Copy

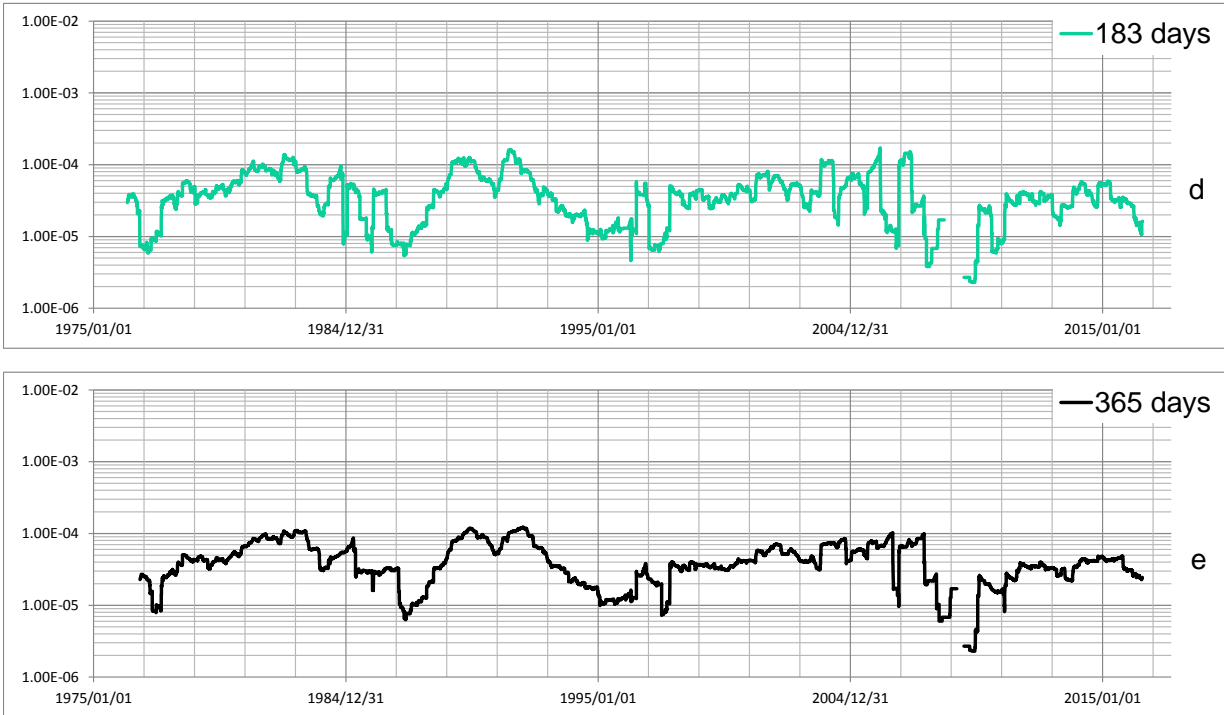


Figure 3. Moving averages $\langle DX \rangle_{\Theta}(t)$ of the daily energy flux $DX(t)$ in Wm^{-2} : a – $\Theta = 7$ days, b – $\Theta = 21$ days, c – $\Theta = 61$ days, d – $\Theta = 183$ days, e – $\Theta = 365$ days.

The GOES catalogue of 32,355 flares has a 1-month long gap (precisely from 2012/08/15 14:48 to 2012/09/19 05:43). In order to bridge this gap, we have used the Hinode EIS Flare Catalogue (Watanabe et al., 2012) as a supplement and also as an independent database for comparison with the results characterizing Cycle 24 obtained when using GOES data. The on-line version of the Hinode catalogue (<http://msslxr.mssl.ucl.ac.uk:8080/SolarB/eisflare.jsp>) has 7024 entries from October 28th 2006 to March 30th, 2013. Although the Hinode data is slightly less complete than GOES, more than 95% of their flare intensity class determinations are identical to those reported in the GOES catalogue. All of the few significant differences appear in the determination of flares of GOES intensity class below C2.0, which does not impact our study of the 32,380 C2+ flares. The evidence for incompleteness of the GOES catalogue for events of class smaller than C2 is explained in (Kossobokov et al., 2008).

RESULTS OF ANALYSIS

Figure 1 displays the inter-event intervals between successive C2+ flare events in the GOES catalogue, together with a moving 100-event average (black line, top part of the Figure). Also plotted (below) is the energy flux of GOES X-ray Class of C2+ flares. Both plots extend from 1975 through mid-2016 and are on logarithmic scales.

Figure 1 provides a vivid illustration of the evolution of flare distribution from 1975 to the present. The running averages of inter-event times (upper part, black line) and the energy of GOES X-ray Class C2+ flares (lower part, red line) appear to undergo quasi-periodic changes with extremely sharp onset and termination between two distinct states of intensive flare production during a solar cycle. The limits of the two states, which we call “active” and “quiet,” are quite distinctive, allowing their definition to be based on solar flares (Kossobokov et al., 2012). Both parts of the figure emphasize the very long “blank” interval of time that terminates Cycle 23 and starts Cycle 24.

The integrated flux of each C2+ flare is proportional to its peak burst intensity; hence this is also the case for the integrated daily flux, for which the sum of peak intensities is therefore a valid proxy (see Figure 1 of Kossobokov et al., 2008). Daily values of X-flux, $DX(t)$, have been computed by taking the sum of the peak intensities (energy proxies) of the C2+ flares belonging to day t . Figure 2 represents the series of daily numbers $DN(t)$ of GOES X-ray C2+ solar flares along with daily energy flux $DX(t)$ for the entire period available.

Naturally, both plots are quite correlated. Two features are outstanding in both: the long duration of Cycle 23 and the two-year interval with no energy between the end of Cycle 23 and the delayed start of Cycle 24.

Figure 3 shows the evolutions of running averages $\langle DX \rangle_{\Theta}(t)$ over intervals Θ respectively (from top to bottom) equal to 7, 21, 61, 183, and 365 days; the value $\langle DX \rangle_{\Theta}(t)$ is attributed to the last day t of the interval Θ . The singular shape of Cycle 23 is increasingly striking with increasing Θ : in Figure 3d and 3e, the first $\approx 70\%$ of the cycle display (on a logarithmic scale of energy flux proxy) linearly rising maxima with an ascending slope, whereas the minima are aligned along a descending slope for the latter part of the cycle. $\langle DX \rangle_{\Theta}(t)$ oscillates between these two lines, which take the shape of a bifurcation, with linearly increasing amplitude between the rising intermittent maxima and the decreasing intermittent minima. The shape of Cycle 23 is completely different from the smoother bimodal aspect of Cycle 22. On the other hand, one might note that Cycle 21 is somewhere in between (in terms of shape) the two successors, with a possibility that the same kind of bifurcation to intermittent regime occurs as in Cycle 23. This could then be a hint that odd and even cycles are different, i.e., a signature of the 22-year Hale magnetic cycle. With only three cycles, this conjecture remains unproven, yet Cycles 23 and 24 remain quite peculiar.

DISCUSSION

As already shown in (Kossobokov et al., 2012), we note the rather abrupt onset and termination of periods with short inter-event times and large and erratic energy fluxes. The characteristics of each cycle (21, 22 and 23) are similar, despite differing total durations. The “pseudo-periodicity” of the moving averages of inter-event times is shorter in the earlier two-thirds of the cycle and longer, with larger amplitude, in the final third of the time with short inter-event times (Figure 1, top part). This frequency drop occurs in 1983-1984 in Cycle 21, in 1992-1994 in Cycle 22 and in 2003-2005 in Cycle 23. Exponential decay of flare intensity starts respectively in 1983, 1993 and 2006 (Figure 1, bottom part). The characteristics of these phases occurring in the late part of the three previous cycles could be recognized even in the early part of Cycle 24, yet another feature that makes this cycle quite anomalous. Evidently, Cycle 24 is not over yet and we cannot provide a complete description as was given for Cycles 21 to 23 in Table 1 of (Kossobokov et al., 2012). However, some of the current estimates of solar activity characteristics

are already remarkable. Specifically, the number of flares in the observed part of Cycle 24 (either 43 in the X-class or 4614 in the C2+ class) is significantly smaller than that in the corresponding parts of the three previous cycles; the total X-flux of 0.051 Wm^{-2} is 2.4, 2.7, and 1.5 times less than in the first 7 years of Cycles 21, 22, and 23, respectively; the maximal flare has GOES class X6.9 (to be compared with X15, X20, and X28 in preceding cycles); the ratio between the number of X-flares and the number of C2 or larger flares is 0.009 (to be compared with 0.0158, 0.0164, and 0.0149). The change in this ratio may indicate that the flare-generating system in the on-going Cycle 24 has changed regime. Following Kossobokov et al., (2008), who note that the logarithm of this ratio is proportional to the slope of the Gutenberg-Richter plot for the distribution of flare energy, we may describe this regime change as going from “super-critical” in the previous three cycles to “under-critical” (Figure 4).

Systematic data on X-flux values are unfortunately not available prior to 1975. But they can be compared, in the period when they are available to a more traditional proxy of solar activity, i.e., sunspot number. The tabulated monthly values of the international sunspot numbers (SILSO World Data Center, 2016; SN_m_tot_V2.0.csv downloaded on August 4, 2016) along with the monthly number of C2 or larger flares are plotted in Figure 5. The excellent fit allows further comparison of the on-going Cycles 24 with solar activity in the past and extrapolation into the future.

Some abrupt regime changes may be more conspicuous with flares than with sunspot numbers (cf. Figures 1-4), but we have no X-flare intensity data prior to 1975. A comparison presented earlier by Kossobokov et al., (2012), placing side by side the sequences from Cycle 2 to 7 and 21 to 24 disclosed an outstanding similarity: Cycle 23 definitely looks like Cycle 4, leading one to compare the on-going Cycle 24 with Cycle 5. Figure 6a cross-compares the monthly sunspot numbers in all the 24 solar cycles from 1754 to the present (August 2016): the trajectory of the on-going Cycle 24 (white) is, definitely, in the lower part of the bundle of 24 cycles. It looks even more convincing when cycle trajectories of accumulated sunspot number are plotted in Figure 6b: after 7 years in progress, the trajectory of Cycle 24 flattens into a plateau that would end up with the third lowest total sunspot number, i.e., with only Cycles 5 and 6 (5,472 and 4,834) being lower, but Cycles 12 and 14 (7,663 and 7,395) somewhat above. It is notable that Cycle 5 follows Cycle 4 that has the largest sunspot total of 16,877. In the same way, Cycle 12 and the on-going Cycle 24 follow Cycles 8-11 and 17-23 that have high solar energy discharge, each characterized with a sunspot total number above 12,000 (about the median of

the 24 totals). The new, entirely revised data series of sunspot numbers (SILSO World Data Center, 2016) confirms that all three Cycles 24, 5, and 12 follow cycles with high solar activity defined as the sunspot total and are among the five smallest since the 18th century (cf. Le Mouél et al., 2010; Kossobokov et al., 2010).

Figure 7 compares sequences of the pairs of successive cycles associated with transition from high to low solar activity: the match is remarkable in both cases, i.e., Cycles 4-5 and 11-12 versus Cycles 23-24. The correlation of a hundred monthly sunspot numbers in the transitions either from Cycle 4 to 5 or from Cycle 11 to 12 versus from 23 to 24 is above 80% in both cases. The shapes of Cycles 5 and 12 are very similar to the on-going Cycle 24. Although the sequence of Cycles 23-24 definitely looks like 4-5, there is phase lag between the maxima of Cycles 4 and 23 of about 2 years that may require an explanation: Cycle 4 is longer than 23 and might be composed of the two cycles (Usoskin et al., 2009).

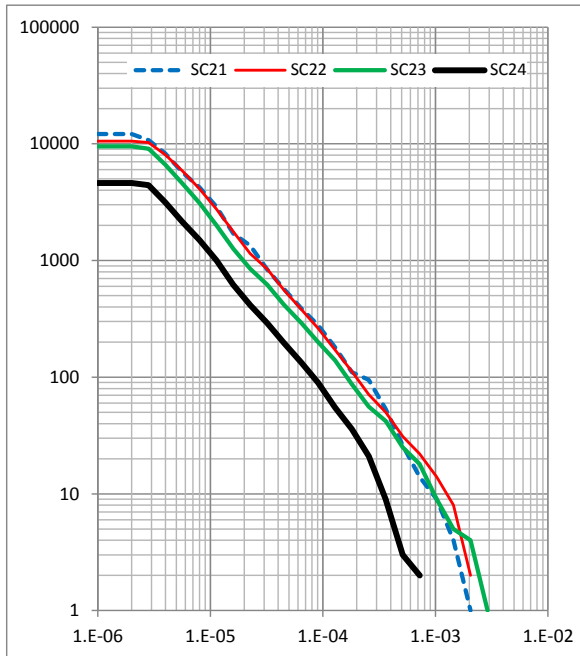


Figure 4. The Gutenberg-Richter plots of the number of flares with energy above given threshold in Cycles 21-24.

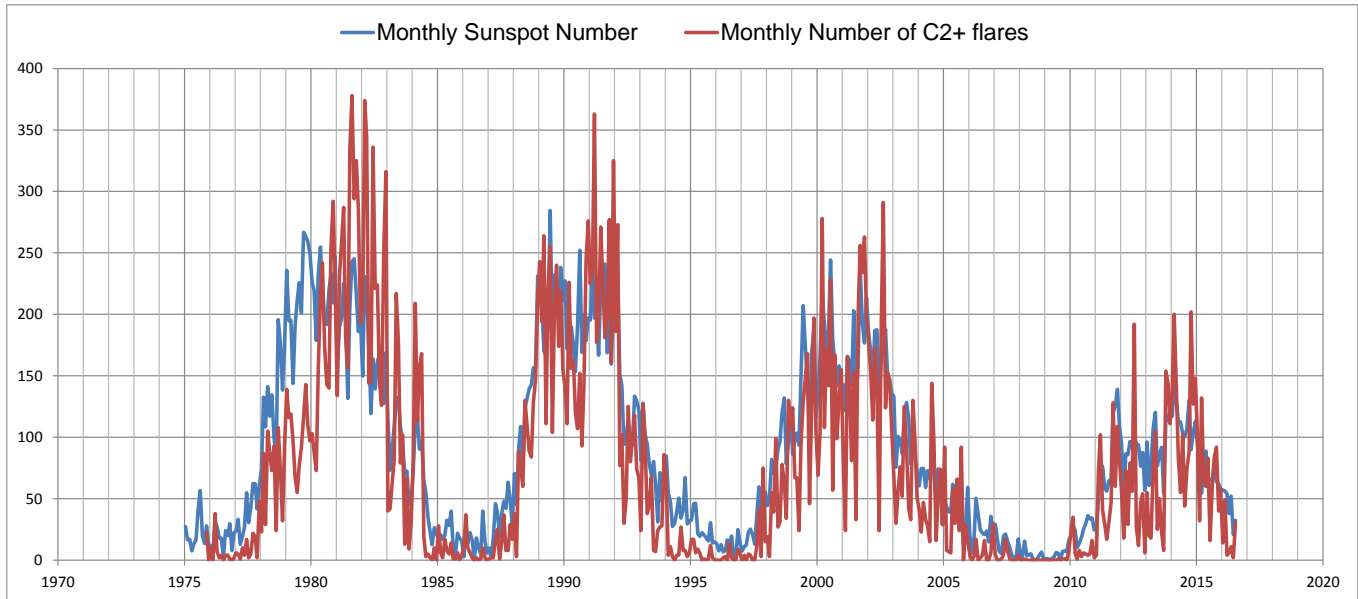


Figure 5. The monthly counts of sunspots (blue) and solar flares of the GOES C2 class or higher.

Complimentary Contributor Copy

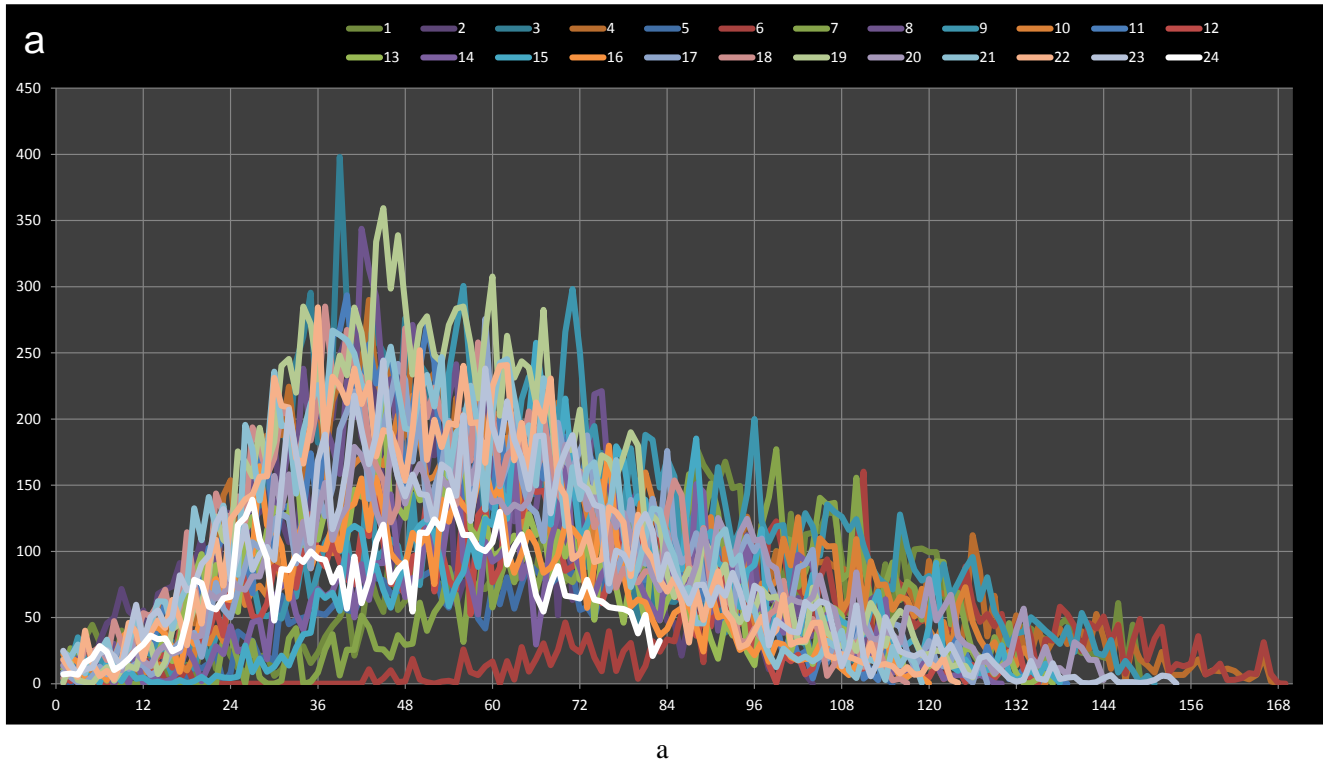


Figure 6. (Continued).

Complimentary Contributor Copy

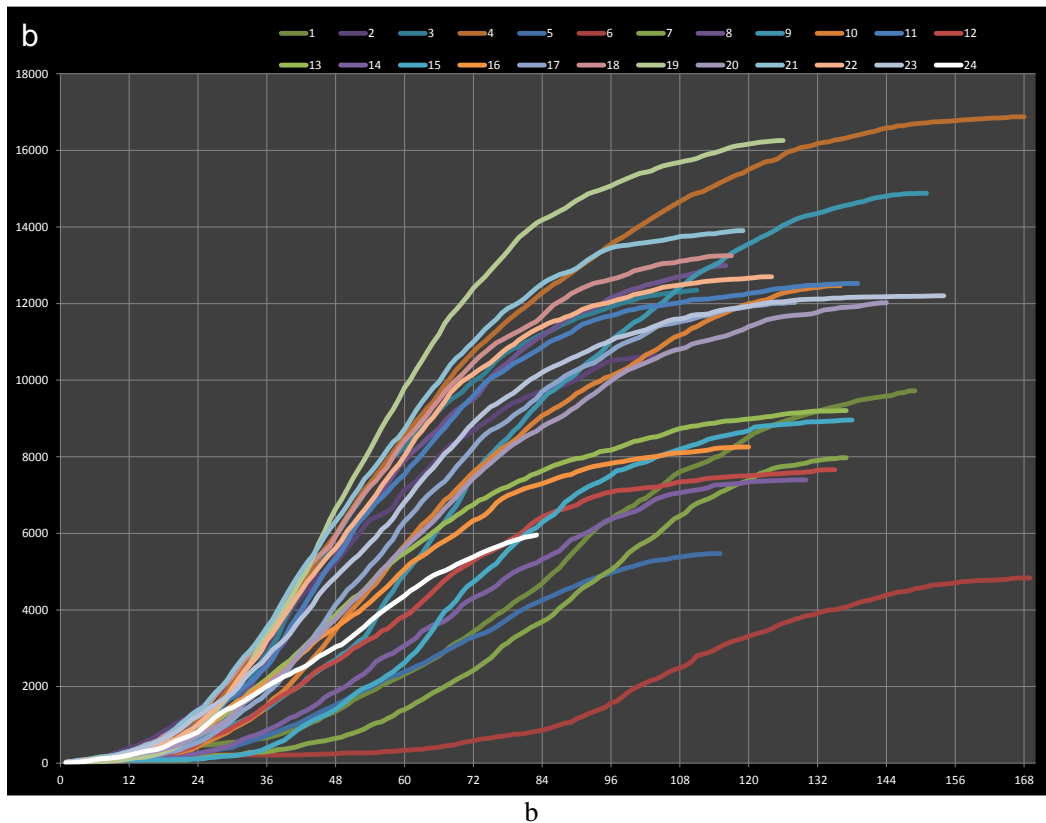


Figure 6. Sunspot Number in Cycles 1-24: monthly values (a) and accumulated from the beginning of a cycle (b).

Complimentary Contributor Copy

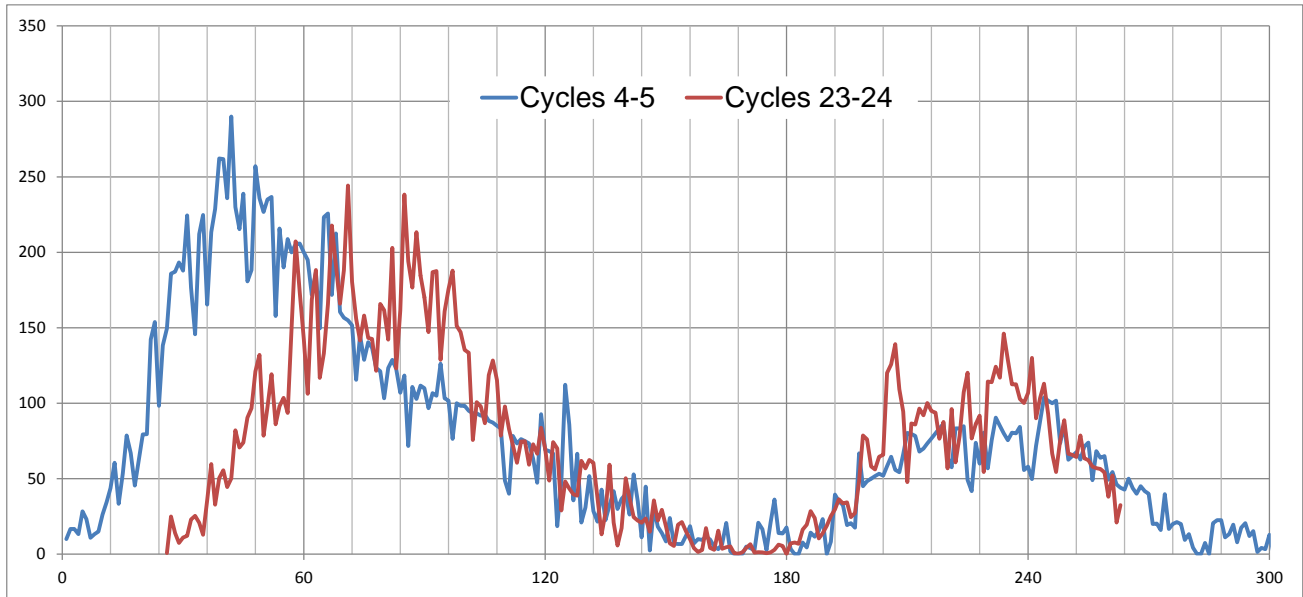


Figure 7. (Continued).

Complimentary Contributor Copy

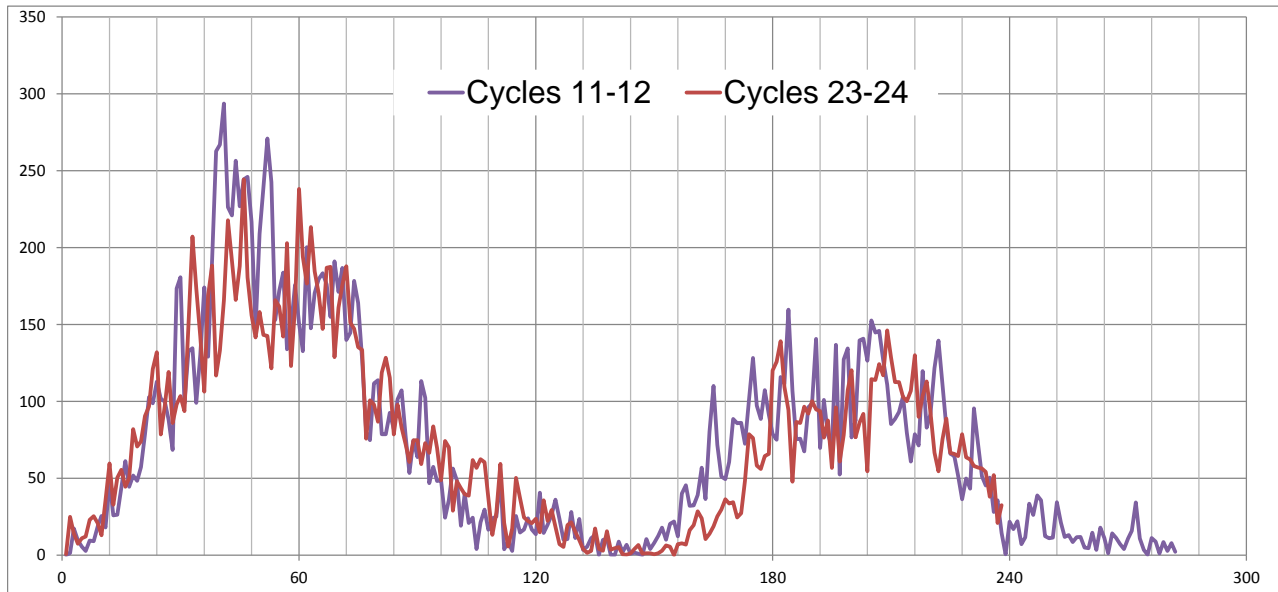


Figure 7. Monthly Sunspot Number in Cycles 4-5 (top) and 11-12 (bottom) with the superimposed on-going pair of Cycles 23-24.

Complimentary Contributor Copy

CONCLUSION

The duration of solar Cycle 24 remains a subject of debate, even though we already surpassed the two of its comparable monthly maxima in November 2011 (139.1) and February 2014 (146.1). If the fits of successions of solar cycles shown in Figure 7 have any “climatological” value, we may conclude that we are either in the Cycles 4-5 or 11-12 situation, the only with a succession since 1700 resembling what is known so far of Cycles 23-24. Then, inference from the solar activity decay observed in Figures 1-3 and 5-7 suggests a short duration of about 9-10 years for Cycle 24, as in low-activity cycles 5 and 12 (and also 6, 14). Moreover, the total energy of Cycle 24 may become the third lowest and the shortest of all instrumentally observed (Figure 6b). This would be supported by the unusual evolution of flare inter-event times and energy flux discussed in Figure 1. Some early predictions regarding Cycle 24 have already been rejected (Hathaway, 2008; Pesnel, 2008; others, e.g., based on the weak polar fields by Svalgaard et al., (2005) and/or derived from a non-linear coupling between sunspot maxima and aa-index minima by *Duhau* (2003) may still be vindicated.

Flare (or even sunspot) data are still too short to fully display the range of variability that can take place in a full solar cycle, and therefore one cannot yet predict accurately and reliably possibly non-linear trends in solar activity over the coming decade or, as we see here, even over a few years. Therefore, the plausible prediction of an approaching new Grand Solar Minimum and Little Ice Age in 2030-2040 (Mörner, 2015) might still be premature. Based on a detailed statistical analysis of solar flares, Kossobokov et al., (2008) have demonstrated a wide variety of impulsive energy release processes, none of which follows a common behavior nor could be attributed to a universal physical mechanism. Apparently and, in particular, at the times of a transition, we can only make an educated guess and keep correcting it through real-time monitoring of the phenomena.

Being based on rather short series (less than four full solar cycles for flares and about two dozen for monthly sunspot numbers) and a morphological similarity in evolution throughout a cycle, the present analysis and suggestion of a forecast are of course only tentative and still lack a sufficient physical background (they could be placed in the “precursor” class of Sello, 2001). However, the joint analyses of sunspots and flares and the representativeness of flares as solar activity markers gives some hope that the above analysis has some value and may stand the test of future observations.

Finally, the observed decline of solar activity in the on-going Cycle 24 similar to the fall in either Cycle 5 or 12 (Figure 7), and the flare signature in Figures 1 and 5 suggest a possible scenario of a further decline to the next solar minimum on transition to Cycle 25 in about 1-3 years. The prediction that we may be approaching a Grand Minimum as suggested by Duhau and de Jager (2008) and Russell et al., (2010) finds support in our analysis of flares and sunspots.

REFERENCES

- Aschwanden, M.J., *Physics of the Solar Corona: An Introduction with Problems and Solutions*, ISBN 3-540-30765-6, Springer, Berlin, 2006.
- Baranovski, A. L.; Clette, F.; Nollau V., *Ann. Geophys.*, 2008, 26, 231-241.
- Blanter, E.; Le Mouël, J.-L.; Shnirman, M.; Courtillot, V., *J. Atmos. Sol.-Terr. Phys.*, 2014, 117, 71-80.
- Clette, F.; Lefevre, L., *J. Space Weather Space Clim.*, 2012, 2.
- Duhau, S.; de Jager, C., *Solar Phys.*, 2008, 250, 1-15.
- Duhau, S., *Solar Phys.*, 2003, 213, 203-212.
- Hathaway, D., *Space Sci. Rev.*, 2008, 144, 401-412.
- Hathaway, D. H.; Rightmire, L., *Science*, 2010, 327, 1350.
- Hathaway, D. H.; Rightmire, L., *Astrophys. J.*, 2011, 729 (2), 80-89.
- Kossobokov, V.; Le Mouël, J. L.; Courtillot, V., *J. Atmos. Sol.-Terr. Phys.*, 2010, 72, 595-606.
- Kossobokov, V.; Le Mouël, J.-L.; Courtillot, V., *Solar Physics*, 2012, 276 (1-2), 383-394.
- Kossobokov, V. G.; Lepreti, F.; Carbone, V., *Pure Appl. Geophys.*, 2008, 165, 761-775.
- Le Mouël, J.-L.; Blanter, E.; Shnirman, M.; Courtillot, V., *J. Geophys. Res.*, 2012, 117, A09103.
- Le Mouël, J.-L.; Kossobokov, V.; Courtillot, V., *J. Atmos. Sol.-Terr. Phys.*, 2010, 72, 62-76.
- Mörner, N. *Natural Science*, 2015, 7, 510-518.
- Pesnell, W .D., *Sol. Phys.*, 2008, 252 (1), 209-220, 10.1007/s11207-008-9252-2.
- Russell, C. T.; Luhmann, J. G.; Jian, L. K., *Rev. Geophys.*, 2010, 48, RG2004.
- Scalgaard, L.; Cliver, E. W.; Kamide, Y., *Geophys. Res. Lett.*, 2005, 32, L01104-L01107.
- Sello, S., *Astron. Astrophys.*, 2001, 377, 312-320.

SILSO World Data Center (2016) The International Sunspot Number, International Sunspot Number Monthly Bulletin and online catalogue, 1749-2016, Royal Observatory of Belgium; <http://www.sidc.be/silso/>, last accessed 04 August 2016.

Usoskin, I. G.; Mursula, K.; Arlt, R.; Kovaltsov, G. A., *Astroph. J.*, 2009, 700 (2): L154.

Watanabe, K.; Masuda, S.; Segawa, T., *Solar Physics*, 2012, 279 (1), 317-322.

Chapter 5

LATEST NEWS ON ZEBRA PATTERNS IN THE SOLAR RADIO EMISSION

G. P. Chernov*

Key Laboratory of Solar Activity, National Astronomical Observatories,
Chinese Academy of Sciences, Beijing, China
Pushkov Institute of Terrestrial Magnetism, Ionosphere and Radio Wave
Propagation, Russian Academy of Sciences (IZMIRAN),
Troitsk, Moscow, Russia

ABSTRACT

The publications of the last three years concerning the study of the most intriguing fine structure in type IV solar radio bursts – zebra pattern (ZPs), are reviewed. The main attention is paid to new observations, irrespective of whether a paper includes detailed interpretation of an event or simply reports the beginning of operation of a new tool. The radiation mechanism of a ZP based on a double plasma resonance (DPR) remains the most widespread and standard, though ten alternative mechanisms have been offered. However, in a number of works difficulties with the explanation of a complex zebra are noted, especially in combination with fiber bursts and spikes. Therefore, several papers in which description of the radiation mechanism of a ZP on the DPR is improved are considered in more detail. In spite of lack of spatial information in the radio data we can still follow the flare dynamics using

* E-mail: gchernov@izmiran.ru.

SDO/AIA images in several EUV lines. In the discussion, the debatable questions regarding the comparison of mechanisms associated with DPR in terms of the model of interaction of plasma waves with whistlers are illuminated.

Keywords: Sun: flares, Sun: fine structure, Sun: microwave radiation, Sun: zebra pattern

1. INTRODUCTION

A zebra-pattern (ZP), in the form regular stripes in emission and absorption on the dynamic spectra of solar radio bursts, has already been studied for five solar cycles. Basic observational properties are presented in a number of reviews and monographs (Slottje, 1981; Kuijpers, 1975; Chernov, 2006, Chernov, 2011). Simultaneously with the observations, theoretical models were being developed, and currently more than ten mechanisms are offered. Most often in the literature the mechanism based on a double plasma resonance (DPR) is discussed (Kuijpers, 1975; Zheleznykov and Zlotnik, 1975a, b; Kuijpers (1980); Mollwo, 1983; 1988; Winglee and Dulk, 1986) which assumes that the upper hybrid frequency (ω_{UH}) in the solar corona becomes a multiple of the electron-cyclotron frequency:

$$\omega_{UH} = (\omega_{Pe}^2 + \omega_{Be}^2)^{1/2} = s\omega_{Be} \quad (1)$$

where ω_{Pe} is the electron plasma frequency, ω_{Be} is the electron cyclotron frequency, s is the integer harmonic number, and usually $\omega_{Be} \ll \omega_{Pe}$.

This mechanism experiences a number of difficulties with the explanation of the dynamics of zebra stripes and some thin effects (sharp changes of frequency drift, a large number of stripes, frequency splitting of stripes, superfine millisecond structure); therefore works on its improvement began to appear (Karlický et al., 2001; LaBelle et al., 2003; Kuznetsov and Tsap, 2007). The theory of LaBelle et al., 2003 is based on the emission of auroral choruses (magnetospheric bursts) via the escape of the Z mode captured by regular plasma density inhomogeneities. Kuznetsov and Tsap (2007) assumed that the velocity distribution function of hot electrons within the loss cone can be described by a power law with an exponent of 8–10. In this case, a fairly deep modulation can be achieved.

An alternative mechanism for ZP was proposed by Chernov (1976; 1990): the coalescence of plasma waves (l) with whistlers (w), $l + w \rightarrow t$ (Kuijpers, 1975), but a unified model in which the formation of ZP was attributed to the oblique propagation of whistlers, while the formation of stripes with a stable negative frequency drift (the fiber bursts) was explained by the ducted propagation of waves along a magnetic trap. This model explains occasionally observed transformation of the ZP stripes into fibers and vice versa.

However, a certain boom of new models proceeds. In several works the formation of ZP stripes is explained by radio wave diffraction on the heterogeneities in the corona (Laptukhov and Chernov, 2006; Barta and Karlicky, 2006), or by the interference of the direct and reflected from the heterogeneities rays (Ledenev, Yan, and Fu, 2006). In these cases the number of harmonics does not depend on the ratio of the plasma frequency to the gyrofrequency in the source. The formation of ZP stripes due to radio wave propagation through the coronal heterogeneities can be considered as the most natural mechanism of ZP.

It is important to note that the model based on whistlers successfully explains the zigzags of stripes and their splitting, and also the variations in the frequency drift of stripes synchronously with the spatial drift of the sources of radio emission (Chernov, 2006). Since each new phenomenon brings its uncommon parameters of fine structures, it is hard to handle the entire variety of parameters in the statistical systemizing (see, e.g., Tan et al., 2014). Below primary attention is given to the analysis of separate phenomena. Just such a situation stimulates many authors to elaborate on new mechanisms.

Only spatially-resolving observations could help to find out where the ZP stripes form (during the excitation of waves in the source or in the course of their further propagation).

During the last several years some new varieties of ZP have been recorded. In the present paper an attempt is made to estimate when the spatially-resolving observations can be the determining factor for the determination of the radio emission mechanism.

We also try to evaluate which model most adequately describes the new observational data and to find out where the ZP stripes form (during the excitation of waves in the source or in the course of their further propagation). Calculations show that the DPR-based mechanism fails to describe the generation of a large number of ZP stripes in any coronal plasma model (Chernov, 2010). Karlicky, Yasnov, 2015 also examined some other unsolved problems or difficulties in the DPR model in detail.

Here, it is shown that the new varieties of ZP succeed in explaining these phenomena within the framework of known mechanisms by taking into account the special features of plasma parameters and fast particles in the source. On the other hand, the formation of ZP stripes due to radio wave propagation through the coronal heterogeneities can be considered as the most natural mechanism of ZP. The mechanism related to the excitation of discrete eigenmodes of the periodically nonuniform plasma (Laptukhov and Chernov, 2006; 2009; 2012) can yield the observed number of harmonics. However, in that case, only the possibility of generating harmonics in a one-dimensional stationary problem is considered, i.e., the frequency dynamics of stripes is not analyzed.

During the last several years many new events with ZP have been recorded. Now, it is necessary to assess the possibility of their interpretation by taking into account all known models of ZPs, and our main goal is to review results of all recent publications about a ZP.

2. SEVERAL SPECIFIC CASES OF RECENT OBSERVATIONS

The measurement of positions and sizes of radio sources in the observations of the fine structure of solar radio bursts is the decisive factor for the selection of the radio emission mechanism. The identical parameters of the radio sources for zebra-structure and fiber bursts will confirm the common mechanism for both structures.

The new examined events show that the zebra-structure and fiber bursts can appear almost simultaneously or consecutively in the microwave, decimeter and meter wave bands.

2.1. FASR/FST Observations of ZP on December 14, 2006

The most cited and used model for ZP is mechanism at DPR, especially after the paper of Chen et al., (2011) where the authors allegedly confirm this mechanism using positional observation by the *Frequency-Agile Solar Radiotelescope Subsystem Testbed* (FASR, FST).

Observation. The authors presented the first interferometric observation of a radio burst with ZP in the decimeter range in the event on December 14, 2006 with simultaneous high spectral (≈ 1 MHz) and high time (20 ms) resolution (Figure 1[©] AAS. Reproduced with permission). By using *Owens*

Valley Solar Array (OVSA) to calibrate the FST, the source position of the zebra pattern can be located on the solar disk. The location of the ZP emission centroid was defined by the intersection of the three interferometric fringes of FST. The interferometric phase embodies the spatial information of the radiation source. They found a spatial drift of ZP source of $15.6'' \pm 6.5''$ from NE to SW on the solar disk, corresponding to a projected drift velocity of $(2.5 \pm 1.0) \cdot 10^9 \text{ cm s}^{-1}$ ($\approx 0.1c$). Unfortunately, Chen et al., (2011) considered averages of the phases “along” the on- and off-stripe positions (in time), to reveal the spatial distribution of the ZP source over frequency.

Comments to the interpretation. The authors conclude that the zebra burst is consistent with a DPR model, and they reject the alternative whistler model using an estimation of the tangent angle between whistler trajectory and solar surface (where a moving radio source was observed) by two method.

In this connection, it is necessary to note that the model based on whistlers was there mistakenly rejected. In the whistler model, when we estimate $V_{\text{gr}} = 2.5 \cdot 10^9 \text{ cm s}^{-1}$, that's value in the quasi-longitudinal propagation (along the magnetic trap, it is not V_{proj} as authors used). Actually $V_{\text{proj}} = V_{\text{gr}} \cos \alpha_1$, then for the whistler propagating to large angle to magnetic field ($\cos \alpha_1 \sim 0.1$) one could obtain the same value of $\tan \alpha_1$, as for $\tan \alpha_2$ (obtained using observed displacement of zebra stripes 1-6, and a height difference between them (see Figure 2)). Thus, there is no problem with the whistler model, in which the spatial drift of the radio source can be actually connected with the projection of the group velocity of whistlers. In such a case the assumed relation of the spatial drift of the radio source and frequency drift of stripes with a change of the speed of fast particles drops off.

The frequency drift of the of zebra- stripes changed the sign three times during one second (Figure 1), which highly improbably can be connected both with the change of the speeds of fast particles or with rapid changes in the magnetic field. The high speed of spatial drift of the zebra sources ($\sim 0.1c$) can be related with more high density gradient across the magnetic trap.

Then, Chen et al., (2011) used convenient idealised models for the plasma density and magnetic field depending exponentially upon height, which allows to receive the necessary ratio of scale heights for density and magnetic field $L_n/L_B = 4.4$. In the decimeter band an attempt on the determination of the displacement of the source during one zebra stripe in the event on December 14, 2006 with the aid of the system FASR did not succeed because of the insufficient time resolution, $\sim 20 \text{ ms}$, approximately in the same time interval.

The height of source was determined by the indirect method: by the extrapolation of the magnetic field above the active region in combination with an arbitrarily selected density model. Thus, it is impossible to determine unambiguously a suitable ZP model even in this event. Additional similar observations for more detailed consideration of the behavior of a radio source of one stripe of the ZP are required.

In the whistler model, radio sources of fiber bursts and ZP should be really moving, and the spatial drift of ZP stripes should change synchronously with the changes of frequency drift in the dynamical spectrum. It occurs in accordance with the change of the group velocity of whistlers as a result of the quasi-linear diffusion of the latter on fast particles (Chernov, 1990). In the DPR model the ZP source must be rather stationary.

2.2. Discussion of Several Case Studies

2.2.1. The September 17, 2002 Event

It is known that ZP is rarely observed at frequencies higher than 5 GHz.

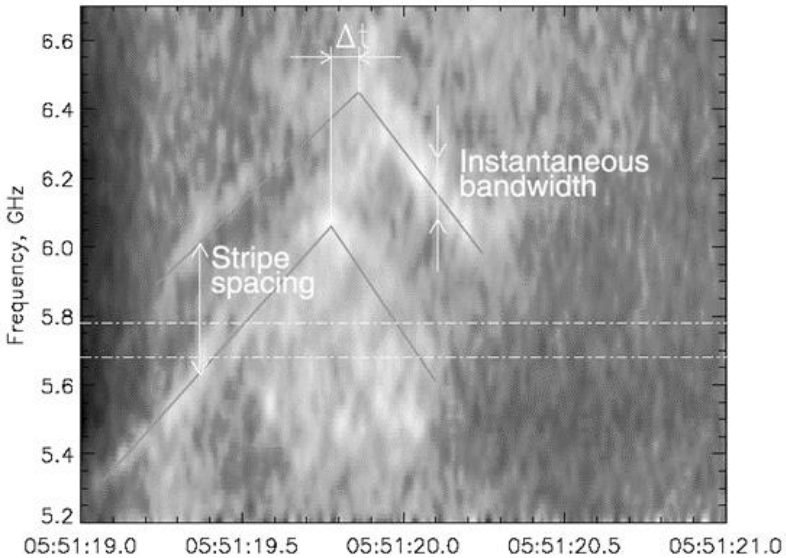


Figure 3. The dynamic spectrum of ZP observed on 17 September 2002. White means increased emission. The zebra stripes are indicated by the gray lines. The horizontal lines mark the boundaries of the SSRT receiver bands (from Altyntsev et al., 2011).

In the recent work of Altyntsev et al., (2011) the event on September 17, 2002 with a zebra-like pattern is discussed (Figure 3). Although it is difficult to classify this image as a typical ZP, Altyntsev et al., discuss it in terms of the DPR model, together with several other events, among which one was the May 29, 2003 event.

2.2.2. *The May 29, 2003 Event*

This event was also analyzed in more detail by Chernov et al., (2012a) (Figure 4). Dynamic spectra in Figure 4 demonstrate that all the emission comprises fine-structure details in the form of pulses (spikes). Their duration is limited to one pixel; i.e., it is at the limit of the 5 ms temporal resolution (rarely to two pixels, ~ 10 ms). They occupy the frequency band from ~ 70 to 100 MHz. Their band and duration might be below the resolution limit. The continual background burst also exhibits the spike structure. Groups of spikes create various fine-structure forms: fast and slow-drifting fibers. The brightest (most intense) ones form different zebra stripes.

The spatial locations of the radio bursts were obtained by the Siberian Solar Radio Telescope (SSRT) (5.7 GHz) and *Nobeyama Radioheliograph* (NoRH) (17 GHz) (Figure 5).

This event may be used as an example demonstrating the possible difficulties that the DPR mechanism faces for explaining the zebra-structure with sporadic stripes. Originally, the DPR mechanism was developed under the assumption that there are always DPR levels in the source, and only the presence of fast particles with a loss-cone or ring (DGH) velocity distribution provides the excitation of the regular zebra structure of different modulation depths (depending on the particle energy spectrum, Kuznetsov and Tsap (2007)). The presence of such particles may be considered obvious, so that the absence of zebra-structure at the beginning of the burst suggests there are no DPR levels.

DPR levels cannot quickly appear and disappear in the corona. Processes of emergence of new magnetic fluxes and formation of new loops are very slow. Changes in height scales of density and magnetic fields may be associated only with flare ejections and shocks. With the ejection velocity taken as the Alfvén velocity (≈ 1000 km s⁻¹), the DPR levels (taking into account the magnetic field frozen-in condition) may shift the green flare loop (in Figure 5) by half of its length with sizes of $\sim 10''$ for approximately 7 s. This time exceeds the lifetime of zebra-structure stripes by an order of magnitude. The sporadic nature of ZS stripes, the wave-like drift of two stripes (IV in Figure 4), their splitting, and the presence of isolated fibers with forward and

reverse drifts rule out the existence of any regular DPR levels. Moreover, the validity of the DPR conditions in thin flare loops along which the density and magnetic field strength vary only slightly is in doubt (Aschwanden 2004).

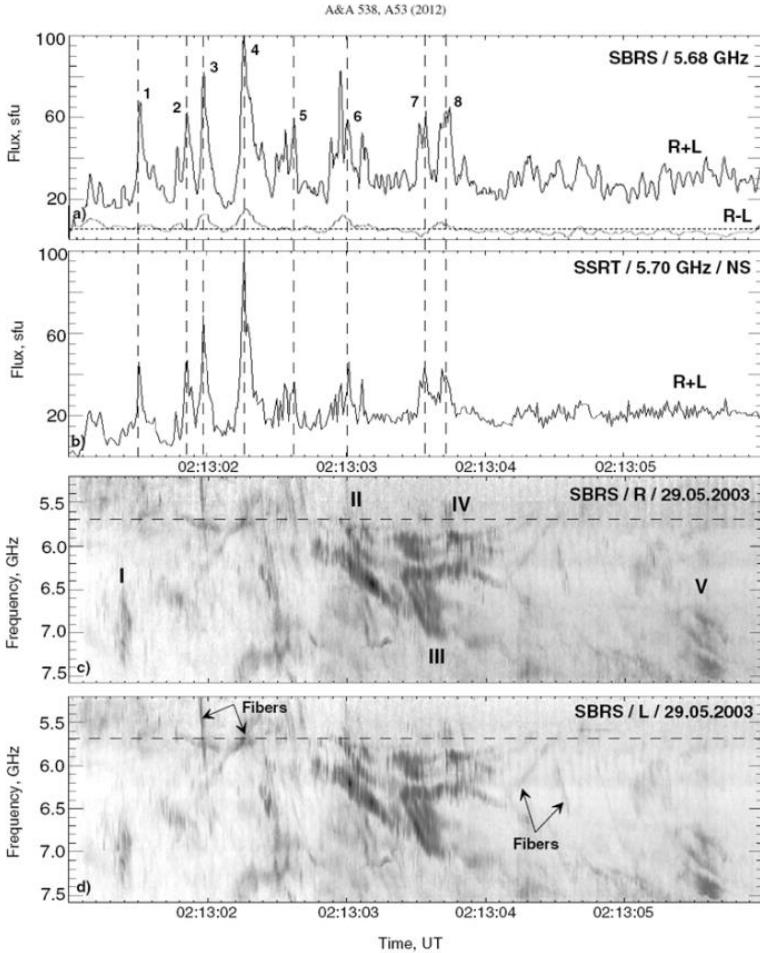


Figure 4. Comparison of the time profiles recorded at Solar Broadband Radio Spectrometer (SBRS) a) and SSRT b) and the dynamic spectra (c), (d) registered by the SBRS spectro-polarimeter. The dark details correspond to the increased emission. The horizontal dashed line c) denotes the SSRT receiving frequency at 5.7 GHz. The calibration was performed using the SSRT-registered background burst. Arabic numerals in panels (a), (b), dashed vertical lines) mark the maximum moments of subsecond pulses recorded by the fibers (from Chernov et al., 2012a).

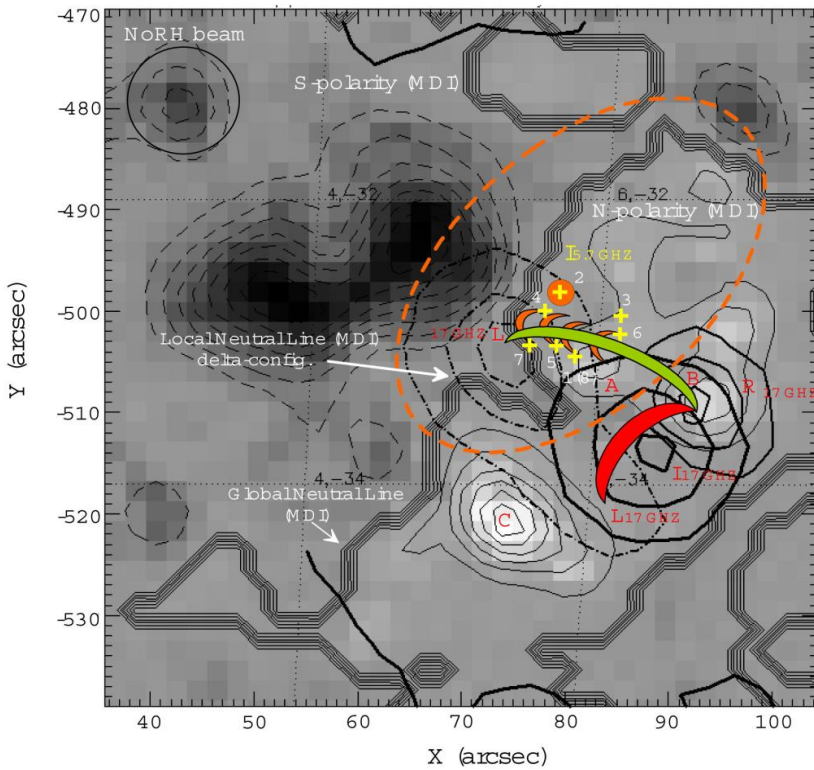


Figure 5. The positions of radio sources at 5.7 GHz (SSRT) and 17 GHz (NoRH) superimposed on the MDI magnetogram. The orange dashed line indicates the position of the left polarized local source at 5.7 GHz at 02:17:54.8 UT. The dash-and-dot line shows the position of the left polarized background source of the burst at 17 GHz (extended southwestward) at 02:13:00 UT. The straight yellow crosses are the positions of spike sources 1–8 corresponding ones in Figure 4 (from Chernov et al., 2012a).

At the same time, all these effects can be naturally explained by the joint model of zebra-structure and fibers when plasma waves interact with whistlers (Chernov 2006). Then, estimations carried out in Chernov et al., (2012a) show that the propagation time of whistlers along flare loops corresponds to the life time of zebra stripes.

The sporadic nature of the fine structure suggests multiple pulsating acceleration of fast particles. However, the superfine spike structure is not necessarily determined by a pulsating acceleration as discussed in Kuznetsov (2007). It is much more probable that the spike nature of the entire emission is

formed by a pulsating mechanism of emission. In this model ZP is generated by periodic whistler packets filling a magnetic trap. But whistlers should occupy the entire radio source and propagate in different directions. Spikes might therefore be related to the pulsating interaction of whistlers with ion-sound waves and subsequent coalescence with plasma waves. This mechanism is discussed in Chernov et al., (2001). In the microwave range it may be more effective because near the reconnection region the presence of nonisothermic plasma ($T_e \gg T_i$) is much more likely as a condition for ion-sound excitation.

2.2.3. The event on February 15, 2011

Tan et al., (2012) analyzed ZP in the first X- class flare in the solar cycle 24, on February 15, 2011. Figure 1 of this work depicts the temporary profiles of the fluxes of radio emission in a number of frequencies, and the profiles of soft X-ray GOES 4 and 8. This X-ray flare began approximately 15 min earlier than radio bursts. The temperature of plasma in the X-ray sources was very high, about 20 MK. Three ZS stripes in the microwave range appeared first at frequencies 6.4 – 7.0 GHz in the left-handed polarization during the rising phase of the first flare brightening (ZP1, Figure 6). Then, at ~11 min ZP2 appeared during the decrease of the second brightening in the 2.6 – 2.75 GHz band (shown here in Figure 7) also in the left-handed polarization. Further, still at ~9.5 min during the decrease of the third brightening in the decimeter band 1035 – 1050 MHz, ZP3 was detected by SBRS/Yunnan (see Figure 8) but this time with the moderate right-handed polarization. Thus, in the prolonged event (~45 min) the ZS appeared only three times for 3-second intervals. By scrutinizing the current prevalent theoretical models of ZP structure generations and comparing their estimated magnetic field strengths in the corresponding source regions, Tan et al., (2012) suggest that the DPR model is the most probable one for explaining the formation of microwave ZPs.

Chernov et al., (2015) focus attention on a number of the aspects that not examined in the work of Tan et al., (2012). In particular, zebra stripes were observed also in the meter band, for example according to the Culgoora spectrograph at 200 - 300 MHz (see Figure 10 in Chernov et al., 2015). The type II burst is also visible, which began near 01:50 UT. The beginning of the corresponding CME was approximately at 01:30 UT, that coincides with the beginning of the X-ray burst. Therefore the type II burst was most likely caused by a piston shock wave.

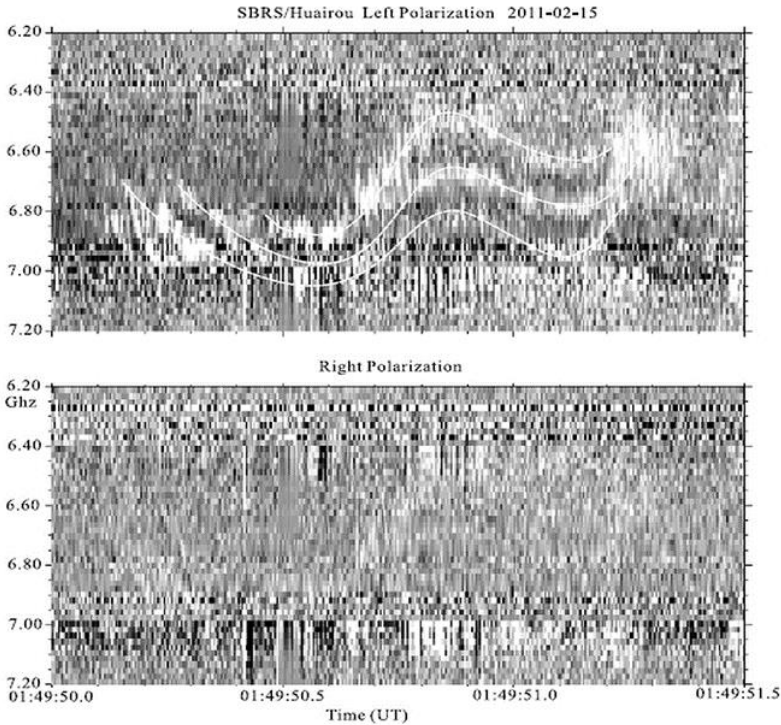


Figure 6. Three ZS stripes in the 6.4 – 7.0 GHz band in the left polarization channel of SBR/Suairou at rising phase of the first flare brightening (ZP1 in Tan et al., 2012). The white dashed curves outshine the zebra stripes.

In Figure 7 we see fast pulsations in the 2.7-2.9 GHz band, from high frequencies of ZP. After approximately 2.5 min. specifically, in this range fiber bursts appeared with the intermediate frequency drift df/dt of ≈ 350 MHz s^{-1} , approximately with the same period (see Figure 11 of Chernov et al., 2015). Subsequently, during five minutes the initial frequencies of fibers increased approximately on 100 MHz together with a new series of pulsations with an irregular period.

If we connect the onsets of three time intervals in which ZP1, ZP2 and ZP3 occur with the appropriate flare brightenings and the ejections in the SDO/AIA 171 Å images, then they lie down in the different sections of AR. In Figure 12 of Chernov et al., 2015 it is shown that sources of ZP1 and ZP2 lie down on the loops above the preceding spot of northern magnetic polarity, and ZP3 above the tailed spot of southern polarity. Therefore in all three cases the emission can be connected with the ordinary wave.

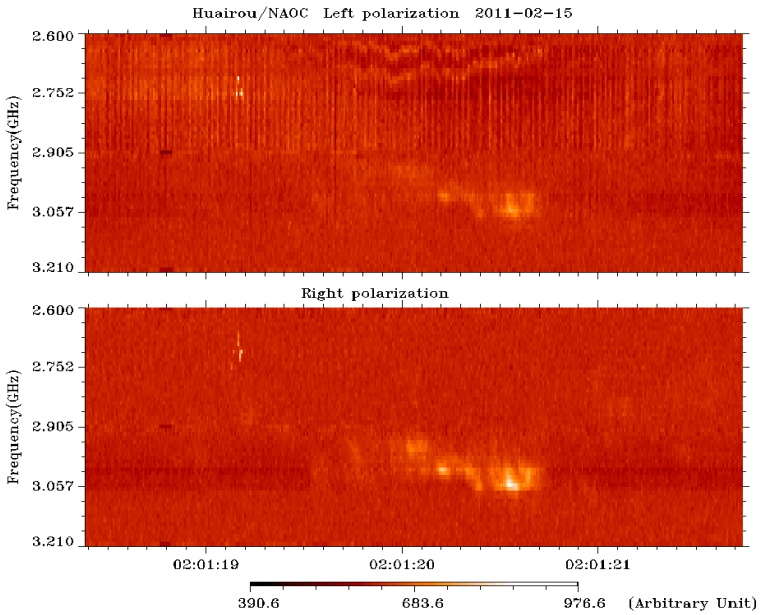


Figure 7. Two stripes of ZS superimposed on fast pulsations with the period of ~ 30 ms.

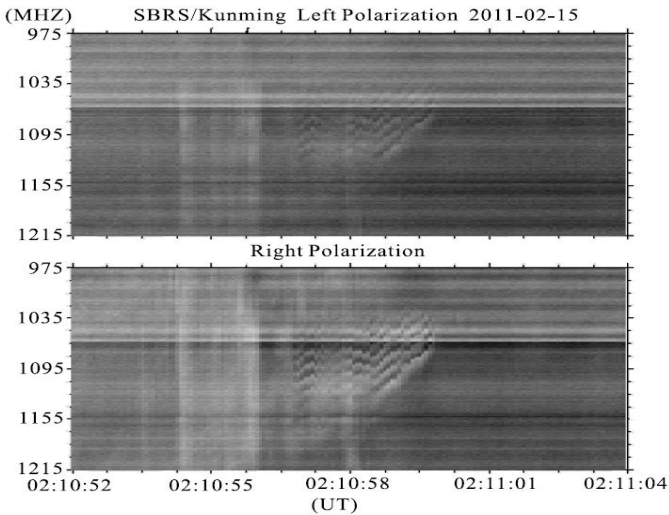


Figure 8. Zebra- structure in the decimeter band 1.04 – 1.13 GHz in right polarization detected by the SBRS/Yunnan (Tan et al., 2012).

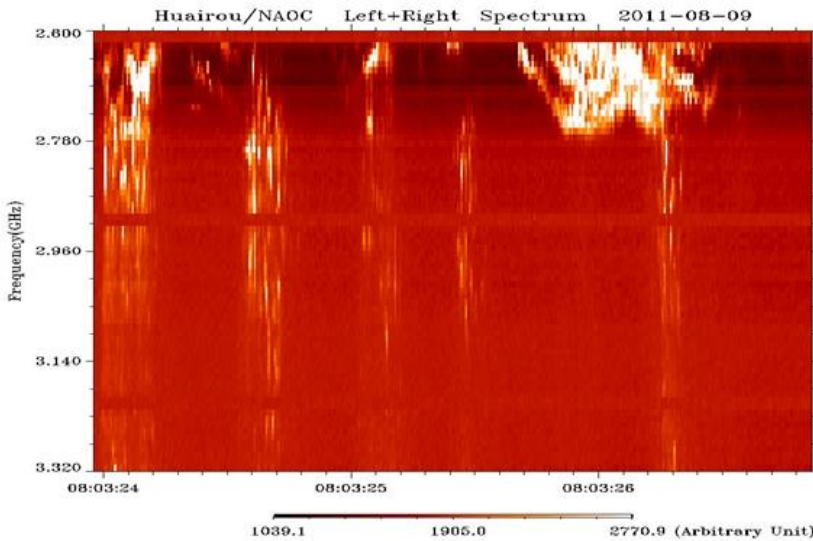


Figure 9. Three stripes of ZS in the LF edge of pulsations with millisecond superfine structure (from Tan and Tan (2012)).

2.2.4. Fast Pulsation in the Event On August 9, 2011

Tan and Tan (2012) analyze peculiar microwave quasi-periodic pulsations (QPP) accompanying a hard X-ray (HXR) QPP of about 20 s duration observed just before the maximum of an X6.9 solar flare on August 9, 2011 at 2.60–3.80 GHz by the Chinese Solar Broadband Radio Spectrometer (SBR/S/Huairou). The most interesting aspect is that the microwave QPP consists of millisecond timescale superfine structures and zebra stripes in the low frequency part of QPP (Figure 9). Each microwave QPP pulse is made up of clusters of millisecond spike bursts or narrow-band type III bursts. The physical analysis indicates that the energetic electrons accelerating from a large-scale highly dynamic magnetic reconnecting current sheet above the flaring loop propagate downward, impact the flaring plasma loop, and produce HXR bursts. The tearing-mode (TM) oscillations in the current sheet modulate HXR emission and generate HXR QPP; the energetic electrons propagating downward produce Langmuir turbulence and plasma waves, resulting in plasma emission. The modulation of the plasma emission by the TM oscillation in the current-carrying plasma loop may generate microwave QPP. The TM instability produces magnetic islands in the loop. Each X-point is then a small reconnection site where the electrons are accelerated. These accelerated electrons impact the ambient plasma and trigger the millisecond

spike clusters or a group of type III bursts. Possibly, each millisecond spike burst or type III burst is one of the elementary bursts (EBs). A large number of such EB clusters form an intense flaring microwave burst. This original interpretation is illustrated by the sketch in Figure 10.

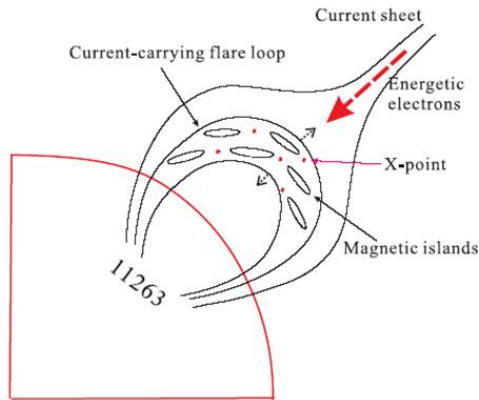


Figure 10. Sketch showing the processes of electron acceleration above and in the flare loop, propagation, and the formation and distribution of magnetic islands in the current-carrying flare loop. It is possible only to add that a source of ZP is probably located at the top of current-carrying flare loop (from Tan and Tan (2012)).

2.2.5. The Decay Phase of the Event on December 1, 2004

Huang and Tan (2012) made a detailed analysis of microwave FSs during the decay phase of the M1.1 flare on December 1, 2004, using the microwave observations with SBRs/Huairou, ranging from 1.10 to 7.60 GHz and the HXR observations from RHESSI.

In the microwave spectra, Huang and Tan (2012) have identified stripe-like bursts such as lace bursts, fiber structures, zebra patterns (ZPs), and quasi-periodic pulsations. They also have detected short narrowband bursts such as dots, type III, and spikes. The lace bursts had rarely been reported, but in this event they are observed to occur frequently in the decay phase of the flare. The similarity between the 25 and 50 keV HXR light curves and microwave time profiles taken at 1.10–1.34 GHz suggests that these microwave FSs are related to the properties of electron acceleration. The electron speed inferred from the frequency drift rates in short narrowband bursts is in the range of $0.13c$ – $0.53c$ (formula 8 in Huang and Tan (2012)) and the corresponding energy is about 10–85 keV, which is close to the energy of HXR-emitting electrons. From the Alfvén soliton model of fiber structures (Bernold, T. E., and Treumann, R. A.

1983), the DPR model of ZPs, and the Bernstein model of the lace bursts, the authors derived a similar magnetic field strength in the range of 60–70 G. Additionally, the physical conditions of the source regions such as height, width, and velocity of the source are estimated.

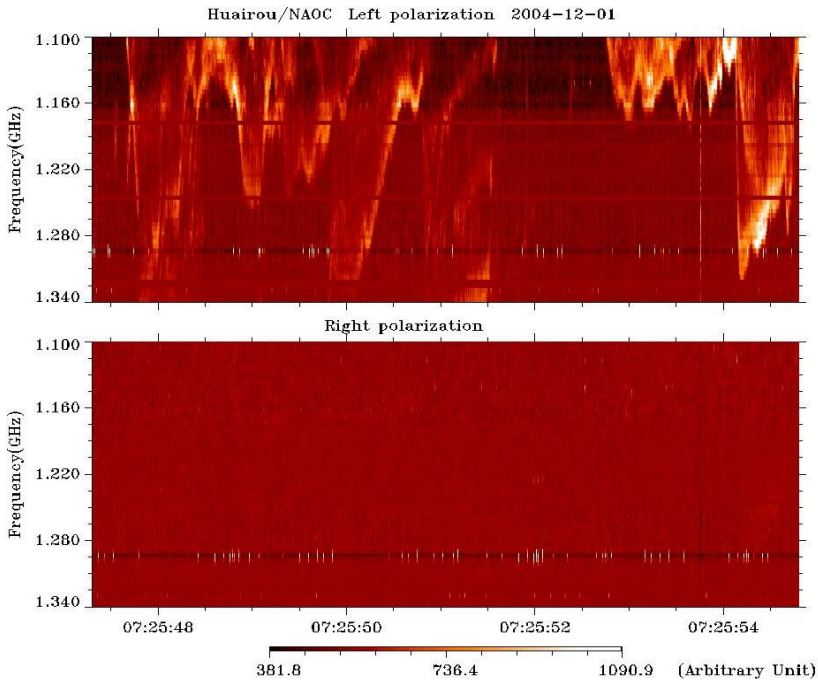


Figure 11. Dynamic spectrum of lace bursts in decay phase of the M1.1 flare event observed at SBRS/Huairou at 07:25:48–07:25:55 UT on 2004 December 1.

The lace bursts are the most obvious fine structure in the decay phase of the M1.1 flare on December 1, 2004 (Figure 11). According to Karlicky et al., (2001), the lace bursts may be generated by DPR mechanism in turbulent plasmas associated with the plasma outflows from the magnetic reconnection sites. In this case, naturally, the authors in no way can explain the sharp jumps of frequency drift, since actually the precise mechanism is unknown (turbulence in DPR model). Nevertheless, the authors determine the magnetic field strength, using the Bernstein model. And it is no matter how strange, they obtained the same strength as well as obtained with fibers bursts and ZP. At least, such an agreement does not prove the correctness of their selection of the Bernstein model.

2.2.6. Quasi-Periodic Wiggles of ZP Stripes

In Yu et al., (2013) quasi-periodic wiggles of microwave zebra pattern (ZP) structures with periods ranging from about 0.5 s to 1.5 s are found in an X-class solar flare on December 13, 2006 at the 2.6–3.8 GHz with the Chinese Solar Broadband Radio Spectrometer (SBRS/Huairou). Periodogram and correlation analysis show that the wiggles have two or three statistically significant periodicities and are almost in phase in different stripes corresponding to different frequencies (Figure 12). The Alfvén speed estimated from the ZP structures is about 700 km s^{-1} . They have found the spatial size of the wave-guiding plasma structure to be about 1 Mm with a detected period of about 1 s. This suggests that the ZP wiggles can be associated with the fast magneto-acoustic oscillations in the active flaring region. The lack of a significant phase shift between wiggles of different stripes suggests that the ZP wiggles are caused by a standing sausage oscillation.

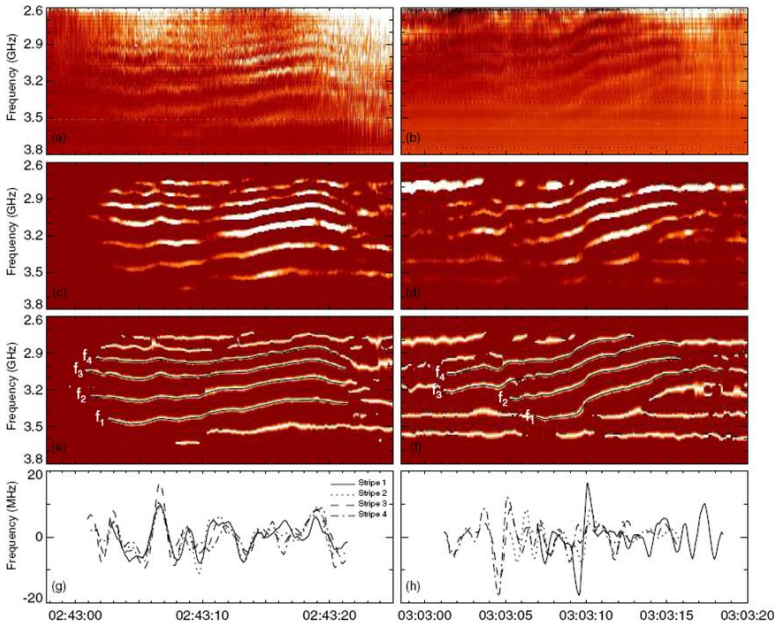


Figure 12. Zebra pattern structures on 2006 December 13 observed by SBRS/Huairou at 2.6–3.8 GHz and the illustration of the processes of extracting the zebra pattern stripes. Panels (a, b): raw spectrograms at 2.6–3.8 GHz on LHCP; (c, d) high contrast images; (e, f) rescaled images with the extracted stripes superposed; and (g, h) detrended selected stripes frequency f_N (from Yu et al., (2013)).

2.2.7. *Statistics*

A comprehensive statistical study would certainly help us to understand the formation mechanism, which is not exactly clear now. Tan et al., (2014a) present such a comprehensive statistical analysis of a big sample with 202 ZP events collected from observations at the Chinese Solar Broadband Radio Spectrometer at Huairou and the Ondřejov Radio spectrograph in the Czech Republic at frequencies of 1.00–7.60 GHz from 2000 to 2013. Tan et al., (2014a) attempted to carry out statistical comparison of models among which the following were chosen:

- Bernstein wave (BW) model (Zheleznyakov and Zlotnik, 1975a);
- Whistler wave (WW) model (Chernov, 2006);
- Double plasma resonance (DPR) model (Zheleznyakov and Zlotnik, 1975a);
- Propagation through coronal inhomogeneities or interference model (Laptuhov and Chernov, 2006; 2012; Bárta, M. and Karlický, M. 2006).

After investigating the parametric properties of ZPs, such as the occurrence in the flare phase, frequency range, polarization degree, duration, etc., they have found that the variation of zebra stripe frequency separation with respect to frequency is the best indicator for a physical classification of ZPs. Microwave ZPs can be classified into three types: equidistant ZPs, variable-distant ZPs, and growing-distant ZPs, (Figure 13) possibly corresponding to mechanisms of the Bernstein wave model, whistler wave model, and DPR model, respectively. This statistical classification may help us to clarify the controversies between the various existing theoretical models, and understand the physical processes in the source regions.

However, a problem remains, connected, first of all, with the ambiguous determination of frequency separation in the observations. Secondly, in the whistler model the frequency separation also increases with the frequency in accordance with increasing of the cyclotron frequency with plasma frequency.

2.2.8. *The Ratio L_N/L_B .*

Yu, Yan, and Tan (2012) investigated the variations of 74 microwave ZP structures observed by the Chinese Solar Broadband Radio Spectrometer (SBR/S/Huairou) at 2.6–3.8 GHz in nine solar flares.

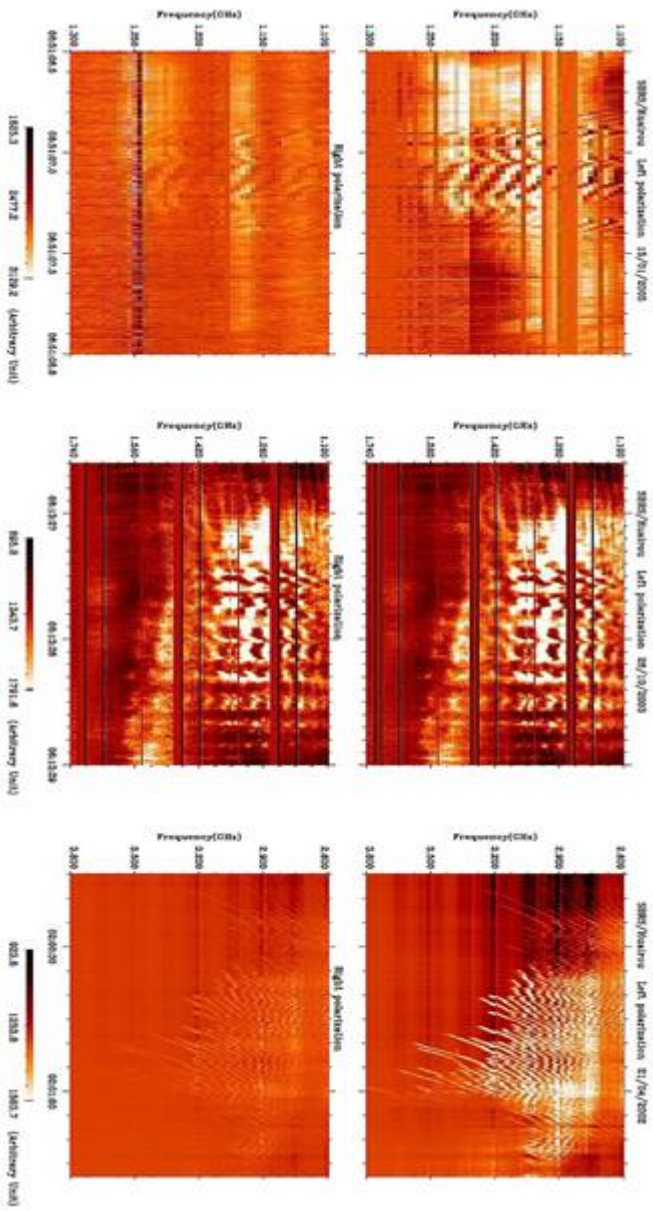


Figure 13. Spectrograms with different ZP separation; (left)- typical equidistant with constant separation (BM), (middle)- variable-distant ZP (WW) with varying separation; and (right)- growing-distant with rising separation (DPR).

They used the DPR model with exponentially decrease of both the magnetic field strength (B) and the plasma density (n_e) with height (h) along the flux tube in the corona.

They found that the ratio between the plasma density scale height L_N and the magnetic field scale height L_B in the emission sources displays a tendency to decrease during the flaring processes. The ratio L_N/L_B is about 3–5 before the maximum of flares. It decreases to about 2 after the maximum. The variation of L_N/L_B during the flaring process is most likely due to topological changes of the magnetic field in the flaring source region, and the stepwise decrease of L_N/L_B possibly reflects the magnetic field relaxation relative to the plasma density when the flaring energy is released.

The ratio L_N/L_B plays a significant role in the DPR model (Zheleznyakov & Zlotnik 1975). However, the absolute values of L_N and L_B are even more important. The authors discuss a contradiction with the DPR model in April 21, 2002 event. Their estimations of the ratio $L_N/L_B = 2$, magnetic field $B = 19.5$ G, and plasma $\beta \approx 1.4$ are a major obstacle for the DPR model to produce thirty four ZP stripes simultaneously in the 2.6–3.8 GHz band in this event. The authors proposed the whistler model to be responsible for the formation of the multi-striped ZP structures in this event, as the ratio L_N/L_B is not an important parameter in this model, and the absolute value of magnetic field B of ≈ 71.5 G is more important.

2.2.9. ZP during Magnetic Reconnection (Chernov et al., 2015)

Even without spatial resolution in radioband we have a great opportunity to follow the dynamics of flare processes using SDO/AIA images in several EUV lines (Chernov et al., 2015). The event on February 24, 2011 is remarkable, as the zebra-structure at frequencies of 2.6 – 3.8 GHz was not polarized and it appeared during the magnetic reconnection observed by SDO/AIA 171 Å in this limb flare (See Figures 2a and 6 in Chernov et al., 2015).

2.2.10. Rope-Like Fibers in the Event on February 12, 2010

Solar radio emission records received at the IZMIRAN spectrograph (25–270 MHz) during the solar flare event on February 12, 2010 are analyzed by Chernov et al. (2014b). Different fine structures were observed in three large groups of type III bursts against a low continuum. According to the data obtained with the Nançay radioheliograph, sources of all three groups of bursts were located in one active region, 11046, and their emissions were accompanied by soft X-ray bursts (GOES satellite): C7.9 at 07:21 UT, B9.6 at

09:40 UT, and M8.3 at 11:25 UT. After the first group of bursts, classical fiber bursts were observed in combination with reverse-drift fiber bursts with unusual arc drift. After the third (the most powerful) group, stable second-duration pulsations and slow drift fiber bursts were observed, the instantaneous frequency bands of which were an order of magnitude larger than the frequency band of classical fiber bursts, and the frequency drift was several times lower. More complex fiber bursts were observed in the weakest group in the time interval 09:40:39–09:42:00 UT (Figure 14). They were narrow-band (~0.5 MHz) fiber bursts, periodically recurring in a narrow frequency band (5–6 MHz) during several seconds (“rope-like” fibers). The presence of many chaotically drifting ensembles of fibers, crossing and superimposing on one another, is a feature of this event. It is assumed that occurrence of these structures can be connected with the existence of many small shock fronts behind the leading edge of a coronal mass ejection.

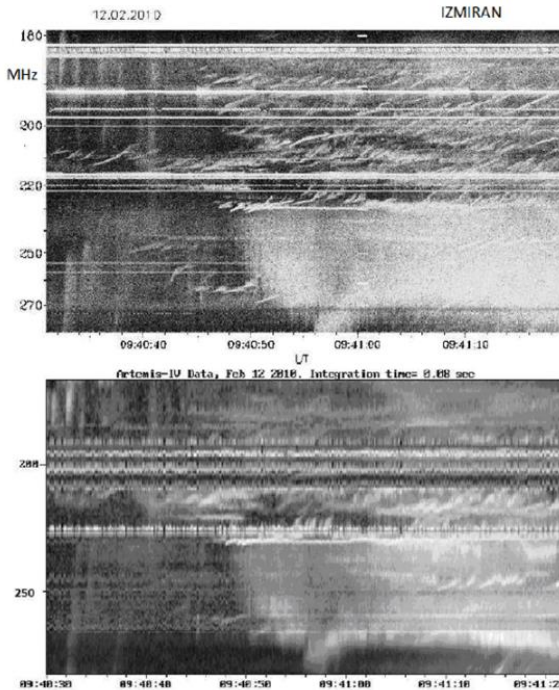


Figure 14. Segments of dynamics spectra with fiber ropes in the 180–280 MHz range measured simultaneously on IZMIRAN and ARTEMIS_IV (Greece) spectrographs on February 12, 2010 (from Chernov et al., 2014b).

2.2.11. Flare Evolution and Polarization Changes in ZP in the Event April 11, 2013

In a M6.5 flare on April 11, 2013, solar radio spectral fine structures were observed for the first time simultaneously by several radio instruments at four different observatories. (Chernov et al., 2016). The fine structures include microwave zebra patterns, fast pulsations, and fibers. They were observed during the flare brightening located at the tops of a loop arcade as shown by SDO/AIA images.

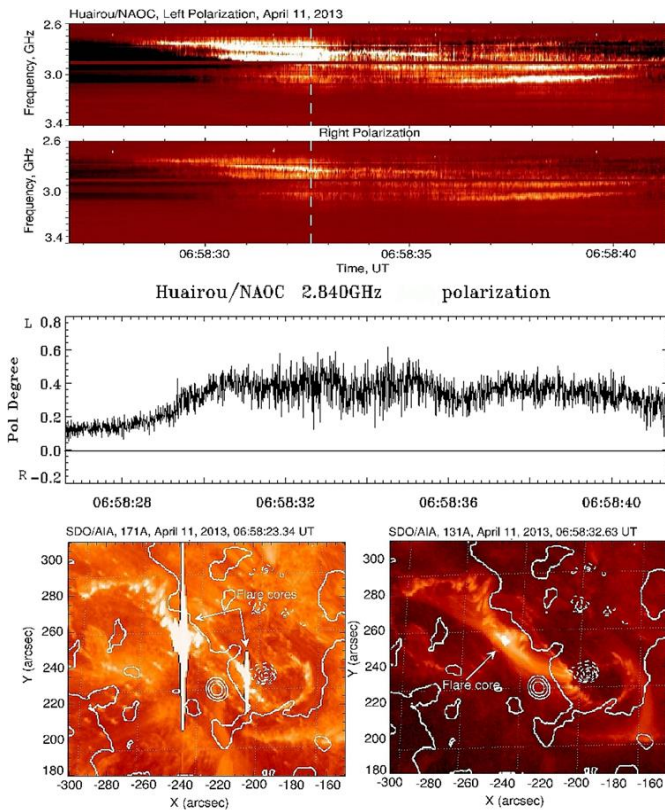


Figure 15. Strong ZP at the beginning of the event that occurred on 11 April 2013 as registered by the SBR/S/Huairou, discussed in Tan et al., (2014). Middle panel: polarization profile at 2.84 GHz. Bottom panel: two frames taking by SDO/AIA 171 Å (left) and 131 Å (right) movies. The dotted vertical line in the spectrum shows the instant of time displayed in the right frame at 131 Å. Moderate left polarization can be explained by a hard flare core in the left flare ribbon with the North magnetic polarity (ordinary wave mode) (Chernov et al., 2016).

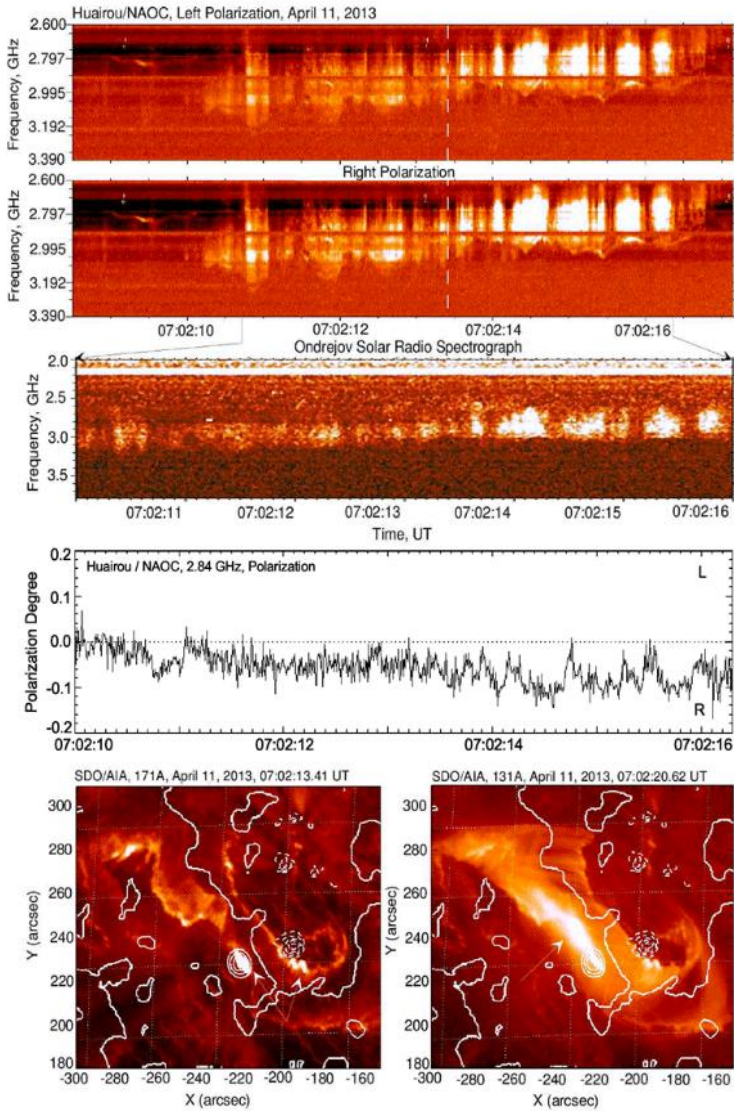


Figure 16. Fast pulsations during 8 sec registered by the SBRS/Huairou in the 11 April 2013 event. Spectra of pulsations and ZP coincide in the observations made by the Huairou and Ondřejov observatories. The polarization profile at 2.84 GHz of SBRS/Huairou shows weak right-handed polarization of $8 \pm 4\%$. Bottom: two frames taken with SDO/AIA at 171Å (left) and 131Å (right) movies. The dotted vertical line in the spectrum shows the instant of time displayed in the left frame in 171Å line (Chernov et al., 2016).

At the beginning of the flare impulsive phase, a strong narrowband ZP burst occurred with a moderate left-handed circular polarization (Figure 15, see also Tan et al., 2014b)). Then a series of pulsations and ZPs were observed almost in an unpolarized emission. After 07:00 UT a ZP appeared with a moderate right-handed polarization (Figure 16). In the flare decay phase (at about of 07:25 UT), ZP and fiber bursts become strongly right-hand polarized. Combining magnetograms observed by the SDO Helioseismic and Magnetic Imager (HMI) with the homologous assumption of EUV flare brightenings and ZP bursts, we deduced that the observed ZPs correspond to the ordinary radio emission mode.

2.2.12. Strange Fibers in the Event on April 19, 2012

In Figure 17 an unusual type II burst consisting of fibers in the frequency range of 42–52 MHz is shown. A stronger emission of type III bursts was superimposed on the fibers.

The narrow instantaneous frequency bandwidth of each fiber ($< or \sim 1$ MHz) allows one to classify them as fiber bursts although they are not parallel to each other.

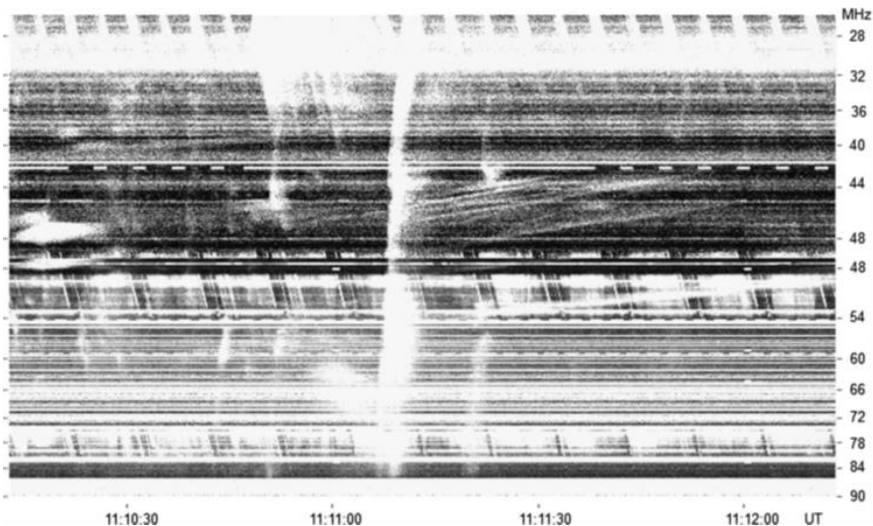


Figure 17. Type II burst on April 19, 2012 in the 25 – 90 MHz band (IZMIRAN) consisting of slow-drifting fibers (from Chernov et al., 2015a).

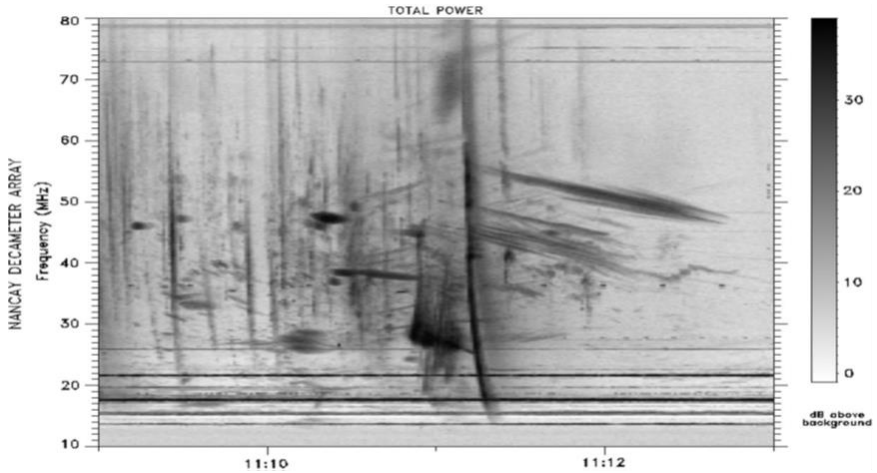


Figure 18. Type II burst on April 19, 2012 in the 10 – 70 MHz band with the Nançay Decametric Array (courtesy Alain Lecacheux).

Figure 18 shows the spectrum of this phenomenon obtained with the Nançay Decametric Array in the 10 – 80 MHz band. All large details match with the IZMIRAN spectrum. But here, a more sensitive tool finds another family of weak fibers with a reverse frequency drift and an ensemble of point-like spikes.

The slow drifting fibers in the type II burst (Figure 17 and 18) can be related with standing whistler wave packets in front of the shock front (Chernov, 1997). A magnetic trap is absent upstream the shock front, therefore in such a case the quasilinear interaction of whistlers with fast particles is also absent, and low frequency absorption does not take place. Certainly, we are still far from explaining all components in Figure 18, (besides several families of fibers, numerous point-like spikes). It is possible only to assume the complex turbulent structure before the shock front, or in the intersection region of two shock fronts.

2.2.13. *New Instrumentation*

Based on an old decimeter solar radio spectrometer working in the frequency range of 625–1500 MHz of the Yunnan Astronomical Observatories (YNAO) during the last solar cycle, Gao et al., (2014) designed a fully digital Fast Fourier Transform (FFT) spectrometer to upgrade the old one. The new digital spectrometer has the spectral resolution of 200 kHz, much higher than the old one (about 1.3 MHz). In addition, they also commissioned a new

metric solar radio telescope working in the frequency range of 70–700 MHz located at the Fuxian Solar Observatory of YNAO, deploying the same type of the digital FFT spectrometer. The two instruments have begun to operate in a daily survey mode since September 2009 and March 2012, respectively, and many solar radio bursts have been observed. In these events, various types of decimeter and metric fine structures with fairly meticulous spectral features were detected. These features could not be resolved in previous observations and studies. The information revealed by these new, fine resolution data can improve our knowledge and understanding of the physics of the energy conversion, particle acceleration and transportation during the solar eruption.

Figure 19 shows original fine structures in the August 1, 2010 event, and this confirms the high potential of these instruments in revealing the nature of ZP and other fine spectral structures.

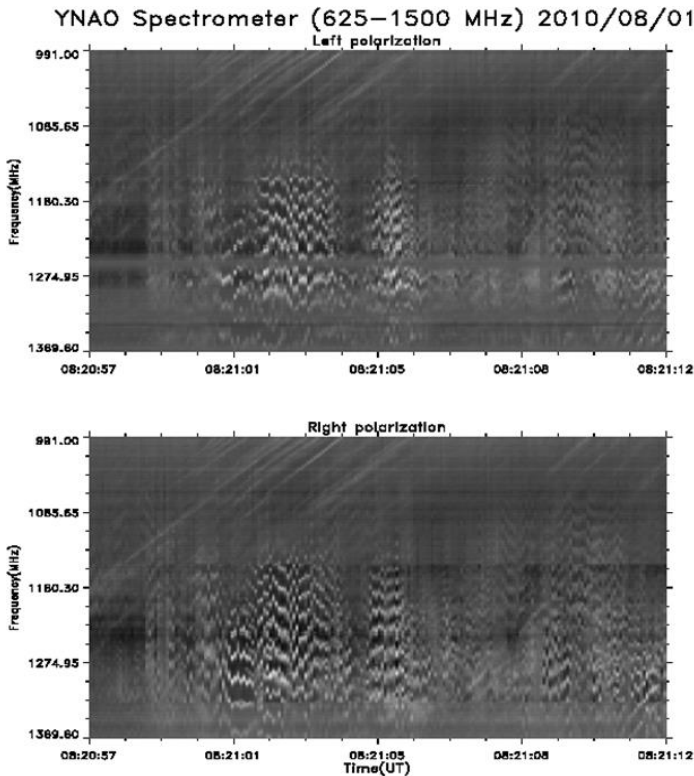


Figure 19. Fiber bursts and ZP in decimeter range of the YNAO Spectrometer (private communication from Guannan Gao).

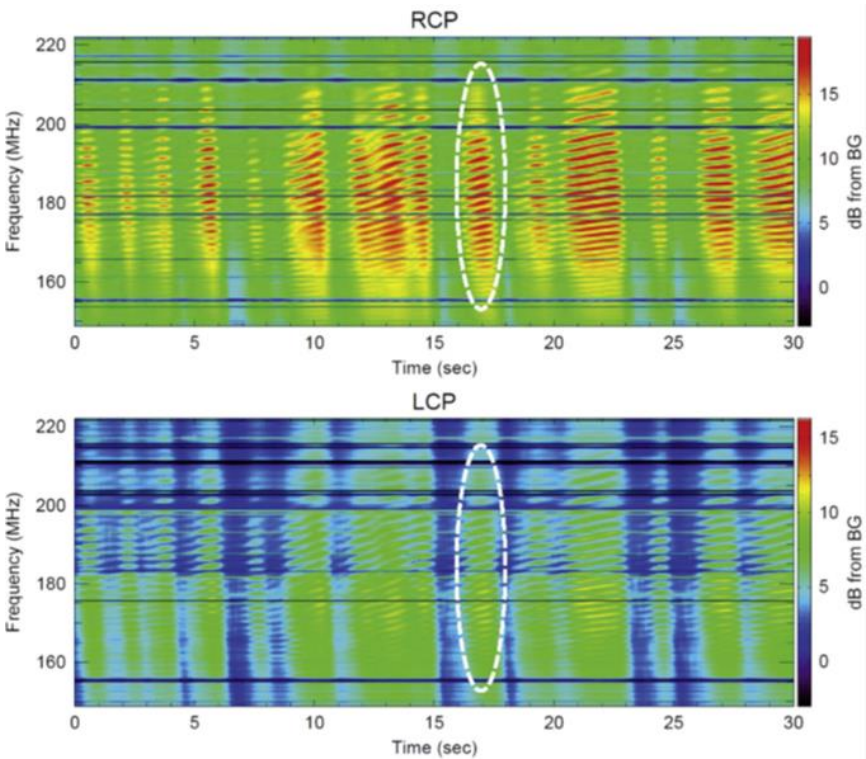


Figure 20. Magnified image of the ZP at 03:22:06–03:22:36 UT on June 21, 2011 (top: RCP, bottom: LCP). The ZP was enhanced in fast drifting envelopes observed with AMATERAS (Kaneda et al., 2015).

Kaneda et al., (2015) investigated the polarization characteristics of a zebra pattern (ZP) in a type-IV solar radio burst observed with AMATERAS on June 21, 2011 for the purpose of evaluating the generation processes of ZPs. Analyzing highly resolved spectral and polarization data revealed the frequency dependence of the degree of circular polarization and the delay between two polarized components (Figure 20). The degree of circular polarization was 50%–70% right-handed and it varied little as a function of frequency. Cross-correlation analysis determined that the left-handed circularly polarized component was delayed by 50–70 ms relative to the right-handed component over the entire frequency range of the ZP, and this delay increased with the frequency. The obtained polarization characteristics were examined by using existing ZP models, and it was concluded that the ZP was generated by the DPR process. However we suggest that the ZP emission was

originally generated in a completely polarized state in the O-mode and was partly converted into the X-mode near the source. Subsequently, the difference between the group velocities of the O-mode and X-mode caused the temporal delay.

2.2.14. High Resolution Observations with Artemis-IV Radio Spectrograph

Very recently Bouratzis et al., (2016) detected spike-bursts in the meter band, and they are of considerable interest as zebra-stripes have superfine structure in the form of ms spikes. In the context of this discussion peculiar spikes are of special interest, in particular the spike groups exhibiting lace-like morphology, chains of spikes in the form of N burst-like patterns and parallel to fiber bursts (see in Bouratzis et al., (2016) Figures 9, 11, 12).

2.2.15. Several Reminders about the Theory of ZP at DPR

Zlotnik (2013) recalls the main requirements for the instability at DPR. Namely, the background type IV continuum is due to the loss-cone instability of hot non-equilibrium electrons, and the enhanced striped radiation results from the double-plasma-resonance effect in the regions where the plasma frequency ω_{pe} coincides with the harmonics of electron gyrofrequency ω_{Be} , $\omega_{pe} = s \omega_{Be}$ (when $\omega_{Be} \ll \omega_{pe}$). Estimations of the electron number density and magnetic field in the coronal magnetic traps, as well as the electron number density and velocities of hot electrons necessary to excite the radiation with the observed fine structure, are given. In particular it is claimed that the wave-like dynamic spectrum of ZP is the radio image of fast magneto-acoustic oscillations of the coronal loop.

2.2.16. A reminder on the Polarization Theory of ZP

Zlotnik, Zaitsev and Altyntsev (2014) discuss the problem of strong polarization of the zebra-type fine structure in solar radio emission. The degree of polarization of the radio emission at twice the plasma frequency originating from the coalescence of two plasma waves is proportional to the ratio of the electron gyrofrequency to the plasma frequency, which is a small number and is negligible. The outgoing radio emission at the fundamental frequency can be strongly polarized as the ordinary mode due to the escaping conditions. Special attention is given to the examination of depolarization effects in the course of propagation in the corona. It is shown that the depolarization of the radio emission propagating in the corona cannot be associated with the effect

of linear coupling of electromagnetic waves in the region of the perpendicular magnetic field.

3. ADDITIONAL DISCUSSION

The study of a short radio burst with rich fine structures on 11 April 2013 showed that each new radio maximum was related to a new flare brightening seen in EUV images of SDO/AIA. Each radio maximum has its own fine structures, usually composed of several stripes of ZP or ZP near the high frequency edge of fast pulsations. Such a relation indicates there is a close connection between radio sources of pulsations and ZP. The 131 Å movie showed a flare loop arcade forming between two sigmoid flare ribbons. Therefore the flare dynamics consisted of consecutive magnetic reconnections in different arcade loops.

The polarization changed in accordance with the position of the new flare brightening. The left flare ribbon was located above the North magnetic polarity (tail spot) and the right ribbon above the South magnetic polarity (leading spot). In all cases, the radio emission mode remained ordinary. When the brightening took place at the looptops, the polarization was very weak, almost zero.

The magnetic field remained stable during the event. At the same time it was improbable that motion of the radio source from one flare ribbon to another one lasted several seconds. A similar explanation of a gradual changing of the polarization sign at 17 GHz (Nobeyama data) was proposed by Huang and Lin, 2006.

Only one question arises: why we receive only a partial degree of polarization? If the emission is generated at the fundamental (by some mechanism) as the ordinary mode, it is fully polarized in the source. During propagation of the radio waves the observed polarization degree is changed due to a depolarization effect. The depolarization happens in a layer where the radio emission is propagated exactly across the magnetic field. In the considered event, the source geometry (the flare occurred at the disk centre) allows that this condition is possibly satisfied for a ZP source in a closed magnetic trap (for more details see Chernov and Zlobec (1995)).

The generation of fast radio pulsations is probably caused by fast electrons accelerated in the upward direction in a vertical current sheet simultaneously with magnetic reconnection. Some of the fast particles that are accelerated downward can be captured in a closed magnetic trap and they could be

responsible for the emission of ZP by some single mechanism. The diversity of ZP stripes is probably given by different conditions in different arcade loops. This is a natural scheme that is in accordance with the standard model of the solar flare as shown in Figure 21.

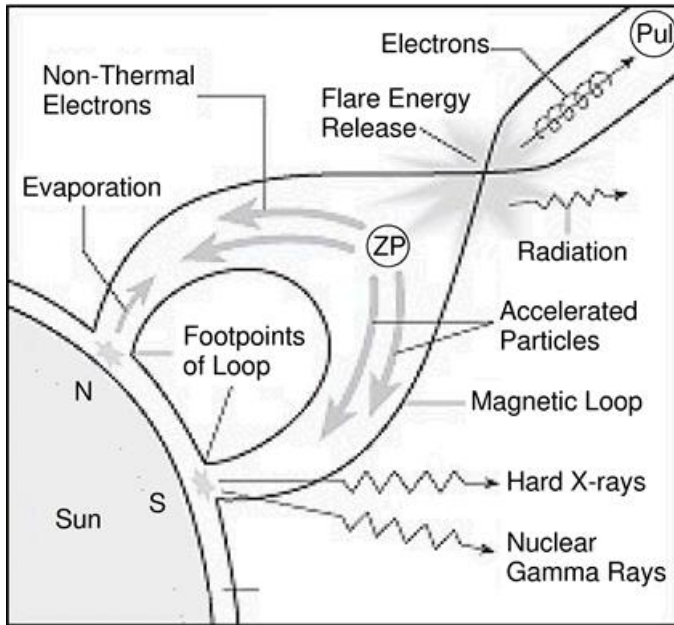


Figure 21. Expected radio source positions of ZP and pulsations (Pul) in the schematic sketch of the standard flare model of Aschwanden, 2006.

Such an expected location of a microwave ZP source at tops of flare magnetic loops was also confirmed in a recent paper by Yasnov and Karlický (2015) that presents results of estimation of bremsstrahlung and cyclotron absorptions of radiation in the corona.

We do not have any convincing evidence that the mechanism that generates a ZP is the emission of Bernstein modes as this was proposed by Tan et al., (2014b) for the first strong ZP. First, an exact definition of the frequency separation between three (and sometimes four) zebra stripes is too problematic. Second, the polarization should be related to the extraordinary mode (Zlotnik, 1976; Kuznetsov, 2005). Third, we do not have any information about size of the radio source with height in the corona (distributed or point like). Else, the radio emission produced by Bernstein modes must be weak, much weaker than in other mechanism, i.e., in the DPR

(Zlotnik, 2009) or interaction of Langmuir waves with whistlers (Chernov, 2006). In both of the latter models, the radio source should be distributed in the vertical direction, but in the DPR model the source should be stationary and in the whistler model – moving (depending on the group velocity of the whistler wave) (for more details see Chernov, Yan and Fu, 2014a). Furthermore, the spatial drift of ZP stripes should change synchronously with changes in the frequency drift of the dynamical spectrum. Recently, more than ten other mechanisms were proposed for ZP, but their significance remains uncertain (Chernov et al., 2015).

To choose which mechanism applies, spatially-resolving observations may be crucial, and it is desirable to observe a limb event. Now, we are expecting progress in the field of solar radio imaging spectroscopy. The first trial observations began on the new Chinese Spectral Radioheliograph (CSRH) which will be the largest and most advanced radio imaging telescope for the solar corona in the world (Yan et al., 2009; Yan et al., 2013).

In several events opposite combinations of a ZP and fiber bursts were observed, when fibers limit the ZP emission to the high frequency part in the decimeter band in the December 1, 2004 event (see Figure 4 in Chernov et al., 2014) and microwave band in the August 1, 2010 event (see Figure 3 in Chernov et al., 2014a). For such events we propose another combinations of radio sources (Figure 22) when ZP is emitted from a magnetic island.

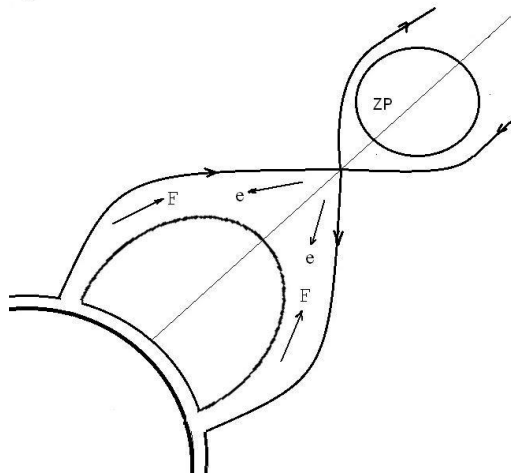


Figure 22. Expected radio source positions of ZP and fiber bursts in events on December 1, 2004 and August 1, 2010.

3.1. Debatable Points

The recently studied events show that the ZP and fiber bursts can appear almost simultaneously or consecutively in the microwave, decimeter and meter wave bands. In the December 1, 2004 and August 1, 2010 events they were almost superimposed on each other. Certainly this fact was known earlier. For example, in the meter range see Figure 4.9 in Chernov, 2011 and in the microwave – *ibid*, Figure 4.38. However when interpreting such phenomena authors usually artificially mark out two idealized structures, either parallel drifting (probably wavy) stripes of the zebra- structure or fiber bursts with intermediate frequency drift (constant and negative). Though the phenomena in which ZP stripes gradually become fibers and back are known (see, for example, the monograph of Chernov (2011) Figure 4.13 and 4.22). In the event on 15 February 2011 we also have an example (Figure 8) of such conversion of one structure into another.

The weak zebra (Figure 2a and Figure 8 in Chernov et al., 2015) can be readily explained by the whistler model, when periodic whistler wave packets fill in the whole magnetic trap. The appearance of fiber bursts in the same frequency band where two minutes before fast pulsations were observed (Figure 7), tests whether the radio sources of both structures are the same, and whether both are created by the whistler mechanism (see Ch.1 in Chernov (2011)).

In the theory of formation of these structures most often any smooth transition of one structure to another is not considered at all. In the theory of ZP the broad acceptance obtained the DPR mechanism. Fiber bursts are explained by a completely different mechanism, the interaction of plasma waves with the whistlers. The DPR mechanism obtained wide recognition due to the very detailed developments of Zheleznyakov (1995) and subsequent series of articles and reviews of Zlotnik (Zlotnik et al., (2003). Zlotnik (2009), Zlotnik, (2010)).

However, the DPR theory achieves completeness of analytical analysis as well as the source model by its simplicity. The impression of the authenticity of the model and operation of the mechanism is immediately created. This allows us to assume that the DPR mechanism must always work, if there is a magnetic trap, in which the plasma density and the magnetic field strength decrease smoothly with the height in the corona with different gradients. A question simultaneously arises, why then does ZP only appears irregularly (by per-second intervals) in prolonged phenomena. In the images of SOHO/EIT then of TRACE and now also of SDO/AIA the magnetic flare loops remain

almost constant during the entire phenomenon. The repetitive maxima of continuous emission confirm the presence of fast particles. However, ZP only appears irregularly for several seconds.

Up to now, we do not have any information about the operation of the DPR mechanism at several resonance levels in laboratory plasma experiments (see also Section 4.5) although numerical simulations of magnetic reconnection and excitation of ion-acoustic and whistler waves have long history. The observations of the last few years confirm the superfine structure of flare magnetic loops. In particular, in number of works it was shown that in thin loops the magnetic field weakly changes with height (Aschwanden, 2004). In such loops it is not possible to expect even two DPR levels, even with the most diverse assumptions about the decrease in the density with height. It is possible to recall that in some phenomena more than 30 zebra stripes were observed simultaneously in the 2.6 - 3.8 GHz band. Thus, it is shown that in any known models of coronal plasma it is impossible to obtain a large number of DPR levels (see Figure 5.21 of Chernov, 2011).

Nevertheless, there have not been attempts to demonstrate a possible existence of a number of DPR levels in space plasmas. Moreover, scale heights are taken arbitrarily in order to obtain several intersections of the curves of plasma frequency and electronic cyclotron harmonics as, for example this is done by Chen et al (2011). It is considered that the DPR mechanism explains any phenomena with ZP. Practically all works discussing the DPR mechanism the presence of a large number of DPR levels is considered obvious. Only in Zlotnik et al (2003) is an attempt to make a more concrete specific selection of the magnetic trap with the use of the calculated magnetic map above AR for the event on October 25, 1994. However, the selection of a basic loop was made arbitrarily (and possibly erroneously) without taking into account the fact that the particles critical for III type bursts and ZP moved in different directions (for greater detail, see Chernov et al., (2005)).

In several recent works the authors began to compare DPR models and the models based on interaction of plasma waves with whistlers. In this case an inaccuracy in the estimations of different parameters of whistlers was allowed. In this context, it is necessary to note that the whistler model was mistakenly rejected by Chen et al., (2011) (see above). In Tan et al., (2012) the estimation of the magnetic field strength using the frequency drift of fibers in the whistler model is made for the frequency of whistlers f_w relative to electron cyclotron frequency $x = f_w/f_{ce} = 0.01$, and in the estimation of the field according to the frequency separation of zebra strips in the same frequency range it is taken as

$x = 0.25$. As a result in the latter case the field strength is underestimated by twice, and the model with the whistlers is rejected. The value x is determined by the frequency at which the value of the increment of whistlers is maximum. According to Chernov (2011) the value x is in the interval of 0.1 to 0.01 depending on different parameters of the distribution function of fast particles. Therefore the values of the field strength in the whistler model must exceed estimations obtained in the DPR model.

In the critical review of Zlotnik (2009), the advantages of the DPR model and the main shortcomings of the whistler model are refined. The author asserts that the theory based on the DPR effect is the best-developed theory for the origin of ZP at meter-decimeter wavelengths at the present time. It explains the fundamental ZP feature in a natural way, namely, the harmonic structure (frequency spacing, numerous stripes, frequency drift, etc.) and gives a good fit for the observed peculiarities in the radio spectrum with quite reasonable parameters of the radiating electrons and coronal plasma. The statement that the theory based on whistlers is able to only explain a single stripe (e.g., a fiber burst) was made in Zlotnik (2009) without the correct consideration of whistler excitation and propagation in the solar corona.

Zlotnik uses the term “oscillation period” of whistlers connected with the bounce motion of fast particles in the magnetic trap. Actually, the loss-cone particle distribution is formed as a result of several passages of the particles in the magnetic trap. Kuijpers (1975) explains the periodicity of the fiber burst using this bounce period (~ 1 s). If we have one rapid injection of fast particles, whistlers (excited at the normal electron cyclotron resonance) propagate towards the particles (they disperse in the space). Quasilinear effects thereby do not operate in normal resonance.

A ZP is rather connected with whistlers excited at anomalous resonance during long lasting injection. In such a case, waves and particles propagate in the same direction, and quasilinear effects begin operate and their role increases with increasing duration of injections. Different stripes of the ZP are then excited because the division of the magnetic trap into zones of maximum amplification of whistlers, separated by intervals of whistler absorption (see more details in Chernov (1990)). The bounce period does not interfere with this process, but it can be superimposed on the ZP.

However, the whistler amplification length is always small (on the order of 10^8 cm in comparison with the length of the magnetic trap being $>10^9$ cm) for any energy of fast particles (Breizman, 1987, Stepanov and Tsap, 1999). According to Gladd (1983), the growth rate of whistlers for relativistic energies of fast particles decreases slightly if the full relativistic dispersion is

used. In this case, the whistlers are excited by anisotropic electron distributions due to anomalous Doppler cyclotron resonance.

Later, Tsang (1984) specified calculations of relativistic growth rates of whistlers with the loss-cone distribution function. It was shown that relativistic effects slightly reduce growth rates. According to Figure 8 in Tsang (1984), the relativistic growth rate is roughly five times lower than the nonrelativistic growth rate. However, the relativistic growth rates increase with the perpendicular temperature of hot electrons T_{\perp} . According to Figure 5 in Tsang (1984), the growth rate increases about two times with increases the electron energy from 100 to 350 keV, if other parameters of hot electrons: loss-cone angle, ratio of gyrofrequency to plasma frequency, temperature anisotropy ($T_{\perp}/T_{\parallel} = 3$) are kept.

Thus, it was known long ago that the whistlers can be excited by a relativistic beam with loss-cone anisotropy. Equation (13.4) in Breizman (1987), coinciding with Eq. (29) in Chernov 2006) that evaluates the smallest possible relaxation length of the beam, has no limitations in the value of energy of fast particles.

A critical comparison of models has been repeated in Zlotnik (2010), only with a new remark concerning the Manley-Rowe relation for the brightness temperature of electromagnetic radiation T_b that is a result of coupling of Langmuir and whistler waves:

$$T_b = \frac{\omega T_l T_w}{\omega_l T_w \sqrt{1 + \frac{\omega_w T_l}{\omega_l T_w}}}, \tag{2}$$

where ω_w and ω_l - frequencies of whistler and Langmuir waves, and T_w and T_l - energies of whistler and Langmuir waves respectively. Zlotnik (2010) states that since $\omega_w \ll \omega_l$, in the denominator only the first term remains, and T_b depends only on T_l , with $T_b \sim T_l$, i.e., the process does not depend on the level of whistler energy. However, Kuijpers (1975) (Eq. (32)) shows that the second term $\omega_w T_l$ should be $\gg \omega_l T_w$ due to $T_l \gg T_w$. An analogous conclusion was made by Fomichev and Fainshtein (1988) with more exact relation of the three wave intensities (see also Eq. (11) in Chernov (2006)). Therefore the value of T_b in the process $l + w \rightarrow t$ depends mainly on T_w . Thus, our conclusion that the entire magnetic trap can be divided into intermittent layers of whistler amplification and absorption remains valid for a broad energy range of fast particles.

In Zlotnik (2009) the main matter which is ignored is that the model involves quasilinear interactions of whistlers with fast particles, allowing one to explain all the fine effects of the ZP dynamics, mainly the superfine structure of ZP stripes and the oscillating frequency drift of the stripes which occurs synchronously with the spatial drift of radio sources. For an explanation of the superfine structure the alternative whistler model remains as the most natural: the dynamic energy transfer between two ion-sound waves (s and s') and whistler waves (w) in a pulsating regime with the process $s + s' \rightarrow w$ (Chernov, Yan, Fu, 2003; Chernov, 2011, section 4.7.5).

Similar continuous discussions stimulate the development of new models. Treumann et al., (2011) proposed a new mechanism for ZP, the ion-cyclotron maser. Thanks to the special delta-shaped distribution function of the accelerated ions, the ion-cyclotron maser generates a number of electromagnetic ion-cyclotron harmonics which modulate the electron maser emission. A part of the accelerated relativistic protons passes along the magnetic field across the trapped loss-cone electron distribution. The modulation of the loss-cone will necessarily cause a modulation of the electron cyclotron maser. Locally this produces the typical “Zebra” emission/absorption bands. However this mechanism can work in an unrealistically strong magnetic field, where $f_{pe}/f_{ce} < 1$.

4. RECENT RESULTS ON THE IMPROVEMENT OF THE DPR MODEL

Karlicky made a big contribution to the development and improvement the DPR mechanism.

Karlický et al., (2013) continued the development of the model of Kuznetsov (2006) for fiber bursts. Kuznetsov (2006) proposed a model in which the fiber bursts are generated by a modulation of the radio emission by magneto-hydrodynamic waves. He also proposed that these waves could be magneto-acoustic waves of a sausage mode type that propagate along a dense coronal loop. Fiber bursts can be explained by a propagating fast sausage magneto-acoustic wave train. Then Karlický (2013) extended a similar model for ZP: the magneto-acoustic waves with density variations modulate the radio continua, and this modulation generates zebra effects. It should be noted that a self-consistent model (with density heterogeneities) was examined by Laptuhov and Chernov (2009; 2012).

Karlický and Yasnov (2015) present a new method of the determination of the magnetic field strength and plasma density in the solar zebra radio sources.

Using the double plasma resonance (DPR) model of the zebra emission they derived analytically the equations for computations of the gyroharmonic number s of a selected zebra line and then they solved these equations numerically. The method was successfully tested on artificially generated zebras and then applied to observed ones. The magnetic field strength and plasma density in the radio sources were determined. Simultaneously, they evaluated the parameter $L_{nb} = 2L_b/(2L_n - L_b)$, where L_n and L_b are the characteristic scale-heights of the plasma density and magnetic field strength in the zebra source, respectively. Computations show that the maximum frequency of the low-polarized zebras is about 8 GHz, in very good agreement with observations. For the high-polarized zebras this limit is about 4 times lower. It was shown that microwave zebras are preferentially generated in the regions with steep gradients of the plasma density as for example in the transition region, on the basis of the previous results of the authors (Yasnov and Karlický, 2015) using the density model by Selhorst, Silva-V´alio, and Costa (2008) (Figure 23). In models with smaller density gradients as e.g., in those with the barometric density profile, the microwave zebras cannot be produced owing to the strong bremsstrahlung and cyclotron absorption affecting the non-thermal electrons. They also showed that this DPR model is able to explain the zebras with frequency-equidistant zebra lines.

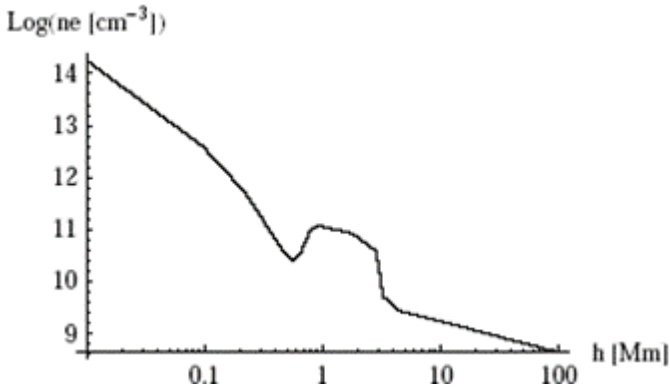


Figure 23. The electron density profile as a function of height in the solar atmosphere according to Selhorst et al., (2008).

The bremsstrahlung absorption in atmospheric layers above the DPR zebra generation region and the cyclotron absorption in the DPR region and in

the gyroresonance layers at higher altitudes limit the spectrum of zebras and micro bursts (MB) from both high-frequency and low-frequency sides.

Karlický (2013) extended his model to the ZP discovered in radio emission of Crab pulsar: ZPs similar to those analyzed in solar observations were observed in the radio emission of the Crab Nebula pulsar (Hankins and Eilek 2007), see Figure 24.

Recently, these ZP were interpreted by Zheleznyakov et al., (2012) using the DPR model. This explains many observed features of these zebras. However, the main problem of the model is that it requires relatively low magnetic field in the pulsar radio source.

Simulations of Karlický (2013) assume that in the pulsar atmosphere the radio continuum is generated at the double-plasma frequency $2\omega_{pe}$ from two coalescing plasma (Langmuir) waves. Furthermore, in the radio continuum source they assumed a fast magneto-acoustic wave. This wave propagates at the Alfvén speed, which in our case of a very high magnetic field B , is close to the speed of light c .

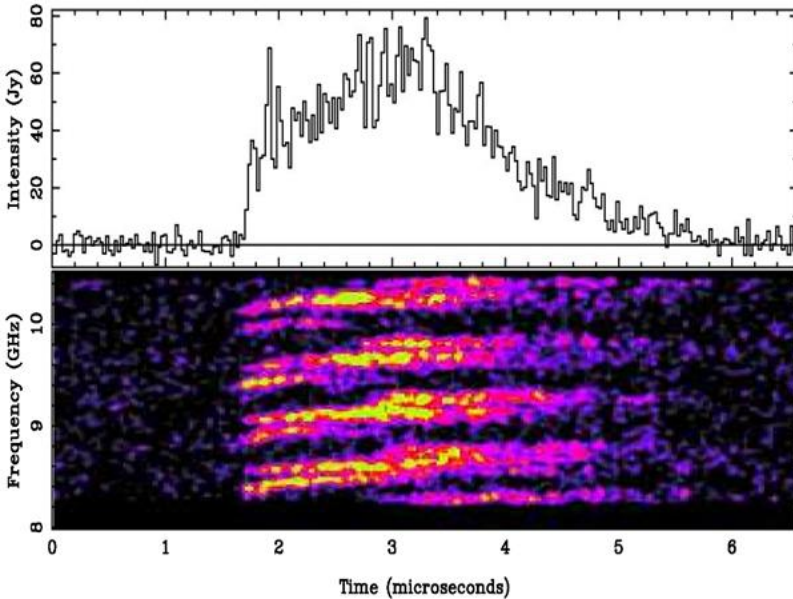


Figure 24. Zebra pattern spectrum in microwave emission from the Crab Nebula pulsar (Hankins and Eilek 2007).

Karlický proposes that the frequency drift of the observed zebra is caused by the propagating fast magneto-acoustic wave. It gives us the spatial scale in

the density model. The wave velocity is $v_A \approx c$, the used relative amplitude of density perturbations and the wavelength are $n_R = 0.01$ and 1.5 km, respectively. Due to the positive frequency drift of the observed zebra stripes, the assumed wave propagates toward lower heights in the present density model. He used the same procedure as in the solar case, and computed radio spectrum. To better specify them a more specific model of the pulsar radio continuum is needed.

In other models, e.g., in the model of Hankins and Eilek (2007), the radio source is in the highly relativistic jet.

It should be noted that nobody has taken into consideration the basic special features of the pulsar zebra: stripes have dual structure, four large envelopes split into 2-3 the narrow stripes, and the duration (microseconds) that is 6 orders of magnitude shorter than the solar one.

4.1. “Fingerprint” ZP

In the recent paper of Zlotnik, Zaitsev, Melnik et al., (2015) a peculiar fine structure in the dynamic spectrum of the solar radio emission discovered by the Radio Telescope UTR-2 spectrograph (Kharkov, Ukraine) in the frequency band 20-30MHz is studied. The structure is observed against the background of a broadband type IV radio burst and consists of the parallel drifting narrow bands of enhanced (in comparison with the background) emission and absorption (Figure 25). The observed structure differs from the widely known ZP at the meter and decimeter wavelengths by the opposite directions of the frequency drift within the limits of a single stripe at a given time, and hence was called a “fingerprint structure” by the authors. It is shown that the observed peculiarities can be understood in the framework of the plasma mechanism of the radiation by virtue of the DPR effect in a nonuniform coronal magnetic trap. The source model providing the peculiar frequency drift of the zebra stripes is proposed.

The authors thoroughly selected the numbers of harmonics and showed that the best fit with the observed forms of stripes (“fingerprint” or vertical arcs) gives the collection of the harmonics $s = 20-30$. They used a slightly modified Newkirk model for the density and the specific functional form of the magnetic field on height ($B = B_0(t)/(1 + h/7.95)^3$). The magnetic field gradient must be very similar to the electron number density gradient with opposite signs of these gradients at the upper and lower parts of the source (to provide different signs of the frequency drift in the high- and low-frequency

parts of the spectrum). At each time no more than 1-3 harmonics are observed, and each harmonic must twice intersect the curve of plasma frequency in each instant of time (Figure 26). The authors conclude that the presented model of the source is able to explain the details of the unusual frequency drift of the stripes of enhanced intensity in the observed fingerprint spectrum within the framework of the DPR mechanism under quite reasonable physical conditions in the coronal magnetic trap.

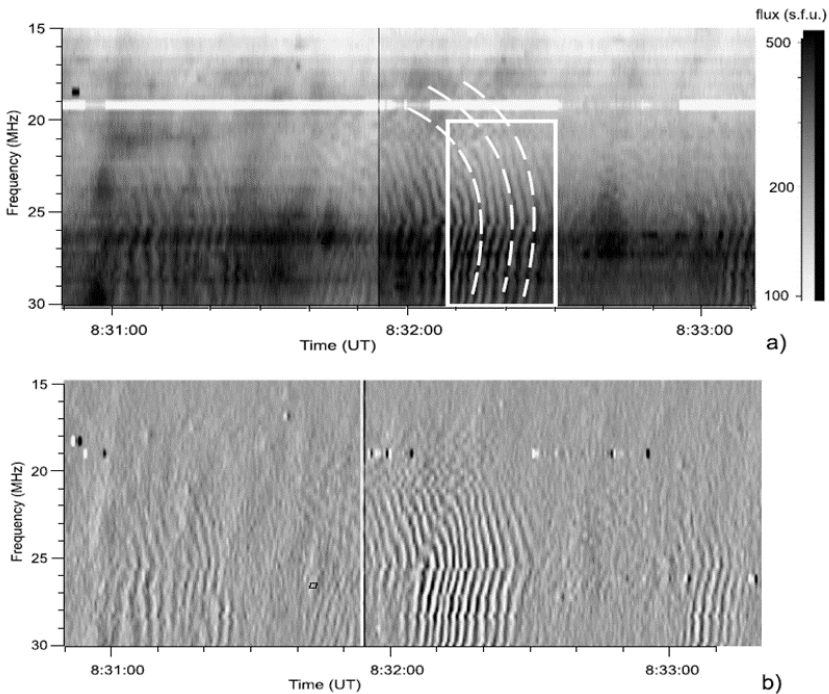


Figure 25. Dynamic spectrum of the solar burst ‘fingerprint’ on 22 July 2004 (a) and its differential dynamic spectrum (b). The rectangle indicates the portion that is used for the numerical analysis. The dashed lines schematically show the form of the fine structure line (from Zlotnik, et al., (2015).

In this connection, it is worth noting that intensity time profiles at frequency 25.45 MHz shown in Figure 27 (from a previous paper of Melnik et al., 2008) presents more evident absorptions of the continuum level. Besides, the differential spectrum at the bottom of Figure 25 shows evident disruptions of stripes at 25.5 MHz (just a nose frequency). Other elements of the continuum emission do not show any disruptions.

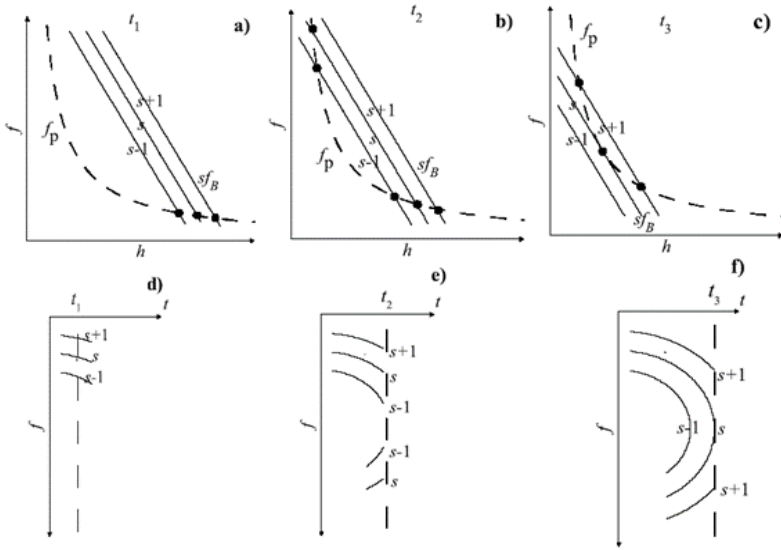


Figure 26. Qualitative interpretation of the fingerprint structure as a set of quasi-vertical arcs. The top panel is the source model at three times $t_1 < t_2 < t_3$; the electron number density remains constant, and the magnetic field decreases in time. The filled circles denote the DPR levels. The lower panel gives the dynamic spectrum with the zebra stripes corresponding to the times t_1 , t_2 , and t_3 (from Zlotnik, et al., (2015)).

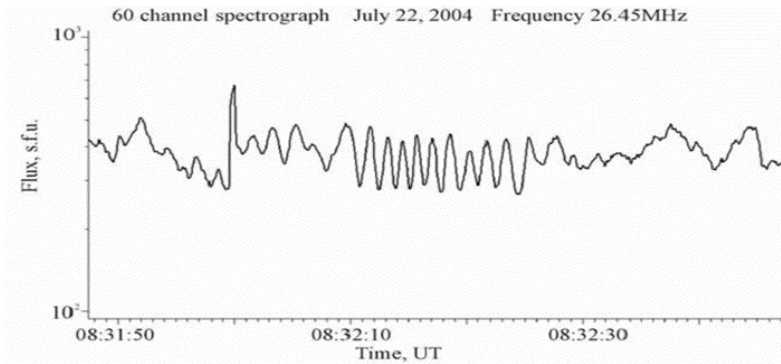


Figure 27. Intensity profile at 25.45 MHz of ZP in the July 22, 2004 event observed by spectrograph of the Radio Telescope UTR-2 (from Melnik, Rucker and Konovalenko, 2008).

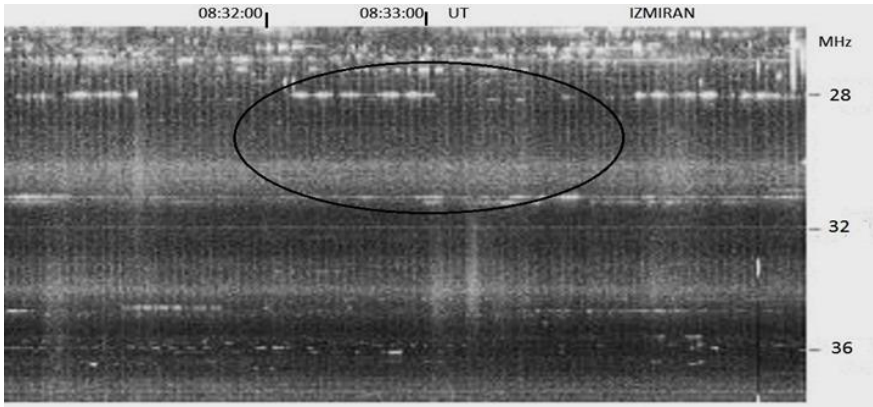


Figure 28. IZMIRAN spectrum of the July 22, 2004 event in the range 25-40 MHz.

The solar origin of this unusual ZP was confirmed by the IZMIRAN spectrum (Figure 28) where some zebra-stripes are visible in the designated oval, although the instrument sensitivity was one order of magnitude lower, and it had a limit time resolution of 1 s.

Summarising, it is possible to still note that the decrease of magnetic field assumed for explaining the frequency drift by a fast magneto-acoustic wave (FMA) seems improbable at the heights in the upper corona of one solar radius, very distant from a flare. The life time of the zebra was evaluated by FMA wave period, i.e., without the FMA wave the DPR mechanism does not work? And really, Karlický (2013) extended a model of Kuznetsov (2006) for fiber bursts, for ZP: the magnetoacoustic waves with density variations modulate the radio continua, and this modulation generates zebra effects (but in the microwave band).

Disruption of the zebra stripes just at nose frequencies says that stripes drifted from different levels independently.

In such a case, the model of the ZP could be much simpler. The ZP appeared simultaneously with coronal mass ejection after which a magnetic islands were formed wherein the fast particles were accelerated simultaneously in top and bottom X- points of the magnetic reconnection. Periodical whistler wave packets generated by these particles propagated towards each other and their interaction with plasma waves gives stripes in emission and absorption. The group velocity of whistlers for the ratio $f_p/f_b = 20$ will be about 10^9 cm s⁻¹.

The estimation of a possible positive frequency drift (for instance, between 20 and 25 MHz) $df/dt = -f V_{gr}/2L_n$ where L_n is the scale height of density of $= 10^{10}$ cm gives about the same value as observed, of 1MHz s⁻¹.

The radio source of the ZP was evidently located in the tail of the CME, in an inhomogeneous plasma, therefore it is possible to examine also the applicability of other mechanisms, for example radio wave propagation through small heterogeneities in the tail of CME (Lapuhov and Chernov, 2009). However, in this case two sources must also emit simultaneously (above and below the magnetic cloud), and heterogeneities must drift towards each other. Lapuhov and Chernov (2012) showed that alternating transparency and opacity stripes in the spectrum of radio waves passing through such a plasma structure (the zebra pattern effect) can be observed at any angle of incidence.

4.2. Laboratory Plasma Experiments

We found only one confirmation about the operation of DPR mechanism in the laboratory installations but only at the second cyclotron harmonic (Figure 29) in Viktorov, Mansfeld and Golubev (2015a). In this paper the authors report kinetic instabilities of nonequilibrium plasma heated by powerful radiation of a gyrotron at the electron cyclotron resonance (ECR) and confined in a mirror magnetic trap.

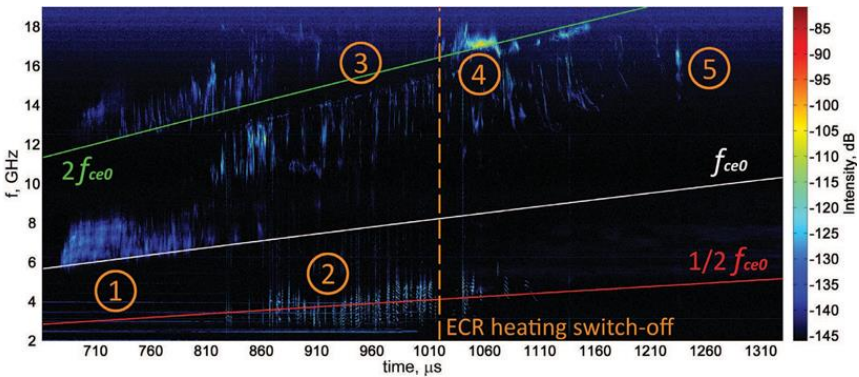


Figure 29. Dynamic spectrum of the plasma radiation. The types of kinetic instabilities considered in the paper are highlighted in the Figure: 1: the initial stage of the ECR discharge (rarefied plasma); 2 and 3: stages of the developed discharge (dense plasma); 4: the beginning phase of plasma decay (dense plasma); 5: decaying plasma (rarefied plasma). The three lines on the spectrogram show the time variation of the corresponding frequencies $2f_{ce0}$ (green), f_{ce0} (white) and $1/2f_{ce0}$ (red), where $f_{ce0} = f_{ce}$ (z center) is the electron cyclotron frequency in the center of the magnetic trap on its axis (a part of Figure 2 from Viktorov, Mansfeld and Golubev (2015a)).

It is seen in Figure 29 that any emission at the third cyclotron harmonic is absent. It is possible certainly to connect this with the difficulties of designing in the installation the parameters of plasma similar in the magnetic trap in the solar corona, especially the ratio $f_p/f_b \gg 1$.

Emission of the dense plasma at frequencies about $f_{ce0}/2$ (type 2 in Figure 29) is more likely related to the whistler mode instability. The observed radiation at higher frequencies with the sharp upper spectral boundary (type 3) can be apparently related to the excitation of plasma waves at the upper hybrid resonance.

Similar experiment is discussed also in Viktorov, Golubev, Zaitsev and Mansfeld (2015b), where the DPR is discussed in more details. However, the main attention is devoted to a fast temporal structure of observed radio emission.

CONCLUSION

We have shown that the polarization of the ZP corresponds to the ordinary wave mode and it changes in accordance with the dynamics of flare processes. Simultaneous or consecutive appearance of ZP in different frequency bands is obviously connected with the dynamics of flare processes.

A future analysis is needed to clarify whether a radio source showing ZP is really related to a closed magnetic loop, and if it is located at lower altitudes than the source of the pulsations, as is shown by the radio spectrum of ZP at the high frequency boundary of pulsations. New solar radio spectral imaging observations should help to compare the source sizes of different fine structures, and reveal their possible motion.

In the whistler model radio sources of fiber bursts and ZP are moving, and the spatial drift of ZP stripes should change synchronously with the changes of the frequency drift in the dynamical spectrum. In the DPR model, the ZP source must be rather stationary.

In almost all papers the interpretation of ZP begins with the most accepted DPR model. Above, we highlighted several additional problems with this model in the explanation of complicated events. We showed that the event on December 14, 2006 examined in the highly cited paper of Chen et al., (2011) in terms of the DPR model, could be likewise explained in terms of the whistler model, taking into account the propagation of whistlers along a magnetic trap.

The “fingerprint” form of the ZP in the decameter band is also discussed in the DPR model, whereas it can be simply related with the whistler propagation in magnetic islands. Zlotnik et al., (2015) explain the fast frequency drift and lifetime of the ZP in terms of the FMA waves which modulate the DPR mechanism, while Karlický (2013) used the density perturbations in the FMA waves (modulating the continuum emission) as a source of ZP without any attraction of the DPR. At the same time Yu et al., (2013), explain only the quasi-periodic wiggles of a microwave ZP in terms of the FMA oscillation.

The DPR mechanism was even used to interpret zebra-like stripes in microwave radiation of the Crab Nebula pulsar, despite numerous problems with the plasma parameters. Those problems motivated Karlický to develop a ZP model, based on the FMA waves, for pulsars.

Simultaneous appearances of fibers and ZP and the smooth transition of zebra-stripes into the fibers and back indicate the united mechanism for the formation of different drifting stripes in emission and absorption within the framework of the interaction of plasma waves with whistlers, taking into account quasi-linear interaction of whistlers with the fast particles and with ion-acoustic waves.

In contrast with the DPR model, the whistler model explains many specific features of ZP:

- weak zebra stripes with different scales in a broadband frequency range;
- simultaneous appearance of fiber bursts, fast pulsations and spike-bursts;
- the oscillatory frequency drift and the frequency splitting of stripes;
- a change in the spatial drift of radio source synchronously with the frequency drift of stripes in the spectrum;
- the millisecond superfine structure of stripes;
- the rope-like fibers.

The presence of ion-acoustic waves can be considered justified in the source in the vicinity of magnetic reconnection with the outgoing shock fronts. The propagating ion-acoustic waves can serve as natural heterogeneities, passing through which electromagnetic waves shape the additional stripes of transparency and opacity in the spectrum. Laptukhov and Chernov (2012) showed that alternating transparency and opacity stripes in the spectrum of

radio waves passing through such a plasma structure (the ZP effect) can be observed at any angle of incidence.

It should be noted that the relative significance of these several recently proposed mechanisms remains uncertain.

Simultaneous or consecutive appearance of ZP in different frequency bands is obviously connected with the dynamics of flare processes.

For a comprehensive discussion of comparative analysis of observations of ZP and fiber bursts and different theoretical models we refer the reader to the review of Chernov (2012).

ACKNOWLEDGMENTS

The author is grateful to all authors and all editions granted permissions to use their data. The author is grateful to the RHESSI, SOHO (LASCO/EIT), SDO and Nobeyama Radioheliograph teams for operating the instruments and performing the basic data reduction, and especially, for the open data policy. The research that was carried out by G. P. Chernov at National Astronomical Observatories (NAOC) was supported by the Chinese Academy of Sciences Visiting Professorship for Senior International Scientists, grant No. 2011T1J20. The author is grateful to the Chinese colleagues: Yihua Yan, Baolin Tan, Chengming Tan. This work is also supported by the Russian Foundation for Basic Research under Grant 14-02-00367.

REFERENCES

- Altyntsev, A. T., Lesovoi, S. V., Meshalkina, N. S., Sych, R. A., and Yan, Y.: 2011, *Sol. Phys.* 273, 163.
- Aschwanden M., 2004, *Physics of the Solar Corona. An Introduction*, Springer, Praxis Publishing Ltd, Chichester, UK.
- Aschwanden M. J. 2006, The standart model of a flare, ppt presentation at AIA/HMI workshop, Monterey 2006.
- Bárta, M. and Karlický, M.: 2006, *Astron. Astrophys.* 450, 359.
- Bouratzis C., Hillaris, A., Alissandrakis, C. E., Preka-Papadema, P., Moussas, X. C., Caroubalos, Tsitsipis, P., and A. Kontogeorgos 2016, *Astron. Astrophys.* 586, A 29.

- Breizman, B. N.: 1987, in *Problems in Plasma Theory*, Kadomtsev, B.B. Eds., Energoizdat, Moscow (in Russian), 15, 55.
- Chen Bin, T. S. Bastian, D. E. Gary, and Ju Jing, 2011, Spatially and spectrally resolved observations of a zebra pattern in solar decimetric radio burst, *Astrophys. J.* 736, 64.
- Chernov, G. P.: 1976, *Sov. Astron.* 20, 582.
- Chernov, G. P.: 1990, *Sol. Phys.* 130, 75.
- Chernov, G. P.: 1997, *Astronomy Letters*, **23**, 827.
- Chernov, G. P.: 2005, Recent data on zebra patterns, *Astron. Astrophys.* 437, 1047-1054.
- Chernov, G. P.: 2006, *Space Sci. Rev.* 127, 195.
- Chernov, G. P.: 2010, *Research in Astron. Astrophys.* 10, 9, 821.
- Chernov, G. P., and Zlobec, P.: 1995, *Solar Phys.* 160, 79.
- Chernov, G. P., Fu, Q., Lao, D. B. and Hanaoka, J.: 2001, *Solar Phys.* 201, 153.
- Chernov, G. P., 2011, Fine structure of solar radio bursts, Springer ASSL 375, Heidelberg.
- Chernov G. P., Sych, R. A., Meshalkina, N. S., Yan, Y. and Tan C. 2012a: *Astron. Astrophys.* 538, A53.
- Chernov G. P., 2012b, Complex Radio Zebra Patterns escaping from the Solar Corona and New Generation Mechanisms, In: *Horizons in World Physics*, V. 278, Eds: Albert Reiner, Nova Science Publisher, New-York, Ch. 1, P. 1-75. https://www.novapublishers.com/catalog/product_info.php?products_id=30998.
- Chernov, G. P., Yan, Y. H., and Fu, Q. J.: 2003, *Astron. Astrophys.* 406, 1071.
- Chernov, G. P., Yan, Y. H., Fu, Q. J. and Tan Ch. M.: 2005, *Astron. Astrophys.* 437, 1047.
- Chernov, G. P., Yan, Y. H, Fu. Q. J.: 2014a, *Research in Astron. Astrophys.* 14, 7, 831.
- Chernov, G. P., Fomichev, V. V., Gorgutsa, R. V. Markeev A. K., Sobolev, D. E. Hillaris, A. Alissandrakis, K.: 2014b, *Geomagnetism and Aeronomy*, 54, 406.
- Chernov, G. P., Fomichev, V. V., Tan, B. L., Yan, Y. H., Tan, Ch. M. and Fu, Q. J.: 2015, *Solar Phys.* 290, 95.
- Chernov, G. P., Fomichev, V. V., Tan B. L., Yan, Y. H, Tan Ch. M., Fu. Q. J.: 2016, *Res. Astron. Astrophys.* 16, 28.
- Fomichev, V. V. and Fainshtein, S. M.: 1988, *Sov. Astron.* 32, 552.
- Gao, G. Dong, M., L. Wu, N. Lin, J.: 2014, *New Astronomy*, 30, 68.
- Gladd, N. T.: 1983, *Phys. Fluids*, 26, 974.

- Hankins, T. H., & Eilek, J. A. 2007, *ApJ*, 670, 693.
- Huang G., and Lin J.: 2006, *ApJ*, 639, L99.
- Huang, G. L., and Tan, B. L.:2012, *Astrophys. J.* 745, 186.
- Kaneda, K., Misawa, H. Iwai, K. Tsuchiya, F. and Obara, T.: 2015, *Astrophys. J. L.* 808, L45.
- Karlický, M., Barta, M., Jiricka, K. et al.,: 2001, *Astron. Astrophys.* 375, 638.
- Karlický, M., Meszarosova, H., & Jelinek, P.: 2013, *Astron. Astrophys.* 550, A1.
- Karlický, M.: 2013, *Astron. Astrophys.* 552, A90.
- Karlický, M. and Yasnov, L. V.: 2015, *Astron. Astrophys.* 581_A115.
- Kuijpers, J.: 1975, *Collective wave-particle interactions in solar type IV radio source*, *Ph.D Thesis*, Utrecht University.
- Kuijpers, J.: 1980, in M. R. Kundu and T. E. Gergely (eds), *Theory of type IV dm Bursts*, Radio Physics of the Sun, p. 341.
- Kuznetsov, A. A.: 2005, *Astron. Astrophys.* 438, 341.
- Kuznetsov, A. A.: 2006, *Solar Phys.* 237, 153.
- Kuznetsov, A. A. 2007, *Astron. Letters.*, 33, 319.
- Kuznetsov, A. A., and Tsap, Yu. T.: 2007, *Solar Phys.* 241, 127.
- LaBelle J., Treumann R. A., Yoon P. H., Karlický M.: 2003, *Astrophys. J.* 593, 1195.
- Lapuhov, A. I. and Chernov, G. P.: 2006, *Plasma Phys. Rep.* 32, 866.
- Lapuhov, A. I. and Chernov, G. P.: 2009, *Plasma Phys. Rep.* 35, 160.
- Lapuhov, A. I. and Chernov, G. P.: 2012, *Plasma Phys. Rep.* 38, 613.
- Ledenev, V. G., Yan, Y., and Fu, Q.: 2006, *Sol. Phys.*, 233, 129.
- Melnik, V. N., Rucker, H. O, and Konvalenko, A. A.: 2008, *Solar Physics Research Trends* (ed. P. Wang) Nova Science Publisher, NY, Ch. 8, 287.
- Mollwo, L.: 1983, *Solar Phys.* 83, 305.
- Mollwo, L.: 1988, *Solar Phys.* 116, 323.
- Selhorst, C. L., Silva-Válio, A., and Costa, J. E. R. 2008, *A&A*, 488, 1079.
- Slotje, C.: 1981, *Atlas of fine Structures of Dynamic Spectra of Solar Type IV-dm and Some Type II Bursts*, Utrecht Observatory.
- Stepanov, A. V., Tsap, Yu. T.: 1999, *Astron. Rep.* 43, 838.
- Tan B. L., Yan Y. H., Tan C. M., Sych R. A., Gao G. N., 2012, *Microwave zebra pattern Structures in the X2.2 solar flare on Feb. 15, 2011*, *Astrophys. J.* 744, 166-183.
- Tan B. L., Tan C. M., 2012, *Astrophys. J.* 749, 28-35.
- Tan, B. L., Tan, C. M., Zhang, Y., Mészárosová, H., Karlický, M., 2014a, *Astrophys. J.*, 780, 129.

- Tan, B. L., Tan, C. M., Zhang, Y., Huang, J. Mészáros, H., Karlický, M., Yan, Y. 2014b, *Astrophys. J.*, 790, 151.
- Treumann, R. A., Nakamura, R., Baumjohann, W.: 2011, *Ann. Geophys.*, 29, 1673.
- Tsang, K. T.: 1984, *Phys. Fluids*, 27, 1659.
- Viktorov, M., Mansfeld, D., and Golubev, S.: 2015a, *EPL*, 109 (2015) 65002.
- Viktorov, M. E. Golubev, S. V. Zaitsev, V. V. and Mansfeld, D. A.: 2015b, *Radiophysics and Quantum Electronics*, 57, 849.
- Winglee, R. M. and Dulk G. A.: 1986, *Astrophys. J.* 307, 808.
- Yasnov, L. V., and Karlický, M.: 2015, *Solar. Phys.* 290, 2001.
- Yan, Y. H., Zhang, J., Wang, W., et al.: 2009, *Earth Moon and Planets*, 104, 97.
- Yan, Y., Wang, W., Liu, F., et al.: 2013, in *IAU Symposium*, 294, eds. A. G. Kosovichev, E. de Gouveia Dal Pino, and Y. Yan, 489.
- Yu, S. J., Yan, Y. H., and Tan, B. L.: 2012, *Astrophys. J.*, 761, 136.
- Yu, S. J., Nakariakov, V. M., Selzer, L. A., Tan, B. L., & Yan, Y. H.: 2013, *Astrophys. J.* 777, 159.
- Zheleznyakov V. V.: 1995, *Radiation in Astrophysical Plasma*, Kluwer Academic, Dordrecht (in Russ. Izdat. Nauka, Moscow, 1977).
- Zheleznykov, V. V., and Zlotnik, E. Ya.: 1975a, *Solar. Phys.* 44, 447.
- Zheleznykov, V. V., and Zlotnik, E. Ya.: 1975b, *Solar. Phys.* 44, 461.
- Zlotnik, E. Ya.: 1976, *Izv. VUZov Radiofizika*, 19, 481.
- Zlotnik E. Ya.: 2009, Origin of zebra pattern in type IV solar radio emission, *Cent. Eur. Astrophys. Bull.* 1, 281-298.
- Zlotnik, E. Ya.: 2010, *Solar-Terrestrial Physics, Collected articles*, Siberian Depatement of Russian Academy of Sciences Eds, (in Russian), 16, 49.
- Zlotnik E. Ya.: 2013, *Solar. Phys.* 284, 579.
- Zlotnik E. Ya, Zaitsev V. V., Altyntsev, A. T.: 2014, *Solar. Phys.* 289, 233.
- Zlotnik E. Ya, Zaitsev V. V., Aurass H., Hofmann A.: 2003, Solar type IV burst spectral fine structures- Part II- Source model, *Astron. Astrophys.* 410, 1011.
- Zlotnik E. Ya., Zaitsev V. V., Melnik V. N, Konovalenko A. A. and Dorovskiy V. V.: 2015, *Solar. Phys.* 290, 2013.

Complimentary Contributor Copy

INDEX

#

¹⁰Be spikes, 5
¹⁴C concentration, 5, 6
¹⁴C spike, 6

A

amplitude, viii, 45, 47, 48, 49, 51, 54, 55,
56, 57, 58, 59, 60, 61, 62, 63, 64, 66, 67,
68, 69, 72, 73, 74, 76, 82, 90, 139
anisotropy, 135
assessment, 11
atmosphere, vii, 46, 51, 52, 76, 83, 137, 138
atoms, 52, 76
aurora borealis, vii, 1, 6
authenticity, 132

B

bandwidth, 124
Beijing, 101
Belgium, 100
bilateral, 74
breakdown, 6
Brno, 77
broadband, 139, 145
Bulgaria, 78

C

cables, 48
calcium, 52
calibration, 109
campaigns, 7
carbon, 10
Caribbean, 2
Carrington, vii, 1, 2, 4, 5, 6, 7, 8, 9
Carrington event, vii, 1, 2, 4, 5, 6, 7, 8, 9
cell phones, 7
Central Europe, 49, 62
challenges, 82
chaos, 8, 76
China, 101
cities, 7, 8
civilization, vii, 4, 6, 7, 10
classes, 51, 58, 63, 84
classification, 55, 118
climate, 9, 46, 84
clusters, 114
collisions, 76, 77
color, 56, 57, 60, 62, 68
communication, 71, 126
communication systems, 71
communities, 7
comparative analysis, 146
composition, 47
computation, 70
computing, 74

condensation, 7
 configuration, 83
 contradiction, 120
 controversies, 118
 coronal mass ejection, vii, 2, 3, 4, 121, 142
 correlation, 57, 63, 69, 70, 83, 92, 117, 127
 correlation analysis, 117, 127
 cosmic rays, vii, 1, 52
 cost, 2
 current limit, 9
 cycles, ix, 10, 81, 83, 84, 90, 91, 92, 98, 102
 Czech Republic, 77, 118

D

damages, 51
 database, 74, 77, 89
 decay, 83, 90, 98, 115, 116, 124, 143
 deficit, 83
 depolarization, 128, 129
 detection, 58, 78
 developing countries, 7
 diffraction, 103
 diffusion, 107
 disaster, 2, 7
 dispersion, 134
 displacement, 105
 distribution, viii, ix, 45, 72, 81, 83, 89, 91,
 102, 105, 108, 115, 134, 135, 136
 distribution function, 102, 134, 135, 136
 divergence, 83
 diversity, 130
 DOI, 9, 76

E

earthquakes, 47, 71
 EIS, 89
 EIT, 132, 146
 electrical conductivity, 66
 electricity, 2, 7
 electromagnetic, viii, 52, 83, 129, 135, 136,
 145
 electromagnetic waves, viii, 52, 129, 145

electron cyclotron resonance, 134, 143
 electronic systems, 7, 8
 electron(s), vii, viii, 45, 46, 47, 51, 52, 53,
 54, 55, 58, 62, 63, 64, 66, 68, 69, 70, 71,
 72, 74, 102, 114, 115, 128, 129, 133,
 134, 135, 136, 137, 139, 141, 143
 emission, 4, 5, 102, 103, 104, 105, 107, 108,
 109, 110, 111, 112, 114, 120, 124, 127,
 128, 129, 130, 131, 133, 136, 137, 138,
 139, 141, 142, 144, 145, 149
 energy, vii, ix, 5, 8, 9, 47, 72, 81, 83, 84, 86,
 88, 89, 90, 91, 92, 98, 108, 115, 120,
 126, 134, 135, 136
 energy transfer, 136
 environment, 71
 equilibrium, 128
 equipment, 48
 Europe, 72
 evidence, 9, 10, 58, 83, 89, 130
 evolution, ix, 82, 89, 98
 excitation, 103, 104, 108, 111, 133, 134,
 144
 execution, 54
 extinction, 5, 9
 extreme solar particle events, 5

F

families, 125
 fear, 2
 FFT, 125
 fiber(s), x, 101, 103, 104, 107, 108, 110,
 112, 115, 116, 121, 122, 124, 125, 128,
 131, 132, 133, 134, 136, 142, 144, 145,
 146
 formation, 52, 83, 103, 104, 108, 111, 115,
 118, 120, 132, 145
 formula, 115
 France, 81

G

geomagnetic storms, vii, 2, 47
 geometry, 129

Geostationary Operational Environmental Satellites (GOES), viii, 51, 58, 70, 71, 72, 83, 84, 85, 89, 91, 93, 111, 120
 Germany, viii, 50, 62, 78
 giant flare, 4
 giant solar flare(s), vii, 1, 3, 5, 6, 7, 8, 9, 11
 Gothenburg Geomagnetic Flip, 5
 GPS, 7, 47, 48
 GQD, viii, 45, 49, 50, 62, 63, 64, 65, 66, 68, 69
 Greece, 121
 growth, 66, 134, 135
 growth rate, 134, 135

H

height, 47, 52, 53, 55, 58, 60, 62, 64, 66, 67, 68, 69, 105, 107, 108, 116, 120, 130, 132, 133, 137, 139, 142
 helium, 76
 history, 133
 human, 4, 6, 7
 human health, 7
 hybrid, 102, 144
 hypothesis, ix, 82

I

ideal, viii, 45
 image(s), x, 102, 108, 112, 117, 120, 122, 127, 128, 129, 132
 impulsive, 98, 124
 incidence, 143, 146
 incubation time, 64
 infrastructure, 8
 injections, 134
 institutions, 52
 interference, 57, 62, 103, 118
 ionization, 46, 47, 48, 52, 54, 55, 58, 68, 73, 75
 ions, 51, 136
 islands, 114, 115, 142, 145
 Italy, 50, 57, 66

J

Japan, 10
 Jupiter, 3

K

kinetics, 76

L

lifetime, 108, 145
 light, vii, 11, 46, 57, 84, 115
 living conditions, 8
 lobbying, 7

M

magnetic field, 5, 105, 107, 108, 111, 116, 120, 128, 129, 132, 133, 136, 137, 138, 139, 141, 142
 magnetosphere, vii, 1, 73
 magnitude, vii, viii, 1, 4, 83, 108, 121, 139, 142
 man-made disasters, 7
 mass, vii, 1, 2, 3, 4, 5, 9, 121, 142
 matter, 116, 136
 measurement(s), 47, 53, 83, 104
 median, 91
 medical, 7, 8
 medical care, 8
 medicine, 7
 mega-cities, 7, 8
 meteor, 77
 meter, 104, 111, 128, 132, 134, 139
 microwave radiation, 102, 145
 military, 7
 milky way, 4
 Ministry of Education, 70
 mixing, 75
 models, 102, 103, 104, 105, 111, 118, 127, 131, 133, 135, 136, 137, 139, 146
 modernization, 7

Moon, 149
 morphology, 128
 Moscow, 81, 101, 147, 149

N

National Bureau of Standards, 71, 73
 National Oceanic and Atmospheric
 Administration, 51
 native communities, 7
 natural disaster, 8
 Netherlands, 77
 neutral, 51, 53
 New Zealand, 48
 nitrate spikes, 5
 nitric oxide, 47, 52
 nitrogen, 5, 52
 NOAA, 71, 72
 nonequilibrium, 143
 nonlinear dynamics, 82
 Norway, 10
 numerical analysis, 140

O

opacity, 76, 79, 143, 145
 oscillation, 10, 63, 69, 114, 117, 134, 145
 oxygen, 52

P

PAL, 48
 paleo-solar-flares, vii, 1
 parallel, 124, 128, 132, 139
 periodicity, 90, 134
 permission, 104, 106
 physical properties, 70
 physics, 11, 71, 82, 83, 126
 planetary conjunctions, 3
 polar, 98
 polarity, 112, 122, 129
 polarization, 111, 112, 113, 118, 122, 123,
 124, 127, 128, 129, 130, 144
 policy, 146

population growth, 7
 power plants, 7
 precipitation, 47, 71, 72
 probe, viii, 45
 propagation, viii, 45, 47, 48, 50, 51, 52, 53,
 54, 55, 57, 58, 62, 64, 68, 70, 71, 103,
 105, 110, 115, 128, 129, 134, 144, 145
 proportionality, 84
 protons, 136
 pulsars, 145

Q

quartile, ix, 82

R

radiation, viii, ix, 9, 46, 47, 51, 52, 54, 58,
 60, 62, 63, 64, 66, 67, 68, 69, 70, 72, 76,
 77, 78, 83, 101, 105, 128, 130, 135, 139,
 143, 144, 149
 radio, vii, viii, ix, 45, 47, 48, 49, 51, 52, 53,
 54, 55, 56, 57, 58, 59, 60, 61, 62, 63, 64,
 65, 66, 67, 68, 69, 70, 71, 73, 76, 79,
 101, 102, 103, 104, 105, 107, 108, 110,
 111, 120, 122, 124, 125, 127, 128, 129,
 130, 131, 132, 134, 136, 137, 138, 139,
 142, 143, 144, 145, 146, 147, 148, 149
 radius, 142
 RCP, 127
 reactions, 51
 recall, 133
 recognition, 11, 132
 recombination, 47, 52, 54, 72
 recombination processes, 47, 52
 relaxation, 72, 120, 135
 remote sensing, 71
 representativeness, 98
 requirement(s), 46, 128
 resolution, 49, 104, 108, 120, 125
 response, vii, viii, 75
 rings, 5, 9, 10
 Russia, 9, 77, 101

S

science, 74, 77
 sensing, viii, 45
 sensitivity, viii, 45, 142
 Serbia, viii, 13, 45, 50, 70, 74, 75, 78, 79
 shock, 111, 121, 125, 145
 SIDs, 52, 70
 signals, viii, 45, 47, 48, 49, 51, 54, 55, 58,
 62, 63, 66, 69, 70, 71, 73, 75, 76, 78, 79
 signs, 140
 simulations, 74, 133
 sodium, 52
 software, 48, 54
 solar activity, ix, 47, 82, 83, 90, 91, 92, 98,
 99
 solar flare(s), iv, vii, ix, 1, 2, 3, 4, 5, 6, 7, 8,
 9, 10, 27, 31, 41, 42, 43, 46, 47, 48, 51,
 52, 53, 54, 55, 58, 60, 62, 63, 64, 65, 66,
 67, 68, 69, 70, 71, 72, 73, 74, 76, 79, 81,
 82, 83, 84, 86, 89, 93, 98, 114, 117, 118,
 120, 130, 148
 space environment, 72
 spatial information, x, 101, 105
 spatial location, 108
 specialists, 82
 spectroscopy, 131
 speed of light, 138
 stars, vii, 1, 5
 state(s), viii, ix, 45, 76, 77, 81, 82, 84, 89,
 128, 135
 storage, 48
 storms, vii, 2, 47, 51
 structure, vii, ix, 84, 101, 102, 104, 106,
 108, 110, 111, 113, 114, 116, 117, 120,
 125, 128, 132, 133, 134, 136, 139, 140,
 141, 143, 144, 145, 146, 147
 Sun, vii, 1, 2, 3, 4, 5, 9, 10, 11, 46, 76, 83,
 102, 148
 sunspots, ix, 82, 83, 93, 98
 superflare(s), vii, 1, 2, 4, 5, 9, 11
 supernovae, 5, 9, 10
 supervisor, 74
 survival, 8
 Sweden, 1, 3

T

tangent angle, 105
 teams, 146
 techniques, 47
 technology, viii, 4
 telecommunications, 71
 temperature, 111, 135
 threats, 3, 4, 7, 8
 time resolution, 48, 105, 142
 total energy, 98
 trajectory, 91, 105
 transformation, 66, 103
 transmission, 73
 transparency, 143, 145
 transportation, 126
 trial, 54, 131
 turbulence, 114, 116

U

Ukraine, 139
 USA, 48, 49, 50, 51, 56

V

variables, 54
 variations, vii, viii, 47, 55, 56, 58, 60, 61,
 68, 73, 75, 83, 103, 118, 136, 142
 varieties, 103, 104
 vector, 106
 velocity, 82, 102, 105, 106, 107, 108, 116,
 131, 139, 142
 Venus, 3
 violence, 8

W

warning systems, 7, 8
 Washington, 71
 water, 7
 wave propagation, 55, 103, 104, 143
 wavelengths, 46, 47, 52, 83, 134, 139

web, 51
White House, 10
worldwide, 48

Y

yield, 104